






Universitat Autònoma de Barcelona

**ADVERTIMENT.** L'accés als continguts d'aquesta tesi queda condicionat a l'acceptació de les condicions d'ús establertes per la següent llicència Creative Commons:  [http://cat.creativecommons.org/?page\\_id=184](http://cat.creativecommons.org/?page_id=184)

**ADVERTENCIA.** El acceso a los contenidos de esta tesis queda condicionado a la aceptación de las condiciones de uso establecidas por la siguiente licencia Creative Commons:  <http://es.creativecommons.org/blog/licencias/>

**WARNING.** The access to the contents of this doctoral thesis it is limited to the acceptance of the use conditions set by the following Creative Commons license:  <https://creativecommons.org/licenses/?lang=en>



**Universitat Autònoma  
de Barcelona**

**From macro- to nanoscale electrodeposited  
iron-copper (Fe–Cu) for energy-efficient and  
sustainable applications**

**Evangelia Dislaki**

**Tesi Doctoral**

**Programa de Doctorat en Ciència de Materials**

**Dra. Eva Pellicer Vilà (directora i tutora)**

**Dr. Jordi Sort Viñas (director)**

**Departament de Física**

**Facultat de Ciències**

**2018**





Memòria presentada per aspirar al Grau de Doctor per

**Evangelia Dislaki**

Vist i plau

Dra. Eva Pellicer Vilà

(directora i tutora)

Dr. Jordi Sort Viñas

(director)

Bellaterra, 31/08/2018





La **Dra. Eva Pellicer Vilà**, investigadora Ramón y Cajal del Departament de Física de la Universitat Autònoma de Barcelona,

i el **Dr. Jordi Sort Viñas**, professor ICREA del Departament de Física de la Universitat Autònoma de Barcelona,

CERTIFIQUEN:

Que **Evangelia Dislaki** ha realitzat sota la seva direcció el treball d'investigació que s'exposa a la memòria titulada "*From macro- to nanoscale electrodeposited iron-copper (Fe-Cu) for energy-efficient and sustainable applications*" per optar al grau de **Doctor per la Universitat Autònoma de Barcelona**.

Que el disseny dels experiments, síntesi de mostres, llur caracterització, l'anàlisi dels resultats, i la redacció dels articles i d'aquesta memòria són fruit del treball d'investigació realitzat per Evangelia Dislaki.

I perquè així consti, signen el present certificat,

Dra. Eva Pellicer Vilà

Dr. Jordi Sort Viñas

Bellaterra, 31 d'agost de 2018



## Acknowledgements

I would like to begin by expressing my deepest thanks to my supervisors, Eva Pellicer and Jordi Sort, for their continued guidance throughout the course of this PhD and for the wealth of knowledge they instilled upon me. I also thank Prof. Santiago Suriñach for the warm welcome I received since I joined the group and Prof. Maria Dolors Baró for her useful advice and eagerness to help out wherever needed. To our technician, Pau, I extend my gratitude for maintaining the lab equipment, taking care of replenishing lab supplies and providing all the essentials in order to ensure an optimal work flow in addition to the always witty banter. In the same spirit, I thank the SELECTA European Training Network project coordinator, Jordi Malapeira, for always taking care of the administrative procedures and making life easier and less encumbered by bureaucratic issues. I would like to thank all of the current and former PhDs and postdocs I have spent my research life with these past few years, namely Doga, Cristina, Veronica, Irati, Jin, Sophia, Patrick, Fan, Alberto, Jordina, Miguel, Isarain, Shauna and Enric, for the expertise, the joyous moments as well as the occasional frustrations we shared. During my secondments, I was fortunate enough to collaborate and learn from the most accomplished professionals in their respective fields who welcomed me in their groups and supported my research efforts. Therefore, I would like to thank Prof. Paola Tiberto, Dr. Federica Celegato and Dr. Marco Coïsson at INRiM, Torino, as well as Prof. Paola Rizzi at the University of Torino for the excellent experience working jointly. I especially wish to thank my colleague Matteo at INRiM, for his invaluable contribution to our collaborative research project. I also thank Prof. Uta Klement and Dr. Yiming Yao at Chalmers University of Technology as well as Dr. Salvador Pané and Anastasia at ETH, Zurich. Furthermore, I extend my thanks to all the senior researchers from the participating and partner institutions of the SELECTA ETN for the excellent organization of the various joint workshops and for the knowledge and skills imparted, as well as the many invited speakers who contributed with their lectures and trainings on soft skills. To my fellow SELECTA Early Stage Researchers, I want to express my gratitude for the treasured memories and knowledge we accumulated together throughout the years, for their friendship and



kindness and encouraging words. They truly made this journey an enjoyable one and I hope we continue to keep in touch and collaborate along our future career paths. Of course, I would be amiss not to thank the European Commission for the funding of the SELECTA project under Horizon 2020 without which this PhD would not have been possible. Last but not least, I cannot find words adequate enough to thank my family who have always been there to offer their unconditional love and unwavering support, to believe in me with the greatest conviction and to lift me up even in the most difficult of times. They make everything I do worthwhile.

## Abstract

This work is focused on the electrodeposition and study of Fe–Cu in the form of continuous and patterned thin films and coatings as well as the fabrication and characterization of submicron motifs, nano- and microrods and tubes targeted at a variety of environmental and energy-efficient applications.

Firstly, different electrolytes are developed for the electrochemical deposition of  $\text{Fe}_x\text{Cu}_{1-x}$  coatings of several micrometers in thickness over a wide composition range ( $0 \leq x \leq 86$ ). The effect of various complexing agents and plating conditions such as pH, temperature and magnetic stirring on the morphology, structure, elemental composition and magnetic behavior is investigated. It is shown that the coatings are partially alloyed, despite the low mutual solubility of Fe and Cu, and saturation magnetization can be easily tuned by an adjustment of the Fe content.

Next, the synthetic protocols for the continuous coatings are extrapolated to the fabrication of patterned thin films with a hierarchical porosity achieved by coupling electrodeposition with colloidal lithography. The wetting properties of these films and their potential towards water-oil separation in mixtures and emulsions is assessed as a proof of concept. The high surface-to-volume ratio of the films in conjunction with the high roughness achieved by the macroporous network and the nanosized features along the pore walls lead to a strong hydrophobic/oleophilic nature of the deposits and an impressive absorption capacity. Notably, contrary to the thick coatings, the continuous and patterned  $\text{Fe}_{75}\text{Cu}_{25}$  and  $\text{Fe}_{85}\text{Cu}_{15}$  thin films are demonstrated to be fully alloyed.

Furthermore, the high surface-to-volume ratio and the inherent nanoporosity of the narrow pore walls of the patterned films unveil their excellent potential towards voltage control of magnetization. Indeed, a coercivity reduction of up to 25% under application of a negative bias is achieved. This constitutes a promising way to curtail power consumption since magnetization reversal can then occur with lower applied magnetic fields (i.e., lower electric currents and minimized Joule heating power dissipation).

Next, given the current trend towards miniaturization, submicron structures of three geometries and sizes are produced through electrodeposition onto pre-lithographed substrates. These substrates were previously prepared using electron-beam lithography which ensured a high feature quality. While existing literature on lithographed submicron motifs is largely based on structures below 50 nm in height, the structures prepared here are approximately 200-300 nm in height depending on plating conditions. This gives rise to interesting phenomena such as a compositional gradient, and thus different structural properties along the thickness. The magnetic properties are also thoroughly investigated with magnetic force microscopy suggesting magnetic curling effects.

Finally, compositionally graded magnetic nano- and microrods and tubes of various diameters are fabricated in polycarbonate track-etched membranes through conventional as well as micelle-assisted electrodeposition methods. The ferromagnetic character of the material enables wireless magnetic steering while photocatalytically-driven directional propulsion of the microtubes is also confirmed.

## Resum

Aquest treball se centra en l'electrodeposició i l'estudi del sistema Fe–Cu, tant sobre substrats llisos per a l'obtenció de pel·lícules contínues com en substrats proveïts amb un reticle o màscara, així com la fabricació i caracterització de motius de mida submicromètrica, nanobarres, microbarres i tubs, destinats a ésser utilitzats en una gran varietat d'aplicacions mediambientals i d'eficiència energètica.

En primer lloc, s'han dissenyat diferents electròlits per al dipòsit electroquímic de recobriments  $\text{Fe}_x\text{Cu}_{1-x}$  de diversos micròmetres de gruix en un ampli rang de composició ( $0 \leq x \leq 86$ ). S'ha investigat l'efecte de diversos agents complexants i condicions d'electrodeposició com el pH, la temperatura i l'agitació magnètica del bany sobre la morfologia, estructura, composició elemental i comportament magnètic dels dipòsits obtinguts. S'ha vist que el Fe i el Cu es troben parcialment aliats, malgrat la baixa solubilitat mútua entre ells, i que la magnetització de saturació es pot modular fàcilment a través del contingut de Fe.

A continuació, s'han extrapolat els protocols sintètics establerts per al creixement dels recobriments continus a la fabricació de pel·lícules primes amb una porositat jeràrquica aconseguida mitjançant electrodeposició sobre substrats decorats amb cristalls col·loïdals (*colloidal crystal templating*). S'ha avaluat la humectabilitat d'aquestes pel·lícules i la seva habilitat per extreure l'oli en mescles i emulsions aigua-oli. S'ha vist que l'elevada relació superfície-volum de les pel·lícules, juntament amb l'elevada rugositat derivada de la seva estructura macroporosa i el relleu nanomètric al llarg de les parets de porus, genera un marcat caràcter hidrofòbic / oleofílic dels dipòsits i una notòria capacitat d'absorció d'oli. A diferències de les capes contínues, que són més gruixudes, el grau d'aliatge entre el Fe i el Cu és total en les pel·lícules primes macroporoses de  $\text{Fe}_{75}\text{Cu}_{25}$  i  $\text{Fe}_{85}\text{Cu}_{15}$ .

A més, s'ha demostrat que l'elevada relació superfície-volum i la nanoporositat inherent de les estretes parets de porus de les pel·lícules macroporoses les han convertit en excel·lents candidates per al control de la magnetització mitjançant voltatge. De fet, s'aconsegueix una reducció de la coercitivitat fins a un 25% en ser polaritzades negativament. Aquesta és una metodologia prometedora per reduir el

consum d'energia, ja que la inversió de magnetització s'aconsegueix aplicant camps magnètics més baixos (és a dir, els corrents elèctrics involucrats són més baixos i, per tant, la dissipació de potència per efecte Joule es minimitza).

A continuació, tenint en compte la tendència actual cap a la miniaturització, s'han crescut estructures submicromètriques de tres geometries i mides diferents mitjançant electrodeposició sobre substrats prelitografiats. Aquests substrats es van preparar per litografia per feixos d'electrons per tal d'assegurar una elevada resolució dels motius. Tot i que la literatura existent sobre motius submicromètrics litografiats es basa principalment en estructures amb una alçada inferior a 50 nm, les estructures que s'han preparat en aquesta Tesi fan aproximadament 200-300 nm d'alçada en funció de les condicions d'electrodeposició. Això dóna lloc a fenòmens interessants com ara un gradient de composició i, per tant, diferents propietats estructurals al llarg del gruix. S'han investigat les propietats magnètiques mitjançant microscòpia de forces magnètiques, indicant l'existència d'efectes tipus *magnetic curling*.

Finalment, s'han fabricat nano i microbarres i tubs de diferent diàmetre magnètics i amb gradient de composició en membranes de policarbonat a través de mètodes d'electrodeposició convencionals i també a partir de banys amb surfactants amfifílics (*micelle-assisted electrodeposition*). El caràcter ferromagnètic de les estructures obtingudes ha permès la seva manipulació magnètica remota, mentre que s'ha confirmat la propulsió direccional fotocatalítica dels microtubs.

# Table of contents

<b>1. INTRODUCTION</b> .....	1
1.1. SUSTAINABILITY ASPECTS.....	1
1.2. ELECTRODEPOSITION OF METALS.....	3
1.3. THE Fe–Cu SYSTEM.....	7
1.4. SOFT AND HARD TEMPLATE PATTERNING TECHNIQUES.....	10
1.5. WETTING ON ROUGH SURFACES.....	12
1.6. EXPLOITING FERROMAGNETISM.....	14
1.7. VOLTAGE CONTROL OF MAGNETISM.....	20
1.8. OBJECTIVES.....	22
REFERENCES.....	23
<b>2. IMPORTANT HIGHLIGHTS RELATED TO THE EXPERIMENTAL TECHNIQUES</b>	35
2.1. CONFOCAL LASER SCANNING MICROSCOPY (CLSM).....	35
2.2. SPECTROSCOPIC ELLIPSOMETRY.....	37
2.3. MAGNETO-OPTICAL KERR EFFECT (MOKE).....	38
2.4. ELECTRON ENERGY LOSS SPECTROSCOPY (EELS).....	40
<b>3. RESULTS AS A COMPILATION OF ARTICLES</b> .....	43
3.1. PARAMETRIC AQUEOUS ELECTRODEPOSITION STUDY AND CHARACTERIZATION OF Fe–Cu FILMS.....	44

3.2. FABRICATION OF SUSTAINABLE HYDROPHOBIC AND OLEOPHILIC PSEUDO ORDERED MACROPOROUS Fe–Cu FILMS WITH TUNABLE COMPOSITION AND PORE SIZE VIA ELECTRODEPOSITION THROUGH COLLOIDAL TEMPLATES.....	57
3.3. COERCIVITY MODULATION IN Fe–Cu PSEUDO-ORDERED POROUS THIN FILMS CONTROLLED BY AN APPLIED VOLTAGE: A SUSTAINABLE, ENERGY-EFFICIENT APPROACH TO MAGNETO-ELECTRICALLY DRIVEN MATERIALS.....	73
<b>4. ELECTRODEPOSITED COMPOSITIONALLY GRADED MICRON- AND SUBMICRON-SCALE MAGNETIC STRUCTURES, TUBES AND RODS PATTERNED VIA HARD TEMPLATING AND LITHOGRAPHIC TECHNIQUES</b>	85
4.1. INTRODUCTION.....	86
4.2. EXPERIMENTAL.....	88
4.2.1. <i>Fabrication details</i> .....	88
4.2.2. <i>Sample preparation and post-process treatments</i> .....	89
4.2.3. <i>Electrolytes and plating conditions</i> .....	90
4.2.4. <i>Characterization</i> .....	91
4.3. RESULTS AND DISCUSSION.....	91
4.3.1. <i>Morphology of patterned structures</i> .....	91
4.3.2. <i>Chemical and structural analysis of structures</i> .....	94
4.3.3. <i>Magnetic characterization of the Fe–Cu motifs</i> .....	95
4.3.4. <i>Chemical and morphological analysis of electroplated nano/microrods and tubes</i> .....	98
4.3.5. <i>Photocatalytic performance of microtubes</i> .....	101
4.4. CONCLUSIONS.....	101

REFERENCES.....	103
<b>5. DISCUSSION.....</b>	<b>107</b>
<b>6. CONCLUSIONS.....</b>	<b>113</b>
<b>7. FUTURE PERSPECTIVES.....</b>	<b>117</b>





## Introduction

### 1.1. Sustainability aspects

The scarcity of raw materials and the environmental damage brought on by rapid technological progress underscores the importance of bringing forth sustainable alternatives. The European Union's (EU) industry and economy relies heavily on international markets for procuring important high-tech raw materials such as cobalt, platinum, rare earths and titanium since most of the natural reserves are found in non-EU countries. One notable exception is hafnium with France possessing 43% of the global supply.<sup>1</sup> China is the major supplier of important raw materials, such as rare earth elements (95% of the global supply), antimony, tungsten and magnesium and accounts for a 62% of their total supply to the EU. Brazil holds 90% of niobium which is used in aviation, in stainless steel alloys and in superconducting magnets for magnetic resonance imaging scanners.<sup>1</sup> The USA controls beryllium and helium supplies, Russia has 46% of the global palladium and South Africa holds the world's major iridium, platinum, rhodium and ruthenium reserves.<sup>1</sup>

In emerging economies (e.g. China, Russia, South Africa), protectionist government measures that include export taxes and quotas, price-fixing, dual pricing systems, and restrictive investment rules distort international trade in raw materials and create increasing challenges.<sup>2</sup> The problem is intensified by the high concentration of reserves on a country level and at a company level with further vertical integration resulting in few companies controlling a major percentage of the global trade.

Decreased competition leads, in turn, to rising prices for downstream companies which try to mitigate the effect with long-term contracts and by vertical integration with mining companies.<sup>2</sup> China has also increased its engagement in resource-rich developing countries, particularly in Africa, with infrastructure projects and active participation in exploration and extraction efforts. On the other hand, the USA and Japan, having recognized the importance of these critical raw materials, have implemented policies to safeguard their resources (e.g. stockpiling).<sup>2</sup>

In consideration of this global climate, the European Commission (EC) first launched the “Raw Materials Initiative” in 2008 to tackle the growing challenges with an integrated strategy and created a list of critical raw materials (CRMs) which are of high importance to the economy of the European Union and whose supply is associated with a high risk. This list was first published in 2011 with 14 CRMs identified and was updated in 2014 to include 20 CRMs. The latest list with 27 CRMs was released in 2017 and the EC is committed to regular updates at least every 3 years in order to reflect production, market and technological developments.

In addition, in its efforts to protect human health and the environment from chemical hazard and, at the same time, boost the competitiveness of the EU chemicals industry, REACH (Registration, Evaluation, Authorization and Restriction of Chemicals) was entered into force in 2007.<sup>3</sup> REACH is a regulation with which companies are obliged to comply by identifying the risk associated with the substances they manufacture and sell and by demonstrating their safe usage and providing information on risk minimization methods. It also seeks to encourage alternative methods for hazard assessment in an effort to reduce animal testing. Pursuant to the evaluation of all chemical substances, a list of substances of very high concern (SVHC) is composed with respect to their carcinogenic, mutagenic or toxic hazard.<sup>4</sup> The aim of this list is to slowly phase out the use of these substances or to implement new technologies where safer and economically feasible alternatives exists.

In response to these guidelines, it is imperative to develop new sustainable materials to meet technological demands. Iron, copper and aluminum-based materials are thus well suited as candidate replacements in a variety of applications due to their abundance, low cost and general safety.

## 1.2. Electrodeposition of metals

Among the various fabrication methods available for producing metallic thin films and coatings such as atomic layer deposition, physical vapor deposition, mechanical alloying and vacuum hot pressing sintering, and molecular beam epitaxy, electrodeposition stands out for its simple setup, cost-effectiveness, fast growth rates, facile control of resulting thickness and versatility in terms of creating complex three-dimensional geometries. In combination with lithographic techniques, it can be used to develop components for micro- and nanoelectromechanical systems (MEMS/NEMS) and wirelessly controlled microrobots. In addition, the use of minimally invasive electrolytic baths can further address the concern for environmentally friendly fabrication processes.

During electroplating, a metallic coating is formed onto a conductive substrate through electrochemical reduction of metal ions contained in an electrolyte. Typically, the chemical species containing the metals to be deposited are dissolved in a solvent such as deionized or ultrapure water or an organic compound, though electrodeposition from liquefied low (ionic liquids and deep eutectic solvents)<sup>5</sup> or high temperature<sup>6</sup> molten salts is also quite common. In this work, we will be exclusively discussing electrodeposition from aqueous electrolytes.

A typical 3 electrode cell used for electrodeposition is illustrated in **Figure 1.1**. The substrate to be coated is connected to the negatively charged electrode, known as cathode or working electrode (WE), while the anode or counter electrode (CE) is the positive polarity contact. The anode can consist of an inert metal (e.g. graphite, platinum, vitreous carbon) or can be soluble in order to secure a constant replenishment of the metal cations. The potential is accurately measured and controlled through the use of a third electrode with a stable and known potential which serves as a reference (RE) so that the potential difference between the WE and RE corresponds to the user defined value. Common types of reference electrodes include the saturated calomel electrode (SCE), the silver/silver chloride electrode (Ag/AgCl) and the mercury/mercurous sulfate electrode (Hg/Hg<sub>2</sub>SO<sub>4</sub>). To reduce the ohmic potential drop due to uncompensated solution resistance, a so-called Luggin capillary can be used to bring the potential measuring point in very close proximity to

the WE.<sup>7</sup> A potentiostat/galvanostat is an electronic device used to control the potential of the CE against the WE (potentiostatic mode) or the current flow between the CE and WE according to the user defined value. The temperature of the electrolyte can be precisely controlled with a hot plate connected to a temperature probe or by using a cell comprising an external thermostating jacket.

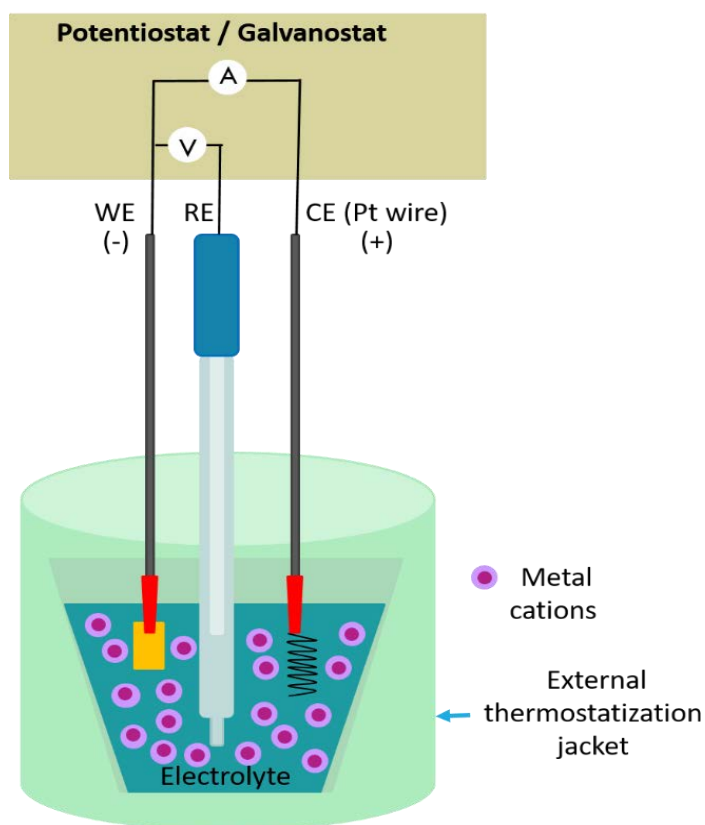


**Figure 1.1.** Illustration of a standard 3 electrode electrodeposition setup.

In order to determine the time necessary to reach a predetermined deposit thickness, Faraday's laws of electrolysis are widely used.<sup>7</sup> The first law states that the total mass of the substance deposited is proportional to the total electric charge passed through the electrolyte. The second law states that for the same electric charge, the mass of deposited substance is proportional to its atomic weight and inversely proportional to its valency. This can be summarized in **Equation 1.1**:

$$m = \left(\frac{Q}{F}\right) \left(\frac{A}{z}\right) \quad (1.1)$$

where  $m$  is the mass of the deposited metal,  $Q$  is the net electric charge passed through the system,  $F$  is Faraday constant ( $F = 96485 \text{ C mol}^{-1}$ ),  $A$  is the atomic weight of the metal and  $z$  is the valency of the dissolved metal ions in the solution. If we also consider that, in the case of constant current,  $Q = It$  the above equation is modified as follows:

$$m = \left(\frac{It}{F}\right) \left(\frac{A}{z}\right) \quad (1.2)$$

where  $I$  represents the applied electric current and  $t$  is the total time the current is applied. The calculated mass can be then used to determine the deposit thickness  $h$ :

$$h = \left(\frac{m}{Sd}\right) \quad (1.3)$$

where  $S$  stands for the surface area of deposition and  $d$  is the density of the material. From **Equation 1.3** we can see that the precise knowledge of the surface area is important for calculations. Therefore smooth, high quality surfaces are important to minimize the discrepancy between the geometric calculation of the surface area and the real value as determined by roughness. Due to the presence of these irregularities, electrodeposition starts at certain high energy sites or growth centers where the metal atoms are incorporated into the deposit. This, in turn, strongly influences the distribution of the current density, measured in  $\text{A m}^{-2}$ , across the surface.

Electrodeposition takes place at a very narrow interface, known as the electric double layer, (EDL) between the growing material and the solution. A charge separation occurs at this region due to the different nature of the mobile charges in the solution and in the solid. As a simplification, this can be thought of as a parallel arrangement of opposite charges. The structure of the EDL has a profound effect on the nucleation and growth processes.

In order to deposit a metal at a specific rate, it is necessary to shift the electrode potential from its equilibrium state in the cathodic (negative) direction, i.e. to apply an overpotential which is symbolized by the letter  $\eta$ . One notable exception is underpotential deposition which occurs at a potential less negative than the equilibrium value, e.g. due to strong interactions between the species that are being deposited and the substrate.<sup>8</sup> However, since different systems will spontaneously

approach the equilibrium state at different rates, the onset or nucleation overpotential can instead be defined, which represents the potential at which deposition begins.<sup>8</sup>

During the process of electrodeposition, there are four different partial reactions taking place in the electrolyte, namely mass transport due to diffusion, convection and migration which governs movement of the reactants from the bulk solution to the electrode surface, chemical reactions (e.g. dissociation of complexed metal ions), charge transfer between the WE and the electroactive species across the EDL and, finally, crystallization by which atoms are incorporated or removed from the crystal lattice.<sup>9</sup> As can be easily surmised, the slowest of these partial reactions determines the overall rate of the deposition process and is thus referred to as rate-determining or limiting. Therefore, the total overpotential is comprised of several components, which correspond to the overpotentials of each partial reaction. Upon charge transfer, the partially reduced ions or metal atoms adsorb onto the surface (i.e. adions or adatoms) where they subsequently diffuse to active growth sites and incorporate into the deposit. A non-ideal surface (a surface which is not ideally smooth but contains lattice defects) consists of flat crystalline layers called terraces and atomic steps which are known as ledges. The locations where ions or atoms can associate to the crystal are named kinks and are seen as steps along the ledges. This is described by the Terrace-Ledge-Kink (TLK) model of which a graphical representation is shown in **Figure 1.2**. Ledges and kinks along with dislocations, impurities and vacancies are considered as defects and play an important role in the structural properties of the resulting material.

Another important consideration is current efficiency since in most situations a certain amount of the charge is consumed by secondary reactions (e.g. cathodic hydrogen evolution, partial reduction of metal species) which occur in parallel with metal deposition.<sup>7</sup> Current efficiency is thus defined as the ratio of the total mass deposited to the theoretical value calculated from Faraday's laws. In the case of co-deposition, the partial current densities of the co-depositing metals which determine the final composition of the deposit should be evaluated.

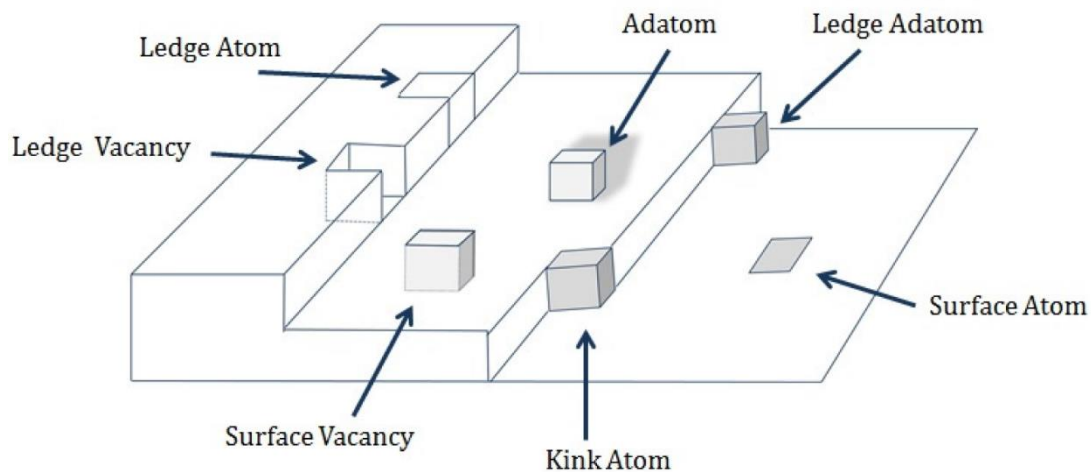


**Figure 1.2.** The Terrace-Ledge-Kink model of a real surface.<sup>8</sup>

The overpotential of deposition as well as the current efficiency are influenced by several parameters such as electrolyte composition (e.g. additives, complexing agents, type and concentration of metal salts), pH, temperature and stirring regime.<sup>7</sup> In most cases, additives are used to influence deposit morphology and structure with the purpose of improving quality and leading to enhanced performance.<sup>10-15</sup>

### 1.3. The Fe–Cu system

Iron and copper are plentiful elements in the earth's crust with iron constituting the fourth most abundant element after oxygen, silicon and aluminum.<sup>16</sup> Iron is essential for life<sup>17</sup> and has many desirable properties such as low cost, recyclability and versatility due to its magnetism-based polymorphism. At atmospheric pressure, iron has two crystal structures, namely body-centered cubic (bcc) and face-centered cubic (fcc). In the lowest-energy state the bcc alpha iron ( $\alpha$ -Fe) is stable while at a temperature of 1184 K it transforms into fcc gamma iron ( $\gamma$ -Fe). Above 1665 K and up to its melting temperature (1809 K) it transforms back to bcc phase of delta iron ( $\delta$ -Fe).<sup>18</sup> Alpha iron is ferromagnetic up to the Curie temperature of 1041 K where it becomes paramagnetic while gamma iron is paramagnetic in its stability range. Under high pressures (about 13 GPa at room temperature), iron undergoes a transition from bcc alpha phase to hexagonal close-packed (hcp) structure with loss of its ferromagnetic long-range order. This form is known as epsilon iron ( $\epsilon$ -Fe) and is found to be bountiful in the earth's core.<sup>19</sup> The diverse iron alloys and compounds feature



very different microstructure and a number of magnetic states which, in turn, greatly influence the physical properties, and can thus accommodate a variety of technological needs (e.g. iron-nickel magnetic devices, iron-zinc anti-corrosion protection, extensive use in steel manufacturing).<sup>18</sup> Further highlighting its versatility, iron can be electrodeposited as a hard and brittle material and subsequently rendered soft and malleable by heat treatment or, conversely, it can be soft and ductile as prepared and carburizing, nitriding or cyaniding processes can be employed to increase the surface hardness.<sup>20</sup> One of the main challenges related to iron electrodeposition, which is problematic for magnetic applications, is the potential oxidation of  $\text{Fe}^{2+}$  to  $\text{Fe}^{3+}$  upon reaction with dissolved oxygen in water-based electrolytes. Since the local pH at the working electrode increases due to hydrogen evolution,  $\text{Fe}^{3+}$  can cause Fe(III) hydroxide precipitation and incorporation into the deposit. Moreover, since hydrogen evolution takes place concurrently with iron deposition, inevitable hydrogen absorption will lead to deposit embrittlement, which can be partially mitigated by high temperature annealing.<sup>7</sup> For this reason, the use of non-water based electrolytes for iron plating like ethylene glycol or deep eutectic solvents is nowadays researched.<sup>21,22</sup> Meanwhile, copper is also of critical biological importance<sup>23,24</sup>, is environmentally friendly and constitutes the most commonly plated metal due to its very high throughput, excellent coverage and high conductivity<sup>18</sup> with applications in electrical wiring, the semiconductor industry<sup>25</sup> and antibiofouling<sup>26,27</sup> among other areas. In recent years, the synthesis of Cu nanoparticles for printed electronics to replace the expensive silver and gold nanoparticle inks in conductive printing has garnered much research attention.<sup>28,29</sup> It has been well established in previous literature that the mutual solid solubility of iron and copper is very low in equilibrium conditions despite their similar atomic radii due to the positive enthalpy of mixing,  $\Delta H_{mix}$  (calculated value of  $\Delta H_{mix} \approx +13 \text{ kJ mol}^{-1}$  and experimental value of  $\Delta H_{mix} \approx +8.9 \text{ kJ mol}^{-1}$  in the liquid phase for an equiatomic composition at 1873 K),<sup>30</sup> which encourages clustering of the atoms into Fe-rich and Cu-rich groups to reduce the internal energy.<sup>31</sup> However, the degree of clustering will decrease as temperature increases due to the increasing importance of entropy.<sup>31</sup> A calculated phase diagram for the Fe—Cu system is given in **Figure 1.3**. The solubility

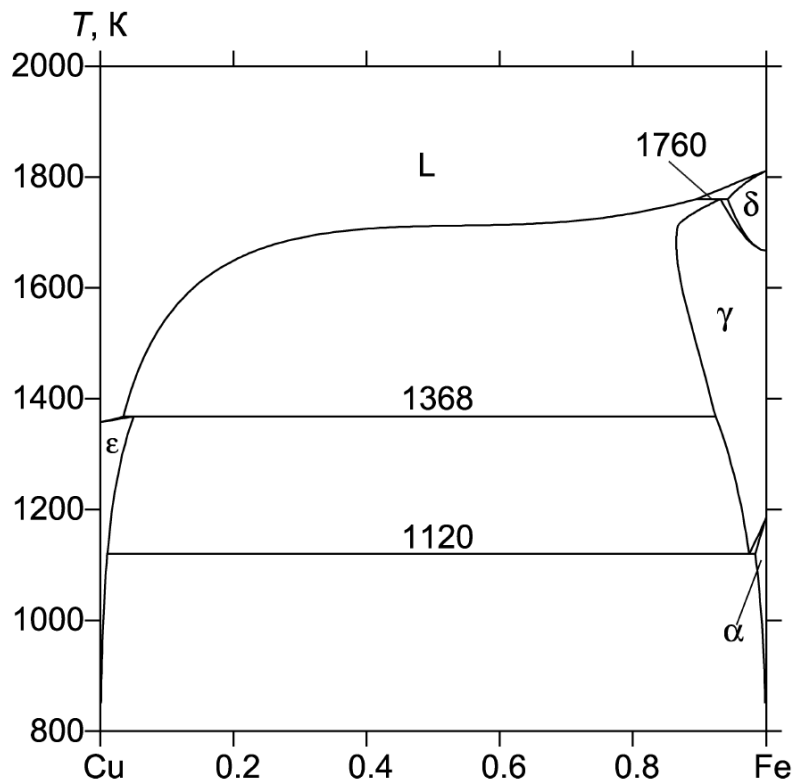


**Figure 1.3.** Calculated phase diagram for the Fe—Cu system.<sup>32</sup>

of iron in copper is generally reported to be slightly lower than that of copper in iron as determined by the integral heat of mixing.<sup>30</sup>

The novel properties of alloyed and bimetallic thin films and coatings composed of typically immiscible elements such as high thermal and electrical conductivity, large ductility, enhanced strength, as well as superior magnetic properties like high magnetoresistance and coercivity, have attracted considerable scientific and technologic interest.<sup>33</sup> Moreover, due to the fascinating magnetic properties of Fe—Cu alloys, many methods, such as mechanical alloying<sup>34</sup> and magnetron sputtering<sup>35</sup> have been employed to form metastable iron-copper solid solutions over the entire composition range. For example, Chien et al. report that, while the magnetic moment of Fe often rapidly declines with alloying due to the magnetic weakness of Fe, it remains nearly constant up to high concentrations of Cu in the Fe—Cu system.<sup>35</sup> Meanwhile, according to Kuch et al., in fcc Fe—Cu alloy thin films grown epitaxially by pulsed-laser deposition on Cu(001), the Fe orbital moments are found to be significantly enhanced with respect to pure Fe.<sup>36</sup> In reference to electroplated films, metastable iron—copper solid solutions have been reported in a few studies related

to thin films within certain composition ranges (a detailed treatment of the state of the art on electrodeposited Fe–Cu is given in Chapter 3.1).<sup>37-39</sup> Noce et al. found that the Fe<sub>10</sub>Cu<sub>90</sub> film prepared by pulsed electrodeposition is superparamagnetic with Fe-rich clusters forming within a Cu-rich matrix at room temperature, and that at a critical temperature of 120 K a superferromagnetic order develops.<sup>38</sup> Nevertheless, the limited existing research and the often contradictory results reported highlight the need for more systematic investigation.

#### 1.4. Soft and hard template patterning techniques

In order to produce porous materials several soft and hard templating techniques exist. Hydrogen bubble dynamic template<sup>14,40-42</sup>, ionic surfactants, which are based on electrostatic interactions, as well as a wide variety of non-ionic amphiphilic surfactants (e.g. Brij, block copolymers)<sup>43-46</sup> have been widely used as soft templates. Biological templates, anodized aluminum oxide (AAO) and polycarbonate track etched (PCTE) membranes, mesoporous zeolites, discrete particles (e.g. colloidal spheres) and in situ templates are commonly employed in the hard-templating approach.<sup>46-51</sup> Some examples of the different techniques are shown in **Figure 1.4**. A combination of soft

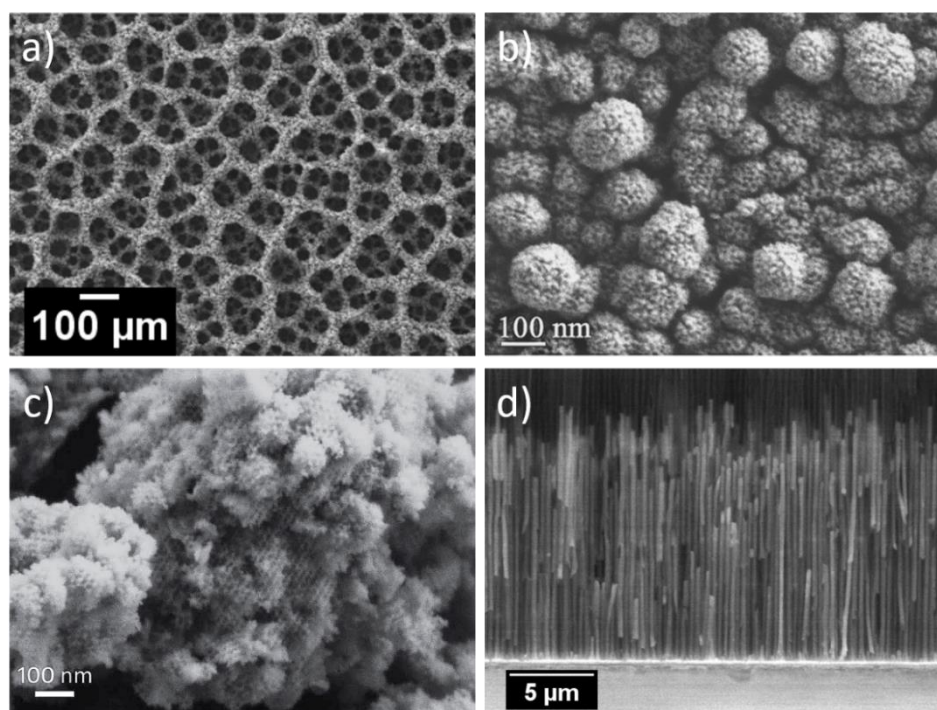


**Figure 1.4.** a) Porous Cu film prepared using hydrogen bubble dynamic template,<sup>40</sup> b) mesoporous Fe-Pt layer grown on Au through micelle-assisted electrodeposition,<sup>43</sup> c) mesoporous silica (KIT-6) templated Co-doped In<sub>2</sub>O<sub>3</sub> oxide<sup>50</sup> and d) Co-W mesowires grown in an AAO template.<sup>47</sup>

and hard templating techniques can lead to hierarchically structured materials with complex architectures.

With respect to introducing porosity in thin films and coatings, colloidal lithography is a particularly potent method when combined with electrodeposition since it allows the creation of three-dimensionally ordered macroporous materials through a straightforward and inexpensive procedure as compared to sophisticated, high cost lithographic techniques.<sup>52,53</sup> For the arrangement of the colloidal particles onto the substrate in a face-centered cubic or hexagonal close-packed structure, several options exist such as dip-coating, vertical deposition, electrophoretic deposition, crystallization driven by depletion force and spin coating.<sup>54,55</sup> An example of colloidal spheres electrophoretically deposited onto Au is seen in **Figure 1.5**.

Finally, since the advent of nanolithography, diverse techniques have been developed for patterning miniaturized structures. Amid these, electron beam lithography has unique benefits such as high resolution down to a few nanometers,<sup>56,57</sup> flexibility in pattern replication and accurate and precise alignment. Typically, a positive polymeric electron-beam resist such as poly(methyl methacrylate) (PMMA), is used to coat the substrate prior to the process. Then a focused beam of electrons exposes the resist writing the desired pattern. A solvent-based developer is then used to remove the

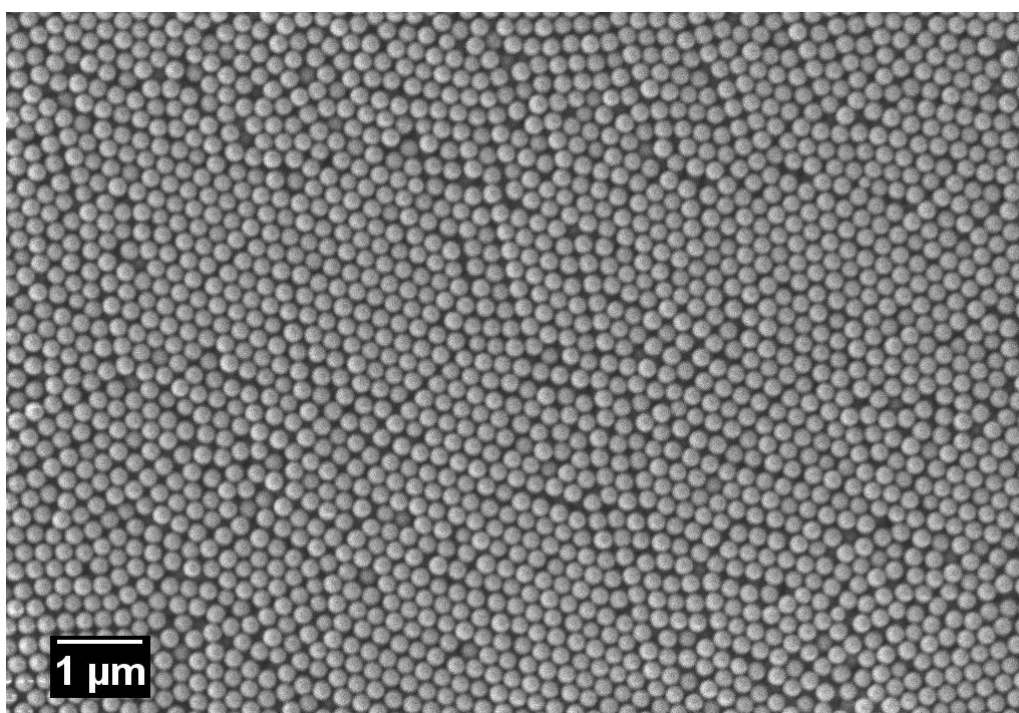


**Figure 1.5.** Colloidal spheres of 350 nm in diameter assembled onto an Au substrate.

resist in the exposed areas. If our substrate is conductive we can then immerse it in our chosen electrolyte and grow our metallic motifs.

### 1.5. Wetting on rough surfaces

One important aspect of metallic thin films, both during their growth as well as in terms of the functional properties of the resulting deposit, concerns their wetting behavior. Wettability is a fundamental property with extensive applicability such as in anti-corrosion, anti-reflection, transparency, drag reduction, self-cleaning, anti-biofouling and water/oil separation.<sup>58</sup> When placing a liquid on a surface, adhesive forces between the surface and the liquid will cause it to spread and form a continuous film while cohesive forces within the liquid will cause it to form a droplet to minimize contact with the surface. Therefore, wetting behavior can be viewed as a competition between adhesion and cohesion.

The angle formed between the surface and the liquid droplet, known as the static contact angle  $\theta$ , is a one-dimensional phenomenon determined by the mechanical equilibrium between three surface tensions  $\gamma$  acting on the contact line of the vapor (v), the liquid (l) and the solid (s) phases, which are symbolized as  $\gamma_{vl}$  (vapor/liquid)  $\gamma_{ls}$  (liquid/solid) and  $\gamma_{vs}$  (vapor/solid).<sup>59</sup> For an ideally smooth rigid surface, the relationship between these tensions is described by Young's equation<sup>60</sup> (**Equation 1.4**) and the contact angle at the three-phase interface is shown schematically in **Figure 1.6**.

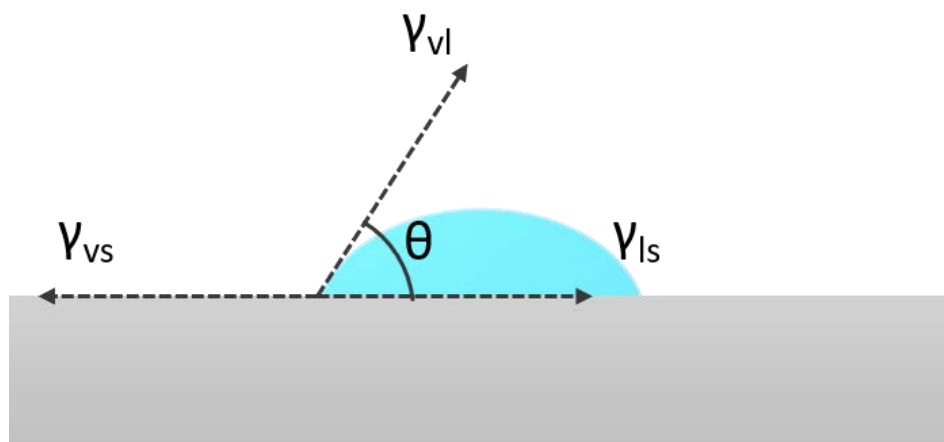


**Figure 1.6.** Equilibrium forces acting on a liquid droplet placed on a smooth solid surface.

$$\gamma_{vs} = \gamma_{vs} + \gamma_{vs} \cos \theta \quad (1.4)$$

When the contact angle is  $0^\circ$  there is perfect wetting while when  $\theta$  is between  $0^\circ$  and  $90^\circ$  a partial wetting scheme exists. An angle between  $90^\circ$  and  $180^\circ$  degrees implies a non-wetted state and at  $180^\circ$  perfect non-wetting is achieved.<sup>59</sup> When the liquid is water, the surface is called hydrophilic in the partial and superhydrophilic in the near-perfect wetting regime, respectively, whereas in the non-wetted state it is considered as hydrophobic. For  $\theta$  values above  $150^\circ$  superhydrophobicity is said to be achieved.

Besides Young's angle, there are two additional important angles that can be measured when a liquid droplet is slowly expanding on or retracting from a surface. The maximum and minimum stable angles are entitled advancing and receding angle, respectively, and their difference is the contact angle hysteresis. The hysteresis is equal to zero for an ideally smooth surface. In practice, however, most surfaces are far from the ideal case and a certain amount of roughness and inhomogeneity exists. Wetting on rough surfaces was first described by Wenzel<sup>61</sup> for the fully wetted regime while for partial wetting with air pocket formation at the interface between the liquid and the solid surface the Cassie-Baxter model<sup>62</sup> was developed. An example of these two wetting states is illustrated in **Figure 1.7**. It should be noted that the Wenzel and Cassie-Baxter models often fail to accurately predict the contact angle since they erroneously assume that it is a result of a simple thermodynamic equilibrium determined by the energetics at the contact area.<sup>63</sup> The fundamental distinction of the two wetting states, however, still stands.

As can be gleaned from the above, contact angle hysteresis is an important parameter in rough surfaces and is essential in distinguishing sticky from non-sticky surfaces. In nature, rose petals and lotus leaves are both intrinsically superhydrophobic but have

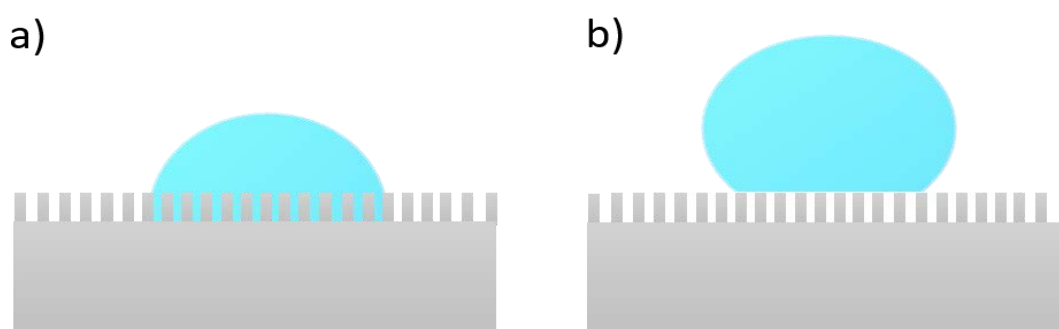


**Figure 1.7.** Rough surface wetting states: a) Wenzel and b) Cassie-Baxter.

very different adhesive forces with water. Rose petals benefit from a hierarchical roughness where water can impregnate large micron sized grooves while air pockets are formed in the nanosized grooves resulting in a strong adhesion with high contact angle hysteresis.<sup>64</sup> In contrast, lotus leaves have smaller micro- and nanostructures which do not allow water to enter thus leading to a low adhesion, i.e. hysteresis, which causes the droplets to easily roll off the leaves.<sup>65,66</sup> This distinction has attracted tremendous interest due to the multitude of prospective applications.<sup>67</sup>

Some examples of hydrophobic metallic surfaces prepared by electrodeposition include gold flower-like microstructures on indium tin oxide (ITO)-coated glass, silver polyhedrons and dendrites on copper covered by a thin nickel film, copper and copper oxide microstructures, ZnO nanorods onto fluorine-doped tin oxide (FTO)-coated glass, cobalt structures with dendritic and flower-like morphologies, manganese rough clusters, an urchin-like lanthanum complex ( $\text{La}[\text{CH}_3-(\text{CH}_2)_{12}-\text{COO}]_3-$ ) and tungsten oxide rough surfaces with pebble-like morphology.<sup>68</sup> Hydrophobic copper-nickel<sup>69</sup> and nickel coatings have been extensively researched and prepared by a variety of one-step, two-step and composite electrodeposition methods.<sup>58</sup>

## 1.6. Exploiting ferromagnetism

Among the multiple functional properties of electrodeposited metallic alloys, the investigation of their magnetic behavior and its evolution depending on size, shape and surface topography is of great interest. On an atomic scale, electrons are characterized by two types of magnetic moment. One is associated with the electron's orbital movement around the nucleus and the other with its spinning motion around its own axis of rotation. Electron spin can be oriented either in the up or in the down direction. Orbital and spin moments of electron pairs can cancel each other out and, therefore, the net magnetic moment of the atom is determined by all orbital and spin contributions taking into account these cancellations.

Ferromagnetic materials possess a permanent magnetic moment resulting mainly from the existence of uncanceled electron spins since the contribution from orbital moments is quite small. Furthermore, coupling interactions cause neighboring electron spins to align with each other over large areas which are called magnetic

domains. The size of the domains is microscopic, and, for a polycrystalline material, the grain and magnetic domain sizes do not necessarily coincide, namely each grain can contain more than one magnetic domain, or a single domain can contain several grains. The different domains are separated by walls along which the direction of magnetization gradually starts to change. Usually, the domains are randomly oriented with respect to one another and the bulk material remains unmagnetized. However, when an external magnetic field is applied, the domain walls propagate in such a way that the magnetic domains aligned favorably to the field direction grow at the expense of the others. In addition to domain wall propagation, rotation of the magnetic moments inside the domains toward the direction of the applied field also occurs. Both processes continue with increasing field strength until the material becomes macroscopically a single domain which is perfectly aligned in the field direction and then the maximum magnetization, i.e. saturation magnetization,  $M_s$ , is reached.<sup>70</sup> This phenomenon is illustrated in **Figure 1.8**.

Ferromagnets will tend to retain a portion of their magnetization, called the remanence, even after the external field is removed, thus resulting in a hysteresis effect. Therefore, when reversing the field direction from saturation, the original path delineated by the variation of the magnetization  $M$  with the applied field  $H$  will not be retraced. This effect is attributed to the resistance of domain wall motion in response to the field reversal. The field required to drive the magnetization of the material back to zero is its coercivity,  $H_c$ . Materials with high coercivity values that are difficult to magnetize and demagnetize are called hard magnetic while those with low coercivity, which as result involve less energy dissipation with respect to switching, are soft magnetic. This “memory” effect related to magnetic remanence forms the basis of magnetic data storage technologies. In Figure 1.8, these concepts are elucidated with the help of different hysteresis loops acquired for ferromagnetic Fe–Cu films of two distinct stoichiometries. Typical materials that display these characteristics are certain transition metals (Fe, Co, Ni) and their alloys as well as alloy compositions containing rare-earths like neodymium (Nd) and dysprosium (Dy). Recently, room temperature ferromagnetism was also discovered in tetragonal ruthenium (Ru).<sup>71</sup>



An immensely important parameter which strongly affects the shape of the hysteresis loop is magnetic anisotropy which describes the directional dependence of the magnetic properties. The different types of anisotropy can be categorized as magnetocrystalline, shape, stress and exchange anisotropy as well as induced by magnetic annealing, plastic deformation or irradiation.<sup>72</sup>

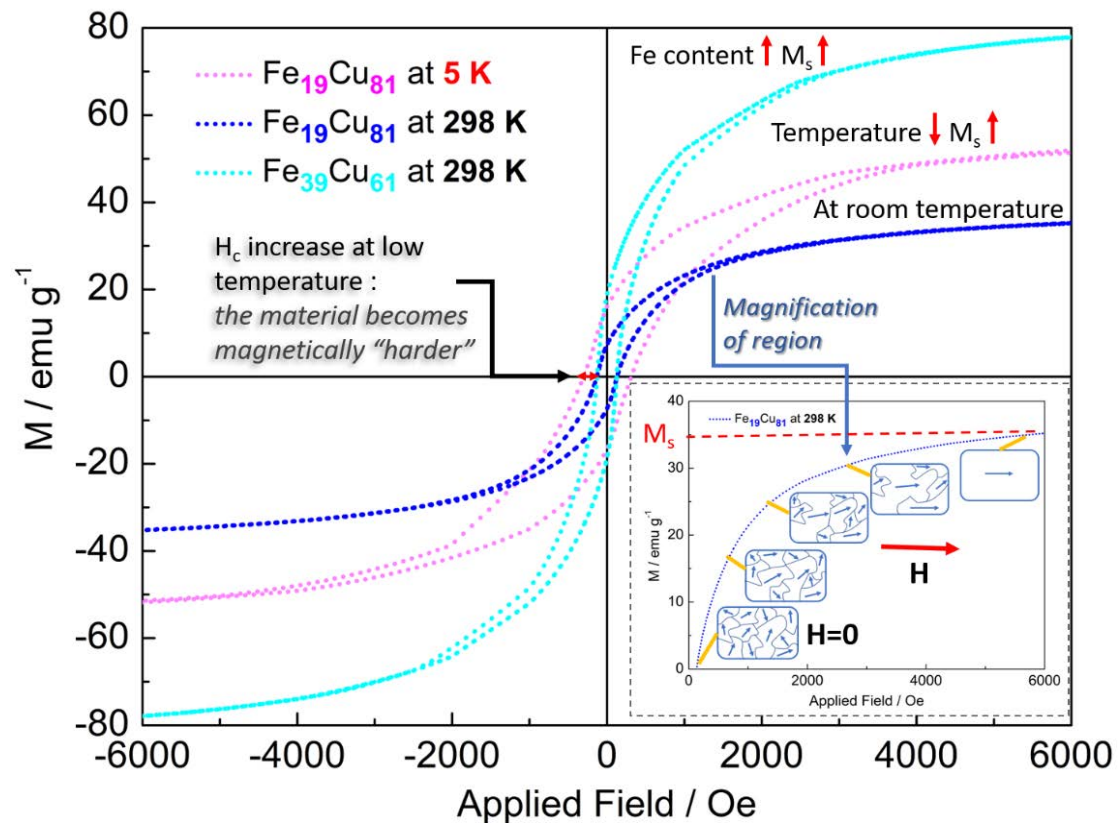


**Figure 1.8.** Comprehensive image illustrating basic ferromagnetism concepts through the Fe–Cu system.

Temperature constitutes an important factor influencing the magnetic behavior of the material. Saturation magnetization is maximum at 0 K where atomic thermal agitation is at a minimum. This is also described in Figure 1.8, where it is seen that the  $M_s$  of a  $\text{Fe}_{19}\text{Cu}_{81}$  film at 5 K is substantially higher than at room temperature. Random thermal motions counteract the coupling interactions such that with increasing temperature the saturation magnetization gradually decreases until it reaches the Curie temperature  $T_c$ , where it sharply declines to zero. At this temperature the material becomes paramagnetic which means that it no longer retains any magnetization when the external field is removed and, as consequence, there is no hysteresis effect. Certain alloys can be annealed in a magnetic field close to but below the Curie temperature and then cooled to room temperature to induce a permanent anisotropy

with an easy axis aligned with the applied field. This process is termed magnetic annealing and renders the material magnetically softer along the easy axis.<sup>72</sup> This effect has been technologically exploited as a means to record magnetic information in hard magnetic materials through thermally-assisted writing.<sup>73</sup>

Magnetocrystalline anisotropy is intrinsic to the material and is dependent on spin-orbit coupling. When an external field is attempting to reorient the electron spin, it also acts on the orbit which tends to resist due to strong orbit-lattice coupling. The anisotropy energy is the energy required to overcome the spin/orbit coupling and rotate the spin against the easy axis of magnetization. Crystal anisotropy is greatly influenced by temperature and rapidly decreases as the Curie temperature is gradually approached, at a faster rate than the magnetization, while dropping to zero at the Curie point. This causes the coercivity to also disappear since it is strongly dependent on the intrinsic anisotropy. For a polycrystalline material, if the individual grains are randomly oriented then the material will not exhibit a crystal anisotropy. In most cases, however, the crystals have a preferred orientation (or crystallographic texture) and then the material will have an anisotropy corresponding to the weighted average of the anisotropies of the individual grains.<sup>72</sup>

Shape can also be a source of anisotropy since materials are magnetized more easily along their long (easy) axis rather than their short (hard) axis. This means that larger fields are required to switch magnetization in the short axis direction.

When exposed to a magnetic field, a ferromagnetic material can also change its dimensions. This induced strain is termed magnetostriction  $\lambda$  and is measured at saturation. The effect is rather minuscule, but there exists an inverse magnetostrictive effect whereby the permeability of the material and the size and shape of the hysteresis loop can be changed dramatically when subjected to a mechanical stress. This means that if  $\lambda$  is positive an applied tensile stress which elongates the material (positive) will increase the magnetization while a compressive stress (negative) will decrease it. In polycrystalline metals, the magnetoelastic energy arising from stress application can be calculated as follows from **Equation 1.5**.<sup>74</sup>

$$E = -\frac{3}{2}\lambda\sigma\cos^2\theta \quad (1.5)$$

where  $\sigma$  is the applied stress and  $\theta$  is the angle between the saturation magnetization and the stress direction.

This property is utilized in magnetostrictive transducers and has been intensely investigated for future ultra-low power and high-density hybrid systems such as in spin transfer torque magnetic tunnel junction (STT-MTJ)-based nonvolatile memory.<sup>75-78</sup> However, there is still a performance gap with respect to high dynamic write energy, large latency, yield and reliability.<sup>79</sup>

Thanks to advances in lithographic and other unconventional synthesis techniques, recent work on nanomagnetism in three dimensions has been extensive. In 3D nanostructures, novel physical properties related to geometry, topology and chirality arise with great implications for sensing, data storage, nanoelectronics, cloud computing and biomedicine.<sup>80</sup>

One can also use the geometry of the material to tailor the optical and magnetic properties. Magnetic metamaterials, for instance, are synthetically created by subwavelength arrangement of the components rather than by compositional tuning, thus leading to passive electromagnetic properties not found in nature such as a negative refraction index and perfect absorption.<sup>81-83</sup> It is even possible to design materials with permittivity and permeability values that vary in an independent and arbitrary manner throughout and assuming positive or even negative values. Notably, negative permeability is a property naturally found only in diamagnetic materials.

Plastic deformation at room temperature can be used to alter the magnetic properties and induce a uniaxial anisotropy by a method called rolling. The easy axis can be either parallel or perpendicular to the rolling direction. It can be applied to metals and alloys to increase the density of dislocations and other defects. This, in turn, leads to clockwise rotation of the hysteresis loop, an increase in coercivity as well as increased mechanical strength and hardness.

Furthermore, a material can be bombarded with neutrons, ions, electrons or gamma rays to bring about atomic rearrangements which alter the physical and mechanical properties.<sup>72</sup> Ion irradiation or ion implantation can be utilized to augment mechanical strength and hardness and change the magnetization and crystal anisotropy.<sup>84-87</sup> This

can be achieved without necessarily increasing magnetic hardness as plastic deformation does and some materials become, in fact, magnetically softer.<sup>88</sup>

Light can also be used to switch the magnetization either by indirect coupling of the electric field component of the light with spins via spin-orbit interaction or direct coupling between the magnetic field component and spins.<sup>89</sup>

Another interesting way to realize magnetization switching has been by employing electric currents. When an electric current is polarized, i.e. it has an unequal number of spin-up and spin-down electrons, and passes through a magnetic material, the spin mismatch exerts a torque which can change the magnetization direction of the material when large enough currents are flowing.<sup>90</sup> This can be exploited for spin-transfer torque magnetic random-access memory (STT-MRAM) devices as the non-volatile effect is quite promising for information storage. However, the constant flow of a large current density is required, which causes high energy consumption.

Phase change materials (PCMs) are among the most promising for nonvolatile, rewritable data storage and their rapid speed, rivaling volatile dynamic random-access memories, makes them good candidates for a universal memory. A short voltage pulse is used to heat the PCM up to its melting temperature where it changes to a liquid phase. During this process the PCM is absorbing heat and provides a cooling effect. When the material is rapidly quenched, an amorphous state with higher resistivity is induced. After application of a second short pulse of lower voltage, the PCM recrystallizes, hence enabling the nonvolatile data storage functionality. Several approaches to decrease the required pulse power for storage have been explored.<sup>91</sup>

Taking into consideration the above, the switching of magnetization while preserving the magnetic behavior of the fabricated materials requires the application of magnetic fields which, in turn, are generated using electric currents. This, however, entails a large energy consumption through Joule heating. Therefore, the possibility to partially substitute electric currents with electric fields and thus achieve higher energy efficiency by minimizing Joule effect heat dissipation holds enormous potential. In this respect, voltage control of magnetism has been intensely pursued in recent years.<sup>92</sup>

## 1.7. Voltage control of magnetism

As has been evinced in the preceding short overview, the control of magnetism is a fascinating research topic due the vast array of applications in information technology. Among the different avenues explored in literature, voltage manipulation of magnetism is a particularly promising option with several added advantages such as reversibility, non-volatility and high-speed which can revolutionize magnetic data storage, high-frequency magnetic devices and spin-based electronics.

In metals, an enhancement of the electric field through the use of ferroelectric materials and electrolytes as dielectrics constituted a major breakthrough. Ionic liquids can tremendously magnify the electric field due to the presence of the electric double layer. Moreover, owing to the high oxygen mobility, they allow for an alternative mechanism of manipulation through chemically induced oxygen migration.<sup>93-96</sup> More in detail, when an electric field is applied, an electric double layer forms at the interface between the ionic liquid and the material with paired opposite charges. As result, transfer of oxygen ions can occur, mediated by oxygen vacancies, which alters the magnetic properties.

Nevertheless, the well-known screening effect, whereby an electric field can only penetrate a Thomas-Fermi screening length into a metal (in the order of atomic dimensions), was long considered a limitation in voltage control of magnetism.<sup>97</sup> In other words, the electric charges are concentrated at the surface and screen the bulk of the metal from the applied electric field. In the seminal work by Weisheit et al.,<sup>98</sup> a large electric field was achieved in FePd and FePt ultrathin films by immersing them in a propylene carbonate electrolyte with solvated  $\text{Na}^+$  and  $\text{OH}^-$  ions. Specifically, a coercivity modification of -4.5% and +1% in FePt and FePd was reached, respectively. A schematic of the electrolytic cell used is shown in **Figure 1.9**.

The change was attributed to a modulation in the number of unpaired  $d$  electrons with energies close to the Fermi under application of an electric field. Weisheit et al. also suggested that a high surface-to-volume ratio could be the key to overcoming the issue of screening and achieving substantial electric field induced changes.

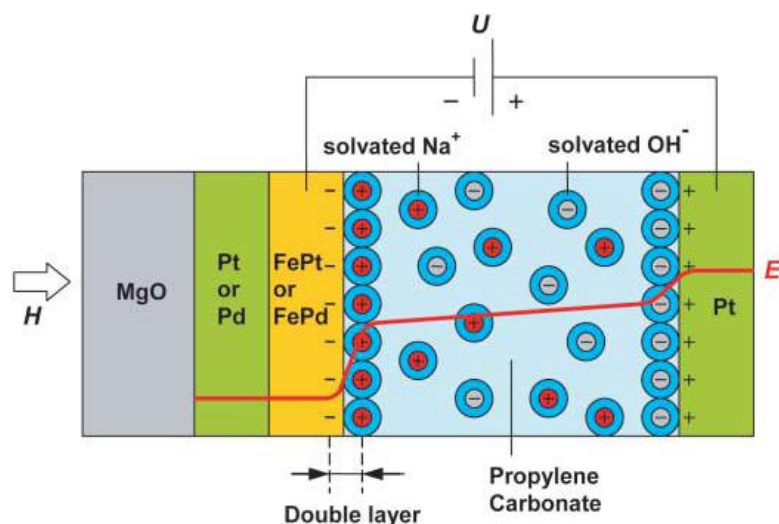


**Figure 1.9.** Schematic of the experimental setup under application of an electric field.<sup>98</sup>

Indeed, a coercivity reduction of 32% was recently accomplished in 600 nm thick, nanoporous Cu-Ni films prepared by micelle-assisted electrodeposition, a delicate and intricate electrochemical process.<sup>99</sup> Other properties such as the Curie Temperature and saturation magnetization have also been successfully manipulated by electric fields.<sup>100</sup>

Materials such as MgO and HfO<sub>2</sub> with a high relative permittivity, which results in a higher capacity per unit area and, therefore, boosts the capability to modulate carrier density with the same voltage, have been used as the dielectric layer. The effect, however, is volatile in the absence of an electric field. Ferroelectric materials have remnant polarization thus ensuring a nonvolatile effect and can greatly enlarge the relative permittivity.<sup>93</sup> In addition, their inverse piezoelectric and magnetostriction properties render strain-mediated magnetization switching possible.<sup>100,101</sup> Meanwhile, in multiferroic materials (ferromagnetic and ferroelectric), exchange bias coupling between the ferromagnetic and antiferromagnetic order can enable voltage controlled magnetic switching.<sup>101,103</sup> Another mechanism of voltage control of magnetism is orbital reconstruction which occurs through the orbital hybridization between a ferromagnetic metal and a dielectric or ferroelectric material or, optimally, at the interface of ferromagnetic and ferroelectric oxides.<sup>104</sup>

The mechanisms of voltage control of mechanisms mentioned above, namely carrier modulation, strain, exchange coupling, orbital reconstruction and electrochemical redox can also work synergistically or competitively in many cases rather than in a

separate and independent manner. Therefore, the investigation of their relationship and combined result is critical to thoroughly understanding and optimally employing their properties.

## 1.8. Objectives

Electrodeposition and the pursuit of alternative materials to replace the scarce and hazardous currently in use in high tech industry is at the heart of this thesis. For this reason, the Fe—Cu system presents an excellent candidate to answer modern demands in a sustainably and cost-efficient manner. Electrodeposition is coupled with other methods to achieve novel morphologies with solutions to modern day problems.

The main goals can thus be summarized as follows:

- i. Growth of continuous Fe—Cu films over a wide composition range from aqueous electrolytes and study of the influence that the bath constituents and plating conditions exert on the resulting films properties.
- ii. Combination of electrodeposition with colloidal templating to achieve patterned macropores and investigation of the effect that different pore diameters and Fe/Cu ratios have on the wetting behavior of the films.
- iii. Experimental investigation of the magneto-electric effects in hierarchically porous, relatively thick, Fe—Cu films.
- iv. Fabrication of submicron structures by electrodeposition onto pre-lithographed substrates prepared by electron beam lithography with the purpose of studying the growth of Fe—Cu into narrow cavities with sharply defined edges and discovering new magnetic phenomena related to size and geometry.
- v. Preparation of arrays of high aspect ratio rods and tubes of various diameters and creation of segments by electrodeposition into PC membranes. Another goal is to assess their potential photocatalytic activity.

## References

- [1] European Commission, 2017. Communication from the Commission to the European Parliament, the Council, the European Economic and Social Committee and the Committee of the Regions on the 2017 list of Critical Raw Materials for the EU, [online] Available from: <https://eur-lex.europa.eu/legal-content/EN/TXT/?uri=CELEX:52017DC0490> (Accessed 7 June 2018).
- [2] European Commission, 2008. Communication on the review of the list of critical raw materials for the EU and the implementation of the Raw Materials Initiative, [online] Available from: <https://eur-lex.europa.eu/legal-content/EN/TXT/?uri=CELEX:52014DC0297> (Accessed 7 June 2018).
- [3] European Parliament and Council, 2006. Regulation (EC) No 1907/2006 concerning the Registration, Evaluation, Authorisation and Restriction of Chemicals (REACH), establishing a European Chemicals Agency (ECHA), [online] Available from: <https://eur-lex.europa.eu/legal-content/EN/TXT/PDF/?uri=CELEX:32006R1907&from=EN> (Accessed 7 June 2018).
- [4] European Chemicals Agency, 2018. Candidate list of substances of very high concern for authorization, [online] Available from: <https://echa.europa.eu/candidate-list-table> (Accessed 7 June 2018).
- [5] Liu, F., Deng, Y., Han, X., Hu, W. and Zhong, C., 2016. Electrodeposition of metals and alloys from ionic liquids. *Journal of Alloys and Compounds*, 654, pp.163-170.
- [6] Gu, Y., Liu, J., Qu, S., Deng, Y., Han, X., Hu, W. and Zhong, C., 2017. Electrodeposition of alloys and compounds from high-temperature molten salts. *Journal of Alloys and Compounds*, 690, pp.228-238.
- [7] Gamburg, Y.D. and Zangari, G., 2011. *Theory and Practice of Metal Electrodeposition*. Springer, New York, NY.
- [8] Zangari, G., 2015. Electrodeposition of alloys and compounds in the era of microelectronics and energy conversion technology. *Coatings*, 5(2), pp.195-218.
- [9] Paunovic, M. and Schlesinger, M., 2006. *Fundamentals of electrochemical deposition*. Wiley-Interscience, Hoboken, NJ.



- [10] Pellicer, E., Varea, A., Pané, S., Sivaraman, K.M., Nelson, B.J., Suriñach, S., Baró, M.D. and Sort, J., 2011. A comparison between fine-grained and nanocrystalline electrodeposited Cu–Ni films. Insights on mechanical and corrosion performance. *Surface and Coatings Technology*, 205(23-24), pp.5285-5293.
- [11] Pané, S., Panagiotopoulou, V., Fusco, S., Pellicer, E., Sort, J., Mochnacki, D., Sivaraman, K.M., Kratochvil, B.E., Baró, M.D. and Nelson, B.J., 2011. The effect of saccharine on the localized electrochemical deposition of Cu-rich Cu–Ni microcolumns. *Electrochemistry Communications*, 13(9), pp.973-976.
- [12] Zajkoska, S.P., Mulone, A., Hansal, W.E., Klement, U., Mann, R. and Kautek, W., 2018. Alkoxylated  $\beta$ -Naphthol as an additive for tin plating from chloride and methane sulfonic acid electrolytes. *Coatings*, 8(2), p.79.
- [13] Nicolenco, A., Tsyntsar, N. and Cesiulis, H., 2017. Fe (III)-based ammonia-free bath for electrodeposition of Fe-W alloys. *Journal of the Electrochemical Society*, 164(9), pp.D590-D596.
- [14] Esteves, M.C., Sumodjo, P.T. and Podlaha, E.J., 2011. Electrodeposition of CoNiMo thin films using glycine as additive: anomalous and induced codeposition. *Electrochimica Acta*, 56(25), pp.9082-9087.
- [15] Banik, S.J. and Akolkar, R., 2015. Suppressing dendritic growth during alkaline zinc electrodeposition using polyethylenimine additive. *Electrochimica Acta*, 179, pp.475-481.
- [16] Yaroshevsky, A. A., 2006. Abundances of chemical elements in the Earth's crust. *Geochemistry International*, 44(1), pp. 48-55.
- [17] Andrews, N. C., 2008. Forging a field: the golden age of iron biology. *Blood*, 112(2), pp. 219-230.
- [18] Pepperhoff, W. and Acet, M., 2001. *Constitution and magnetism of iron and its alloys*. Springer-Verlag Berlin Heidelberg.

- [19] Mathon, O., Baudelet, F., Itié, J. P., Polian, A., d'Astuto, M., Chervin, J. C. and Pascarelli, S., 2004. Dynamics of the magnetic and structural  $\alpha$ - $\epsilon$  phase transition in iron. *Physical Review Letters*, 93(25), pp. 255503.
- [20] Schlesinger, M. and Paunovic, M. eds., 2011. *Modern electroplating* (Vol. 55). John Wiley & Sons.
- [21] Panzeri, Gabriele, Accogli, A., Gibertini E., Rinaldi, C, Nobili, L. and Magagnin L., 2018. Electrodeposition of high-purity nanostructured iron films from Fe (II) and Fe (III) non-aqueous solutions based on ethylene glycol. *Electrochimica Acta*, 271, pp.576-581.
- [22] Böck, R. and Wulf, S. E., 2009. Electrodeposition of iron films from an ionic liquid (ChCl/urea/FeCl<sub>3</sub> deep eutectic mixtures). *Transactions of the IMF*, 87(1), pp.28-32.
- [23] Festa, R. A. and Thiele, D. J., 2011. Copper: an essential metal in biology. *Current Biology*, 21(21), pp. R877-R883.
- [24] Linder, M. C. and Hazegh-Azam, M., 1996. Copper biochemistry and molecular biology. *The American Journal of Clinical Nutrition*, 63(5), pp. 797S-811S.
- [25] Meyer, B. K., Polity, A., Reppin, D., Becker, M., Hering, P., Klar, P. J., Sander Th., Reindl, C., Benz, J., Eickhoff, M., Heiliger, C., Heinemann, M., Bläsing, J., Krost, A. Shokovets, S., Müller, C. and Ronning, C., 2012. Binary copper oxide semiconductors: From materials towards devices. *Physica Status Solidi (b)*, 249(8), pp. 1487-1509.
- [26] Borkow, G. and Gabbay, J., 2005. Copper as a biocidal tool. *Current Medicinal Chemistry*, 12(18), pp. 2163-2175.
- [27] Borkow, G. and Gabbay, J., 2009. Copper, an ancient remedy returning to fight microbial, fungal and viral infections. *Current Chemical Biology*, 3(3), pp. 272-278.
- [28] Luechinger, N. A., Athanassiou, E. K. and Stark, W. J., 2008. Graphene-stabilized copper nanoparticles as an air-stable substitute for silver and gold in low-cost ink-jet printable electronics. *Nanotechnology*, 19(44), pp. 445201.
- [29] Magdassi, S., Grouchko, M. and Kamyshny, A., 2010. Copper nanoparticles for printed electronics: routes towards achieving oxidation stability. *Materials*, 3(9), pp. 4626-4638.

- [30] Boom, R., De Boer, F. R., Niessen, A. K. and Miedema, A. R., 1983. Enthalpies of formation of liquid and solid binary alloys based on 3d metals: III. Alloys of iron. *Physica B+ C*, 115(3), pp. 285-309.
- [31] Porter, D. A., Easterling, K. E. and Sherif, M., 2009. *Phase Transformations in Metals and Alloys, (Revised Reprint)*. CRC press.
- [32] Turchanin, M. A., 2001. Thermodynamics of Liquid Alloys, and Stable and Metastable Phase Equilibria in the Copper—Iron System. *Powder Metallurgy and Metal Ceramics*, 40(7-8), pp. 337-353.
- [33] Ma, E., 2005. Alloys created between immiscible elements. *Progress in Materials Science*, 50(4), pp. 413-509.
- [34] Ma, E., Atzmon, M. and Pinkerton, F. E., 1993. Thermodynamic and magnetic properties of metastable  $\text{Fe}_x\text{Cu}_{100-x}$  solid solutions formed by mechanical alloying. *Journal of Applied Physics*, 74(2), pp. 955-962.
- [35] Chien, C. L., Liou, S., Kofalt, D., Yu, W., Egami, T., Watson, T. J. and McGuire, T. R., 1986. Magnetic properties of  $\text{Fe}_x\text{Cu}_{100-x}$  solid solutions. *Physical Review B*, 33(5), pp. 3247.
- [36] Kuch, W., Salvietti, M., Gao, X., Lin, M. T., Klaua, M., Barthel, J., Mohan, Ch. V. and Kirschner, J., 1998. Artificially ordered FeCu alloy superlattices on Cu (001). II. Spin-resolved electronic properties and magnetic dichroism. *Physical Review B*, 58(13), p.8556.
- [37] Ueda, Y. and Kikuchi, N., 1993. Structure and magnetic properties of electrodeposited Fe—Cu alloy films. *Japanese Journal of Applied Physics*, 32(4R), pp. 1779.
- [38] Noce, R. D., Gomes, O. D. M., De Magalhaes, S. D., Wolf, W., Guimarães, R. B., De Castro, A. C., Pires, M. J. M., Macedo, W. A. A., Givord, D. and Barthem, V. M. T. S., 2009. Magnetic properties of Fe—Cu alloys prepared by pulsed electrodeposition. *Journal of Applied Physics*, 106(9), pp. 093907.

- [39] Roy, M. K. and Verma, H. C., 2004. Mössbauer studies of Fe–Cu alloys prepared by electrodeposition. *Journal of magnetism and magnetic materials*, 270(1-2), pp. 186-193.
- [40] Li, Y., Jia, W.Z., Song, Y.Y. and Xia, X.H., 2007. Superhydrophobicity of 3D porous copper films prepared using the hydrogen bubble dynamic template. *Chemistry of Materials*, 19(23), pp.5758-5764.
- [41] Cardoso, D.S.P., Eugénio, S., Silva, T.M., Santos, D.M.F., Sequeira, C.A.C. and Montemor, M.F., 2015. Hydrogen evolution on nanostructured Ni–Cu foams. *RSC Advances*, 5(54), pp.43456-43461.
- [42] Guerrero, M., Zhang, J., Altube, A., García-Lecina, E., Roldan, M., Baró, M.D., Pellicer, E. and Sort, J., 2016. Room-temperature synthesis of three-dimensional porous ZnO@CuNi hybrid magnetic layers with photoluminescent and photocatalytic properties. *Science and Technology of Advanced Materials*, 17(1), pp.177-187.
- [43] Isarain-Chávez, E., Baró, M.D., Pellicer, E. and Sort, J., 2017. Micelle-assisted electrodeposition of highly mesoporous Fe–Pt nodular films with soft magnetic and electrocatalytic properties. *Nanoscale*, 9(45), pp.18081-18093.
- [44] Guerrero, M., Pané, S., Nelson, B.J., Baró, M.D., Roldán, M., Sort, J. and Pellicer, E., 2013. 3D hierarchically porous Cu–BiOCl nanocomposite films: one-step electrochemical synthesis, structural characterization and nanomechanical and photoluminescent properties. *Nanoscale*, 5(24), pp.12542-12550.
- [45] Pal, N. and Bhaumik, A., 2013. Soft templating strategies for the synthesis of mesoporous materials: Inorganic, organic–inorganic hybrid and purely organic solids. *Advances in Colloid and Interface Science*, 189, pp.21-41.
- [46] Pérez-Page, M., Yu, E., Li, J., Rahman, M., Dryden, D.M., Vidu, R. and Stroeve, P., 2016. Template-based syntheses for shape controlled nanostructures. *Advances in Colloid and Interface Science*, 234, pp.51-79.
- [47] Tsyntsar, N., Silkin, S., Cesiulis, H., Guerrero, M., Pellicer, E. and Sort, J., 2016. Toward uniform electrodeposition of magnetic Co–W mesowires arrays: direct versus pulse current deposition. *Electrochimica Acta*, 188, pp.589-601.

- [48] Zkale, B., Shamsudhin, N., Chatzipirpiridis, G., Hoop, M., Gramm, F., Chen, X., Martí, X., Sort, J., Pellicer, E. and Pané, S., 2015. Multisegmented FeCo/Cu nanowires: electrosynthesis, characterization, and magnetic control of biomolecule desorption. *ACS Applied Materials & Interfaces*, 7(13), pp.7389-7396.
- [49] Zhang, J., Agramunt-Puig, S., Del-Valle, N., Navau, C., Baró, M.D., Estradé, S., Peiró, F., Pané, S., Nelson, B.J., Sanchez, A., Nogués, J., Pellicer, E. and Sort, J., 2016. Tailoring staircase-like hysteresis loops in electrodeposited trisegmented magnetic nanowires: A strategy toward minimization of interwire interactions. *ACS Applied Materials & Interfaces*, 8(6), pp.4109-4117.
- [50] Pellicer, E., Cabo, M., Rossinyol, E., Solsona, P., Suriñach, S., Baró, M.D. and Sort, J., 2013. Nanocasting of mesoporous In-TM (TM= Co, Fe, Mn) oxides: Towards 3D diluted-oxide magnetic semiconductor architectures. *Advanced Functional Materials*, 23(7), pp. 900-911.
- [51] Petkovich, N.D. and Stein, A., 2013. Controlling macro-and mesostructures with hierarchical porosity through combined hard and soft templating. *Chemical Society Reviews*, 42(9), pp.3721-3739.
- [52] Hu, J., Abdelsalam, M., Bartlett, P., Cole, R., Sugawara, Y., Baumberg, J., Mahajan, S. and Denuault, G., 2009. Electrodeposition of highly ordered macroporous iridium oxide through self-assembled colloidal templates. *Journal of Materials Chemistry*, 19(23), pp.3855-3858.
- [53] Yuan, Y.F., Xia, X.H., Wu, J.B., Chen, Y.B., Yang, J.L. and Guo, S.Y., 2011. Enhanced electrochromic properties of ordered porous nickel oxide thin film prepared by self-assembled colloidal crystal template-assisted electrodeposition. *Electrochimica Acta*, 56(3), pp.1208-1212.
- [54] Yang, S.M., Jang, S.G., Choi, D.G., Kim, S. and Yu, H.K., 2006. Nanomachining by colloidal lithography. *Small*, 2(4), pp.458-475.
- [55] Zhang, G. and Wang, D., 2009. Colloidal lithography—the art of nanochemical patterning. *Chemistry—An Asian Journal*, 4(2), pp.236-245.

- [56] Yang, J.K., Cord, B., Duan, H., Berggren, K.K., Klingfus, J., Nam, S.W., Kim, K.B. and Rooks, M.J., 2009. Understanding of hydrogen silsesquioxane electron resist for sub-5-nm-half-pitch lithography. *Journal of Vacuum Science & Technology B: Microelectronics and Nanometer Structures Processing, Measurement, and Phenomena*, 27(6), pp.2622-2627.
- [57] Hu, W., Sarveswaran, K., Lieberman, M. and Bernstein, G.H., 2004. Sub-10 nm electron beam lithography using cold development of poly (methylmethacrylate). *Journal of Vacuum Science & Technology B: Microelectronics and Nanometer Structures Processing, Measurement, and Phenomena*, 22(4), pp.1711-1716.
- [58] Rudnik, E. and Chat, K., 2018. A brief review on bio-inspired superhydrophobic electrodeposited nickel coatings. *Transactions of the IMF*, 96(4), pp.185-192.
- [59] Cosgrove, T. ed., 2010. *Colloid science: principles, methods and applications*. Wiley-Blackwell, Hoboken, NJ.
- [60] Young, T., 1805. III. An essay on the cohesion of fluids. *Philosophical Transactions of the Royal Society of London*, 95, pp.65-87.
- [61] Wenzel, R.N., 1936. Resistance of solid surfaces to wetting by water. *Industrial & Engineering Chemistry*, 28(8), pp.988-994.
- [62] Cassie, A.B.D. and Baxter, S., 1944. Wettability of porous surfaces. *Transactions of the Faraday Society*, 40, pp.546-551.
- [63] Law, K.Y. and Zhao, H., 2016. *Surface Wetting: Characterization, Contact Angle, and Fundamentals*, Springer International Publishing Switzerland.
- [64] Bhushan, B. and Nosonovsky, M., 2010. The rose petal effect and the modes of superhydrophobicity. *Philosophical Transactions of the Royal Society of London A: Mathematical, Physical and Engineering Sciences*, 368(1929), pp.4713-4728.
- [65] Barthlott, W. and Neinhuis, C., 1997. Purity of the sacred lotus, or escape from contamination in biological surfaces. *Planta*, 202(1), pp.1-8.
- [66] Michael, N. and Bhushan, B., 2007. Hierarchical roughness makes superhydrophobic states stable. *Microelectronic Engineering*, 84(3), pp. 382-386.

- [67] Zhang, Y.L., Xia, H., Kim, E. and Sun, H.B., 2012. Recent developments in superhydrophobic surfaces with unique structural and functional properties. *Soft Matter*, 8(44), pp.11217-11231.
- [68] Darmanin, T., de Givenchy, E. T., Amigoni, S. and Guittard, F., 2013. Superhydrophobic surfaces by electrochemical processes. *Advanced Materials*, 25(10), pp.1378-1394.
- [69] Wang, H., Hu, Z., Zhu, Y., Yang, S., Jin, K. and Zhu, Y., 2017. Toward easily enlarged superhydrophobic materials with stain-resistant, oil–water separation and anticorrosion function by a water-based one-step electrodeposition method. *Industrial & Engineering Chemistry Research*, 56(4), pp.933-941.
- [70] Callister, W.D. and Rethwisch, D.G., 2014. *Materials science and engineering: an introduction*. John Wiley & Sons, New York, NY.
- [71] Quarterman, P., Sun, C., Garcia-Barriocanal, J., Mahendra, D.C., Lv, Y., Manipatruni, S., Nikonov, D.E., Young, I.A., Voyles, P.M. and Wang, J.P., 2018. Demonstration of Ru as the 4th ferromagnetic element at room temperature. *Nature Communications*, 9(1), p.2058.
- [72] Cullity, B. D. and Graham, C. D., 2011. *Introduction to magnetic materials*. Wiley-IEEE Press, Hoboken, NJ.
- [73] Hamann, H. F., Martin, Y. C. and Wickramasinghe, H. K., 2004. Thermally assisted recording beyond traditional limits. *Applied Physics Letters*, 84(5), pp.810-812.
- [74] del Moral, A., 2008. *Handbook of Magnetostriction and Magnetostrictive Materials*. Del Moral Publ., University of Zaragoza.
- [75] Lei, N., Park, S., Lecoeur, P., Ravelosona, D., Chappert, C., Stelmakhovych, O. and Holý, V., 2011. Magnetization reversal assisted by the inverse piezoelectric effect in Co-Fe-B/ferroelectric multilayers. *Physical Review B*, 84(1), p.012404.
- [76] Shiota, Y., Nozaki, T., Bonell, F., Murakami, S., Shinjo, T. and Suzuki, Y., 2012. Induction of coherent magnetization switching in a few atomic layers of FeCo using voltage pulses. *Nature Materials*, 11(1), p.39.

- [77] Roy, K., Bandyopadhyay, S. and Atulasimha, J., 2011. Hybrid spintronics and straintronics: A magnetic technology for ultra low energy computing and signal processing. *Applied Physics Letters*, 99(6), p.063108.
- [78] Takamura, Y., Shuto, Y., Funakubo, H., Kurosawa, M. K., Nakagawa, S. and Sugahara, S., 2017. Inverse-magnetostriction-induced switching current reduction of STT-MTJs and its application for low-voltage MRAM. *Solid-State Electronics*, 128, pp.194-199.
- [79] Cai, H., Kang, W., Wang, Y., Naviner, L. A. D. B., Yang, J. and Zhao, W., 2017. High Performance MRAM with Spin-Transfer-Torque and Voltage-Controlled Magnetic Anisotropy Effects. *Applied Sciences*, 7(9), p.929.
- [80] Fernández-Pacheco, A., Streubel, R., Fruchart, O., Hertel, R., Fischer, P., & Cowburn, R. P. (2017). Three-dimensional nanomagnetism. *Nature Communications*, 8, p.15756.
- [81] Raeis-Hosseini, N. and Rho, J., 2017. Metasurfaces based on phase-change material as a reconfigurable platform for multifunctional devices. *Materials*, 10(9), p.1046.
- [82] Pendry, J. B., Schurig, D. and Smith, D. R., 2006. Controlling electromagnetic fields. *Science*, 312(5781), pp.1780-1782.
- [83] Zhu, W. M., Liu, A. Q., Zhang, X. M., Tsai, D. P., Bourouina, T., Teng, J. H., Zhang, X.H., Guo, H.C., Tanoto, H., Mei, T., Lo, G. Q. and Kwong, D. L., 2011. Switchable magnetic metamaterials using micromachining processes. *Advanced Materials*, 23(15), pp.1792-1796.
- [84] Borschel, C., Messing, M. E., Borgström, M. T., Paschoal Jr, W., Wallentin, J., Kumar, S., Mergenthaler, K., Deppert, K., Canali, C. M., Pettersson, H, Samuelson, L. and Ronning, C., 2011. A new route toward semiconductor nanospintronics: highly Mn-doped GaAs nanowires realized by ion-implantation under dynamic annealing conditions. *Nano Letters*, 11(9), pp.3935-3940.
- [85] Martín-González, M. S., Briones, F., García-Martín, J. M., Montserrat, J., Vila, L., Faini, G., Testa, A. M., Fiorani, D. and Rohrmann, H., 2010. Nano-patterning of



perpendicular magnetic recording media by low-energy implantation of chemically reactive ions. *Journal of Magnetism and Magnetic Materials*, 322(18), pp.2762-2768.

[86] Maziewski, A., Mazalski, P., Kurant, Z., Liedke, M. O., McCord, J., Fassbender, J., Ferré, J., Mougin, A., Wawro A., Baczewski L. T., Rogalev, A., Wilhelm, F. and Gemming T., 2012. Tailoring of magnetism in Pt/Co/Pt ultrathin films by ion irradiation. *Physical Review B*, 85(5), p.054427.

[87] Liu, C., Yu, C., Hashimoto, N., Ohnuki, S., Ando, M., Shiba, K. and Jitsukawa, S., 2011. Micro-structure and micro-hardness of ODS steels after ion irradiation. *Journal of Nuclear Materials*, 417(1-3), pp.270-273.

[88] Devolder, T., Chappert, C., Mathet, V., Bernas, H., Chen, Y., Jamet, J. P. and Ferré, J., 2000. Magnetization reversal in irradiation-fabricated nanostructures. *Journal of Applied Physics*, 87(12), pp.8671-8681.

[89] Mikhaylovskiy, R. V., Hendry, E., Secchi, A., Mentink, J. H., Eckstein, M., Wu, A., Pisarev, R.V., Kruglyak, V.V., Katsnelson M.I., Rasing T. and Kimel, A. V., 2015. Ultrafast optical modification of exchange interactions in iron oxides. *Nature Communications*, 6, p.8190.

[90] Brataas, A., Kent, A. D. and Ohno, H., 2012. Current-induced torques in magnetic materials. *Nature Materials*, 11(5), p.372.

[91] Salinga, M., and Wuttig, M., 2011. Phase-change memories on a diet. *Science*, 332(6029), p.543-544.

[92] Song, C., Cui, B., Li, F., Zhou, X. and Pan, F., 2017. Recent progress in voltage control of magnetism: Materials, mechanisms, and performance. *Progress in Materials Science*, 87, p.33-82.

[93] Gilbert, D. A., Olamit, J., Dumas, R. K., Kirby, B. J., Grutter, A. J., Maranville, B. B., Arenholz, E., Borchers J. A. and Liu, K., 2016. Controllable positive exchange bias via redox-driven oxygen migration. *Nature Communications*, 7, p.11050.

[94] Grutter, A. J., Gilbert, D. A., Alaán, U. S., Arenholz, E., Maranville, B. B., Borchers, J. A., Suzuki, Y., Liu, K. and Kirby, B. J., 2016. Reversible control of magnetism in

La<sub>0.67</sub>Sr<sub>0.33</sub>MnO<sub>3</sub> through chemically-induced oxygen migration. *Applied Physics Letters*, 108(8), p.082405.

[95] Quintana, A., Menéndez, E., Isarain-Chávez, E., Fornell, J., Solsona, P., Fauth, F., Baró, M.D., Nogués, J., Pellicer, E. and Sort, J., 2018. Tunable magnetism in nanoporous CuNi alloys by reversible voltage-driven element-selective redox processes. *Small*, 14(21), p.1704396.

[96] Robbenolt, S.A., Quintana, A., Pellicer, E. and Sort, J., 2018. Large magnetoelectric effects mediated by electric-field-driven nanoscale phase transformations in sputtered (nanoparticulate) and electrochemically dealloyed (nanoporous) Fe–Cu films. *Nanoscale*, 10, pp.14570-14578

[97] Duan, C.G., Velez, J.P., Sabirianov, R.F., Zhu, Z., Chu, J., Jaswal, S.S. and Tsymbal, E.Y., 2008. Surface magnetoelectric effect in ferromagnetic metal films. *Physical Review Letters*, 101(13), pp.137201.

[98] Weisheit, M., Fähler, S., Marty, A., Souche, Y., Poinignon, C. and Givord, D., 2007. Electric field-induced modification of magnetism in thin-film ferromagnets. *Science*, 315(5810), pp.349-351.

[99] Quintana, A., Zhang, J., Isarain-Chávez, E., Menéndez, E., Cuadrado, R., Robles, R., Baró, M.D., Guerrero, M., Pané, S., Nelson, B.J. and Müller, C.M., 2017. Voltage-induced coercivity reduction in nanoporous alloy films: a boost toward energy-efficient magnetic actuation. *Advanced Functional Materials*, 27(32), p.1701904.

[100] Matsukura, F., Tokura, Y. and Ohno, H., 2015. Control of magnetism by electric fields. *Nature Nanotechnology*, 10(3), p.209.

[101] Ma, J., Hu, J., Li, Z. and Nan, C.W., 2011. Recent progress in multiferroic magnetoelectric composites: from bulk to thin films. *Advanced Materials*, 23(9), pp.1062-1087.

[102] Zhang, S., Zhao, Y.G., Li, P.S., Yang, J.J., Rizwan, S., Zhang, J.X., Seidel, J., Qu, T.L., Yang, Y.J., Luo, Z.L. and He, Q., 2012. Electric-field control of nonvolatile magnetization in Co<sub>40</sub>Fe<sub>40</sub>B<sub>20</sub>/Pb(Mg<sub>1/3</sub>Nb<sub>2/3</sub>)<sub>0.7</sub>Ti<sub>0.3</sub>O<sub>3</sub> structure at room temperature. *Physical Review Letters*, 108(13), p.137203.

[103] Wu, S.M., Cybart, S.A., Yu, P., Rossell, M.D., Zhang, J.X., Ramesh, R. and Dynes, R.C., 2010. Reversible electric control of exchange bias in a multiferroic field-effect device. *Nature materials*, 9(9), p.756.

[104] Cui, B., Song, C., Mao, H., Wu, H., Li, F., Peng, J., Wang, G., Zeng, F. and Pan, F., 2015. Magnetoelectric coupling induced by interfacial orbital reconstruction. *Advanced Materials*, 27(42), pp.6651-6656.

## Important highlights related to the experimental techniques

In the following, a brief overview of several experimental techniques used throughout the thesis is presented in order to elucidate some key concepts for an unfamiliar reader or in the case that a specific technique has been employed in a nonconventional way. A detailed treatment of the fundamentals is beyond the scope of the thesis and can be found in advanced textbooks.

### 2.1. Confocal laser scanning microscopy (CLSM)

Confocal scanning microscopy is a form of optical sectioning microscopy that seeks to overcome some of the inherent limitations of wide-field fluorescence microscopy. In a traditional epifluorescence microscope, a source (e.g. an arc lamp) generates full-spectrum light which, when directed through the objective lens by way of a fluorescence cube towards the specimen, can selectively illuminate it with specific wavelengths that excite a particular fluorophore (i.e. an intrinsically fluorescent or synthesized compound with a number of conjugated double bonds). The time required for a molecule to transition from the ground state to an excited state is in the order of femtoseconds. In good fluorophores, the transition back to the ground state is made through photon expulsion. The energy of the emitted photon is typically less than that of the absorbed photon due to vibrational relaxation and internal conversion. This is known as the Stokes shift. A portion of the emitted photons is then

collected by the objective and sent through the cube to the detector. The cube contains a dichroic mirror and barrier filter to prevent the exciting shorter wavelengths from reaching the detector.<sup>1</sup> One significant problem that arises with wide-field fluorescence microscopy is that the illumination causes the entire specimen thickness to fluoresce creating an out-of-focus blur which diminishes the in-focus details and reduces the contrast thus resulting in deteriorated image quality. Moreover, emitted light originating from planes deeper inside the specimen, where scattering probability is higher, will appear as if arriving from points closer to the surface thus leading to an inaccurate image. Finally, signals which are on top of each other cannot be seen separately and will be superimposed.

Marvin Minsky, known as one of the founders of artificial intelligence, was the first to patent and describe the confocal imaging idea.<sup>2,3</sup> In confocal microscopy, the specimen is imaged in sections acquired at different depths throughout the specimen thickness, thus allowing a three-dimensional reconstruction from the computational combination of the collected image section data. Therefore, the out-of-focus background is eliminated, z-axis resolution is higher, and the contrast is greater. Lateral resolution can also be improved beyond what conventional fluorescence microscopes can achieve.<sup>4</sup> Confocal microscopes compose the section images by consecutively scanning small regions and recording point intensities according to the xy-coordinates. The objective lens is used to transform a collimated plane wave created by a laser beam source into a converging spherical wave and the full numerical aperture of the lens is used to sharply focus the light onto a single point. This entails a longer acquisition time compared to wide-field techniques which acquire the entire image synchronously.<sup>4</sup> Acousto-optical tunable filters are used to modulate the wavelength and intensity of the laser and avoid the issue of bleaching while maintaining a high scan rate. Although confocal microscopy is widely utilized in biology, it has also found a niche in materials science and engineering to image surface topography and extract its roughness using specialized software. The resolution of confocal laser scanning microscope is possibly higher than a standard stylus profiler and provides a greater field of view and depth range than atomic force microscopy.

In **Chapter 3.1**, CLSM is used to assess the roughness of Fe–Cu films electrodeposited under different conditions.

## 2.2. Spectroscopic ellipsometry

Light is a transverse electromagnetic wave and the direction of the electric field vector is conventionally known as its polarization. A polarized wave is one that exhibits periodicity in the spatiotemporal behavior of its electric field vector. The most common polarization is elliptical, where the electric field vector outlines an ellipse on any plane intersecting and perpendicular to the direction of propagation, i.e. one that combines orthogonal components of arbitrary amplitude and phase (linear and circular polarizations also exist as special cases of elliptical polarization). If an electromagnetic wave is a superposition of randomly distributed polarizations it is said to be unpolarized. Ellipsometry measures the amplitude ratio  $\psi$  and phase difference  $\Delta$  between the two basis linear polarizations upon reflection off a specimen. These orthogonal components are known as p-polarized and s-polarized light waves and are parallel and perpendicular to the plane of incidence, respectively.<sup>5</sup> Ellipsometry is a nondestructive, high precision optical characterization technique with applications in semiconductors, biomaterials, real-time monitoring of film growth and evaluation of optical anisotropy.<sup>6</sup>

In a spectroscopic ellipsometer, the light source and the polarizer prepare a known polarization state of the incident light on the specimen and  $(\psi, \Delta)$  spectra are measured for a wavelength  $\lambda$  of light typically in the ultraviolet/visible region, though measurements in the infrared region are also commonly reported.<sup>7</sup> Since the polarization state is determined by light intensity, a known limitation of the technique is related to specimen roughness which promotes light scattering. Scattering reduces the intensity of the reflected light thereby increasing measurement errors, especially when roughness exceeds 30% of the measurement wavelength. The angle of incidence is determined according to the optical properties of the sample but must be oblique since p- and s-polarizations become indistinguishable at normal incidence. An additional advantage of the method is high thickness sensitivity though its spatial resolution is rather low with a spot size of several nanometers. The biggest drawback,

however, is that it is an indirect characterization method which requires the construction of an optical model for the specimen since  $(\psi, \Delta)$  values cannot be directly converted into optical constants. This model is defined by the optical constants and approximate layer thicknesses and involves rather complex analysis. Two optical constants, namely the refractive index  $n$  and extinction coefficient  $k$ , must be estimated and subsequently evaluated for fitness during model simulations. If the values fitted are realistic, i.e. if they fall within the expected range, the complex refractive index can be derived from **Equation 2.1**.<sup>6</sup>

$$N = n - ik \quad (i = \sqrt{-1}) \quad (2.1)$$

The complex dielectric constant  $\epsilon$  and absorption coefficient  $\alpha$  can then be easily calculated ( $\epsilon = N^2$  and  $\alpha = 4\pi k/\lambda$ ). From the optical constants and film layer thicknesses, reflectance and transmittance at different angles of incidence can also be determined. One of the most common practical uses of spectroscopic ellipsometry is to determine the thickness and the volume fraction of void (porosity) of porous silicon layers used in photonics.

In **Chapter 3.3**, ellipsometry measurements are aimed at estimating the inherent porosity of the Fe–Cu continuous films as compared to those patterned by colloidal lithography in an effort to render a hierarchically porous material.

### 2.3. Magneto-optical Kerr effect (MOKE)

The magneto-optical Kerr effect occurs when a linearly polarized light incident on a magnetized material experiences a rotation of the polarization plane, Kerr rotation, and a phase difference between the electric field components perpendicular and parallel to the plane of incidence as described by Kerr ellipticity. In a typical MOKE setup, light generated by a laser source passes through a polarizer and a photoelastic modulator (PEM) before reaching the surface of a non-transparent sample which is situated between two electromagnets. The reflected light, which has experienced a rotation in its plane of polarization, then passes through an analyzer polarizing filter and a photodiode detector, thus producing a signal. Any change in rotation, polarized amplitude or ellipticity can be detected and are converted into changes in light intensity by the analyzer. A lock-in amplifier is used to increase the contrast and

improve the signal-to-noise ratio.<sup>8</sup> The magnetic domain contrast is sensitive to the magnitude and the direction of magnetization. In fact, the Kerr effect is ideal for observing domain wall motion in real time. Local hysteresis loops can also be obtained by plotting the average intensity of the Kerr images against the external applied field. It should be noted that, in metals, only the surface magnetization for a penetration depth of a few tenths of nanometers can be seen.<sup>8</sup>

Three possible configurations exist for carrying out MOKE measurements. In polar MOKE, the light impinges perpendicular to the surface and the magnetic field is applied out-of-plane. In longitudinal MOKE, the magnetization direction is in-plane and parallel to the plane of incidence. Finally, in transverse MOKE, the magnetization vector is in-plane with respect to the surface and normal to the plane of incidence.

For the magneto-electric measurements performed using a MOKE setup in **Chapter 3.3** of this thesis, the samples were mounted in a custom designed quartz cell filled with an ionic liquid (i.e. propylene carbonate with solvated  $\text{Na}^+$  and  $\text{OH}^-$  ions), as shown in **Figure 2.1**.

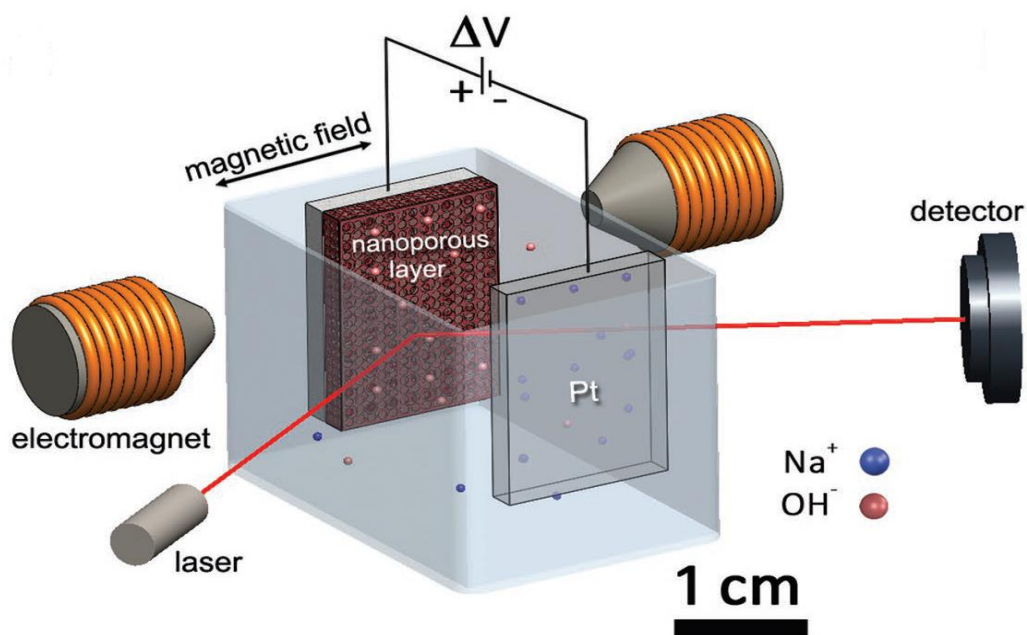


**Figure 2.1.** Experimental setup used for magneto-electric measurements with MOKE (courtesy of Dr. Jin Zhang)



## 2.4. Electron energy loss spectroscopy (EELS)

Transmission electron microscopy (TEM) is a powerful structural characterization technique with a high spatial resolution that can reach atomic dimensions in imaging and electron diffraction. The basic principles of operation are the same as with a light microscope, but electrons are used in place of light. A beam of electrons is generated from an emission source, which is usually a tungsten filament, and is focused by passing through a condenser lens. Since glass lenses would impede the electrons, electromagnetic lenses are used instead. Subsequently, the beam arrives at the specimen where a portion of it is transmitted depending on specimen thickness and electron transparency. Typically, specimens thinner than 100 nm are required for electrons to pass through them. The transmitted part then is focused and initially magnified by the objective lens to form an image onto a fluorescent screen or charge coupled device (CCD) camera. Additional intermediate lenses also serve to magnify the image. Owing to the fact that the wavelength of electrons is much smaller than that of light, the resolution obtained with TEM is many orders of magnitude better. In addition, elemental composition data can be obtained by energy-dispersive X-ray spectroscopy (EDX) or electron energy loss spectroscopy which are made possible by coupling a scanning transmission electron microscope (STEM) with an EDX detector or an electron spectrometer, respectively.

As the incident beam interacts with the atomic electrons of the specimen, this causes inelastic scattering of the high energy electrons, which lose energy (gained by the specimen electrons) and are slightly deflected from their path. The energy distribution of the inelastically scattered electrons provides information about the physical and chemical properties of the specimen. This is the basis of EELS, which constitutes a highly localized and sensitive technique that can be used for elemental mapping and quantitative analysis at atomic resolution and is ideal for light elements such as C and O.<sup>9</sup> The information obtained by EELS is very similar to that of X-ray absorption spectrometry (XAS) performed at the synchrotron though the spatial resolution of EELS is better (< 1 nm in Cs-aberrated STEM instruments). On the other hand, EDX measures the number and energy of X-ray photons emitted by the excited specimen

and is sensitive to heavier elements considering that light elements usually have low X-ray yield.<sup>10</sup> Therefore, the two techniques are considered complimentary.

In **Chapter 4**, EELS is used in combination with EDX to determine the elemental distribution of Fe, Cu and O throughout the thickness of compositionally graded Fe–Cu submicron structures. A lamella of approximately 60 nm was prepared for this measurement.

## References

- [1] Lichtman, J.W. and Conchello, J.A., 2005. Fluorescence microscopy. *Nature Methods*, 2(12), pp.910.
- [2] Minsky, M., 1961. Microscopy apparatus US patent 3013467. *USP Office, Ed. US*.
- [3] Minsky, M., 1988. Memoir on inventing the confocal scanning microscope. *Scanning*, 10(4), pp.128-138.
- [4] Conchello, J.A. and Lichtman, J.W., 2005. Optical sectioning microscopy. *Nature Methods*, 2(12), pp.920.
- [5] Tompkins, H. and Irene, E.A., 2005. *Handbook of ellipsometry*. William Andrew.
- [6] Fujiwara, H., 2007. Spectroscopic ellipsometry: principles and applications. John Wiley & Sons.
- [7] Kroning, A., Furchner, A., Aulich, D., Bittrich, E., Rauch, S., Uhlmann, P., Eichhorn, K.J., Seeber, M., Luzinov, I., Kilbey, S.M. and Lokitz, B.S., 2015. In situ infrared ellipsometry for protein adsorption studies on ultrathin smart polymer brushes in aqueous environment. *ACS Applied Materials & Interfaces*, 7(23), pp.12430-12439.
- [8] Hubert, A. and Schäfer, R., 2008. *Magnetic domains: the analysis of magnetic microstructures*. Springer Science & Business Media.
- [9] Hofer, F., Schmidt, F. P., Grogger, W., & Kothleitner, G., 2016. Fundamentals of electron energy-loss spectroscopy. *IOP Conference Series: Materials Science and Engineering*. IOP Publishing.
- [10] Li, W., & Ni, C., 2013. Electron Energy Loss Spectroscopy (EELS). *Encyclopedia of Tribology*. Springer, Boston, MA.

## **Results as a compilation of articles**

In this Chapter, the results attained in the thesis are presented as a compendium of articles. An extended abstract precedes each publication while a comprehensive discussion can be found in the articles.

### **3.1. Parametric aqueous electrodeposition study and characterization of Fe–Cu films**

In this work,  $\text{Fe}_x\text{Cu}_{1-x}$  ( $0 \leq x \leq 86$ ) coatings of several microns in thickness were synthesized by galvanostatic electrodeposition onto a gold coated substrate from an aqueous sulfate electrolyte under constant magnetic stirring. Citric acid, glycine and sodium gluconate were used as complexing agents in order to study the effect on film structure and morphology. It was shown that high-quality Fe-rich deposits were achieved from the gluconate containing electrolyte. On the other hand, excellent Cu-rich deposits were obtained from the glycine and citric acid baths with glycine leading to higher current efficiency while gluconate had a suppressing effect.

Current efficiency, roughness, deposit quality and composition were also shown to be highly influenced by bath pH, temperature and current density. The increase of temperature generally favored Cu deposition while also diminishing oxygen incorporation. The citric acid and glycine baths yielded improved results in the lower pH values while the opposite was true for the gluconate bath. The optimal ranges of operating current densities were determined for each case. Moreover, as assessed by X-ray photoemission spectroscopy, the oxygen was found to be confined to the uppermost surface with the oxygen peaks drastically decreasing upon removal of the surface layer.

In terms of microstructure, the deposits were found to be nanocrystalline and exhibited phase separation into Cu-rich face-centered cubic (fcc) and Fe-rich body centered cubic (bcc) phases with partial alloying as evidenced by Rietveld refinement. Average crystallite size was smaller for increased Cu content while microstrains were generally much smaller as compared to FeCu films prepared by mechanical alloying.

Finally, concerning the magnetic properties, the deposits were soft magnetic with rather square hysteresis loops while saturation magnetization increased with the Fe content.



## Parametric aqueous electrodeposition study and characterization of Fe–Cu films

Evangelia Dislaki<sup>a</sup>, Jordi Sort<sup>a,b,\*</sup>, Eva Pellicer<sup>a,§</sup>

<sup>a</sup> Departament de Física, Universitat Autònoma de Barcelona, E08193 Bellaterra, Spain.

<sup>b</sup> Institució Catalana de Recerca i Estudis Avançats (ICREA), Pg. Lluís Companys 23, E08010 Barcelona, Spain.

To whom correspondence should be addressed: \*[jordi.sort@uab.cat](mailto:jordi.sort@uab.cat);  
§[eva.pellicer@uab.cat](mailto:eva.pellicer@uab.cat)





# Parametric aqueous electrodeposition study and characterization of Fe–Cu films



Evangelia Dislaki<sup>a</sup>, Jordi Sort<sup>a,b,\*</sup>, Eva Pellicer<sup>a,\*</sup>

<sup>a</sup> *Departament de Física, Universitat Autònoma de Barcelona, E08193 Bellaterra, Spain*

<sup>b</sup> *Institució Catalana de Recerca i Estudis Avançats (ICREA), Pg. Lluís Companys 23, E08010 Barcelona, Spain*

## ARTICLE INFO

### Article history:

Received 28 December 2016

Received in revised form 8 February 2017

Accepted 16 February 2017

Available online 20 February 2017

### Keywords:

Fe-based alloy

Cu-based alloy

Co-deposition

Electroplating

Magnetic properties

## ABSTRACT

In this study, Fe<sub>x</sub>Cu<sub>1-x</sub> films over a wide composition range (0 ≤ x ≤ 86) were prepared from an aqueous sulfate electrolytic solution using three different complexing agents and variable plating conditions. The effect of parameters such as bath composition, current density and temperature on the elemental composition, morphology, structure and magnetic properties of the deposits was investigated. The electrochemical behavior was studied using cyclic voltammetry. High quality, smooth deposits with good substrate adhesion and minimized oxygen content were achieved. X-ray patterns indicate phase separation, though results from Rietveld analysis strongly suggest partial alloying. Magnetization dependence on Fe content is clearly demonstrated.

© 2017 Elsevier Ltd. All rights reserved.

## 1. Introduction

The Fe<sub>x</sub>Cu<sub>1-x</sub> alloy has attracted tremendous interest with respect to the magnetism of the face-centered cubic (fcc) phase of Fe (austenite), which can be obtained either via precipitation in a Cu matrix [1–3] or can be epitaxially grown on a Cu substrate [4,5]. However, the mutual solubility of Fe and Cu is quite low due to their positive enthalpy of mixing which has a theoretical value of 10.5 kJ mole<sup>-1</sup> [6]. Only ≈4 at% Fe can be dissolved into the Cu matrix with fcc structure and, conversely, ≈10 at% Cu can dissolve into the Fe matrix with body-centered cubic (bcc) structure near their respective melting points [7]. Metastable solid solutions have been prepared by different approaches, such as mechanical alloying [8–14] and physical vapor deposition techniques [15–17]. Single crystalline Fe<sub>x</sub>Cu<sub>1-x</sub> alloys over the entire composition range have been prepared successfully on a GaAs (001) substrate via molecular beam epitaxy for film thicknesses up to 8 nm [18]. Studies on the magnetic coupling and alloying interface effect of Fe–Cu multilayers [19–21] and superlattices [16,22] have also been carried out with potential applications in giant magnetoresistive (GMR) devices.

Electrodeposition offers an attractive alternative due to its simple, cost-effective and easy to operate set-up. Moreover, it works at ambient pressure and enables the growth of relatively

thick homogeneous coatings at fast deposition rates. The properties of deposits can be fine-tuned by modulating factors such as the composition, temperature and pH of the electrolytic bath and electroplating parameters such as agitation and deposition mode. However, due to the immiscibility of the system and the tendency of Fe to form oxides/hydroxides, existing literature related to Fe–Cu films prepared via electrodeposition is somewhat limited in scope. In few works, a relatively wide composition range of partially alloyed deposits of nanometer-thickness has been obtained by varying either the Cu or Fe salt concentrations [23,24]. This method was also used in one study focused on achieving high physical properties and enhanced corrosion resistance of thick coatings [25]. In another case, Mössbauer studies of metastable FeCu alloys in powder form targeted four different compositions attained by altering the Fe salt concentration [26]. Alternatively, the applied potential during pulsed electrodeposition mode was tuned in one study to produce the desired thin film composition and the magnetic behavior was investigated in relation to Fe content and temperature [27]. In another paper, Mössbauer studies were performed specifically on the CuFe alloy in powder form with a 72 at% Fe [28]. A paper on the electrodeposition of Cu-rich CuFe thin foams for supercapacitor electrodes was concentrated on the specific capacitance, the electrochemical response and the effect of thermal conditioning [29]. Finally, the effect of magnetic fields parallel to the electrode surface during deposition on the morphology and composition of the thin films has been reported [30].

\* Corresponding author.

E-mail addresses: [jordi.sort@uab.cat](mailto:jordi.sort@uab.cat) (J. Sort), [eva.pellicer@uab.cat](mailto:eva.pellicer@uab.cat) (E. Pellicer).



Additionally, the results of studies on the structural and magnetic properties vary significantly since these are dependent on the fabrication method and the experimental conditions. Importantly, the Fe concentration below which a single fcc structure is obtained, the concentration range of mixed bcc and fcc phase and the Fe concentration above which a single bcc phase is observed, differs for each fabrication method.

In this work, we have prepared micrometer-thick  $\text{Fe}_x\text{Cu}_{1-x}$  films over a wide composition range ( $0 \leq x \leq 86$ ) from three electrolytic solutions where a different complexing agent was used. Subsequently, extensive characterization of the composition, morphology, structure and magnetic properties of the deposits obtained was carried out. Optimized synthetic conditions leading to Fe-rich films with minimized oxygen content are highlighted.

## 2. Experimental

### 2.1. Instrumentation

Electrodeposition was performed in a three-electrode cell connected to a PGSTAT302N Autolab potentiostat/galvanostat (Ecochemie). A double junction  $\text{Ag}|\text{AgCl}$  ( $E = +0.210 \text{ V/SHE}$ ) acted as reference electrode (RE) (Metrohm AG) with a 3 M KCl inner solution and a 1 M  $\text{Na}_2\text{SO}_4$  outer solution. A Pt wire was used as a counter electrode (CE). Silicon/silicon dioxide ( $\text{SiO}_2$ ) substrates with a 10 nm Ti adhesion layer and a 90 nm Au seed layer served as the working electrode (WE) for deposit growth and for cyclic voltammetry (CV) studies. The working area was measured to be  $0.25 \pm 0.01 \text{ cm}^2$ .

### 2.2. Chemicals and electrolytic solutions

The electrolytes (100 mL) were prepared with Millipore Milli-Q water and ACS Reagent grade chemicals purchased from Sigma-Aldrich. The first solution contained 58.8 g/L  $(\text{NH}_4)_2\text{Fe}(\text{SO}_4)_2 \cdot 6\text{H}_2\text{O}$ , 1.25 g/L  $\text{CuSO}_4 \cdot 5\text{H}_2\text{O}$  (i.e., a  $[\text{Fe}(\text{II})]/[\text{Cu}(\text{II})]$  molar ratio of approximately 30), 20.2 g/L citric acid as a complexing agent, 0.2 g/L sodium dodecyl sulfate as a wetting agent and 0.46 g/L saccharine as a grain refining agent (bath A). The as prepared pH was 2.2 and samples were deposited at discrete working temperatures of 25 °C, 35 °C and 45 °C. For the second solution 7.9 g/L glycine was used instead as a complexing agent (keeping the concentration of complexing agent at 0.1 M) and the pH was adjusted from 3.7 to 2.2 with addition of  $\text{H}_2\text{SO}_4$  (bath B). Finally, for the third solution, 22.9 g/L sodium gluconate was the complexing agent and samples were deposited both from the as prepared solution with a pH of 4.1 (bath D) and after the adjustment of the pH to 2.2 with the addition of sulfuric acid (bath C). The stability of the solutions has been confirmed over the course of at least a few months.

### 2.3. Electrode preparation and procedure

Before electrodeposition, substrates were cleaned with acetone, followed by isopropanol and, finally, rinsed with Milli-Q water to remove any debris and residues. The electrolyte was de-aerated with argon gas before each deposition and mild stirring was applied by means of a magnetic stirring bar ( $\omega = 200 \text{ rpm}$ ). The galvanostatic mode was chosen for deposition with applied current densities in the range of  $-25 \text{ mA cm}^{-2}$  to  $-100 \text{ mA cm}^{-2}$ .

### 2.4. Characterization

Sample morphology and roughness were observed via Scanning Electron Microscopy using a Zeiss MERLIN Field Emission Scanning Electron Microscope (FE-SEM) and Confocal Laser Scanning Microscopy (CLSM) with the confocal 3D optical surface metrology

system LEICA DCM3D, respectively. The elemental composition was determined by Energy Dispersive X-ray Spectroscopy (EDXS) at an acceleration voltage of 15 kV. The mass of the deposited material (Fe and Cu amounts) was determined using a Perkin Elmer Optima 4300DV Inductively Coupled Plasma Optical Emission Spectrometer (ICP-OES). In preparation, the deposits were dissolved in test tubes containing 2 ml of nitric acid solution and one tube was filled solely with the solution to be used as a reference. The crystallographic structure of the deposits was studied by X-ray Diffraction (XRD). The XRD patterns were recorded on a Philips X'Pert diffractometer using  $\text{CuK}\alpha$  radiation and a Bragg-Brentano  $\theta$ - $2\theta$  configuration. Cell parameters, crystallite sizes and microstrains were evaluated by Rietveld refinement using the Materials Analysis Using Diffraction (MAUD) software [31]. In order to determine elemental oxidation states, X-ray Photoelectron Spectroscopy (XPS) analysis of several samples was carried out on a PHI 5500 Multitechnique System spectrometer from Physical Electronics, equipped with a monochromatic X-ray source placed perpendicular to the analyzer axis and calibrated using the  $3d^{5/2}$  line of Ag. The adventitious C1s line at 284.5 eV was used as a charge reference to calibrate the XPS spectra. Measurements for the composition depth profiles of six selected samples were obtained by sputtering the surface with an  $\text{Ar}^+$  ion source for 2 minutes ( $\sim 10$ – $15 \text{ nm}$  below the surface). The energy of the deconvoluted peaks was compared with the NIST XPS database. A linear background removal method was employed [32]. For the magnetic characterization samples were placed in a Vibrating Sample Magnetometer (VSM) from LOT-Quantum Design and hysteresis loops were recorded at room temperature, along the in-plane direction of the films, over an applied field range of  $-20 \text{ kOe}$  to  $20 \text{ kOe}$ .

## 3. Results and discussion

### 3.1. Cyclic voltammetry studies

CV curves were recorded from all electrolytic solutions at different temperatures in order to determine the current density range suitable for deposition. A single cycle was run for each case with a scan rate of  $0.05 \text{ V s}^{-1}$  and the potential sweep was initiated at  $-0.2 \text{ V}$ . Initially, the cathodic limit for bath A was varied between  $-0.8$  and  $-1.3 \text{ V}$  to identify where the reduction and oxidation of different species occurs. Moreover, an additional scan was performed with the exclusion of the Cu salt while preserving a constant concentration of the metal cations in the solution, thus facilitating the interpretation of the anodic peaks (Fig. 1a). As is evident in Fig. 1b, the onset of deposition occurs at approximately  $-0.7 \text{ V}$ . At higher cathodic limits, as the potential moves to more negative values, a steep increase in the absolute value of the current density is observed. A noisy signal indicates increased hydrogen co-evolution. After reversal of the scan direction, a single oxidation peak appears at cathodic limits lower than  $-1.1 \text{ V}$ , attributed to Cu species (peak P1). This can be verified by comparing with Fig. 1a where there is only Fe present in the solution and, consequently, there are no observable peaks at the  $-0.8 \text{ V}$  and  $-0.9 \text{ V}$  limits. The onset of deposition for Fe takes place around  $-1 \text{ V}$  and it can be seen that the Fe oxidation peak (peak P5) increases in intensity and shifts to the right for higher cathodic limits. Notably, as can be discerned from Fig. 1b, at the  $-1.1 \text{ V}$  limit a broadened oxidation peak appears (peak P2), shifted to the left relative to peak P1, which signifies the existence of a mixed phase. At the  $-1.2 \text{ V}$  limit, an increase in hydrogen co-evolution is remarked, accompanied by a shift of the oxidation peak P2 to the left and the appearance of a shoulder peak in the anodic scan (peak P3). Furthermore, a weak second oxidation peak appears (peak P4). When compared to the Fe oxidation peak 5 in Fig. 1a, peak 4

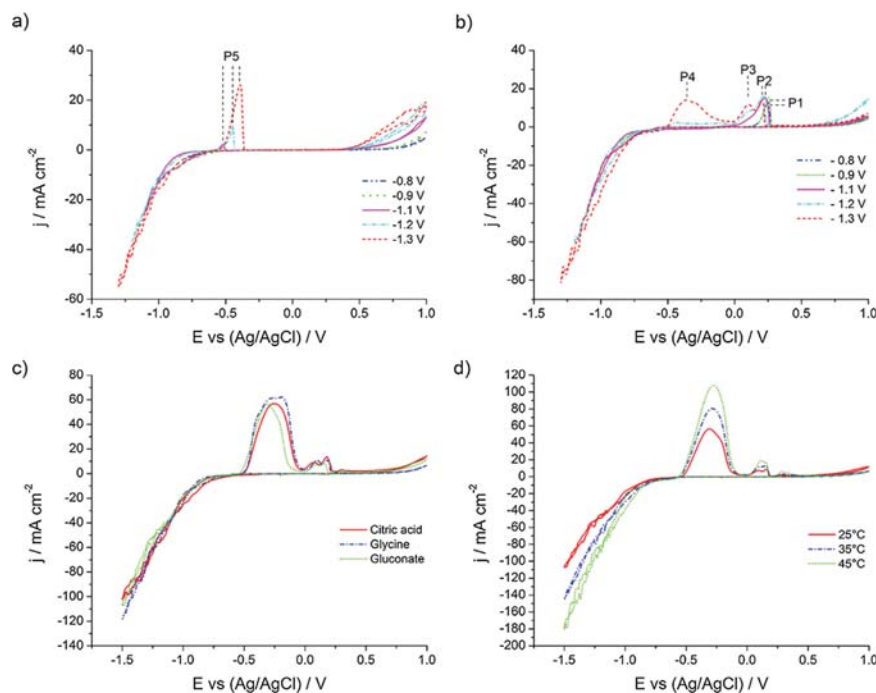


**Fig. 1.** Cyclic voltammeteries under stirring conditions from (a) electrolyte A with omission of the Cu salt (b) electrolyte A at different cathodic limits (c) electrolytes A, B and C at 25 °C and (d) electrolyte C at different temperatures.

corresponds in position but is substantially broadened indicating once again the presence of a mixed phase. At the highest cathodic limit of  $-1.3$  V, there is intense hydrogen co-evolution leading to introduction of significant amounts of oxides and hydroxides in the deposits. As result, a clear double-peak split (peaks P2 and P3) and a marked augmentation of peak P4 is seen in the anodic scan. These interpretations were in agreement with EDX elemental analysis.

After these preliminary tests, the cathodic limit was set to  $-1.5$  V for all experiments. As seen in Fig. 1c, the onset of deposition at room temperature is similar for electrolytes A, B and C at about  $-0.7$  V. As expected, in the anodic scan, a complex oxidation process takes place with multiple peaks denoting the formation of non-single phase deposits with variable chemical composition. According to the insights provided by this study an appropriate range of current densities was chosen for sample preparation.

With respect to the effect of temperature, similar trends were recorded for all electrolytes. As exemplified in Fig. 1d for the gluconate containing solution at pH = 2.2 (bath C), the increase of temperature to 35 °C and, subsequently, to 45 °C leads to an earlier onset of deposition and faster deposition rates. This is seen by an increase in the absolute value of current density, which indicates rapid deposition of large amounts of material within a narrow potential range. Consequently, this is accompanied by an increase of the height of the oxidation peaks.

### 3.2. Effect of complexing agents, current density and temperature

The effect of current density on deposit composition for the different electrolytes at 25 °C can be observed in Fig. 2. Error bars have been included, which represent the standard deviation for at least three replicas in each case. As expected, the increase of current density favors deposition of Fe, which is charge transfer controlled [33]. At large absolute values of current density, deposit composition becomes more difficult to control and oxygen incorporation increases in electrolytes A, B and C. This behavior

suggests an increase in the local pH in the vicinity of the cathode, which, although mitigated by the inclusion of boric acid, results in hydrogen evolution reactions and possibly in the formation and precipitation of iron hydroxides on the cathode, which are incorporated in the deposit. When the value of current density exceeds  $-75$  mA cm $^{-2}$  for the citric acid (A) and glycine solution (B) and  $-100$  mA cm $^{-2}$  for the gluconate electrolyte (C and D) deposit quality rapidly declines and poor adhesion to the substrate occurs.

For the citric acid and glycine electrolytes (baths A and B), samples over a wide composition range are obtained, though glycine appears to lead to deposits slightly richer in Cu (Fig. 2a and b). In the gluconate solution (baths C and D), the samples are mostly Fe-rich with more than 70 at% Fe. Copper-rich deposits are only obtained at current densities below  $-50$  mA cm $^{-2}$  as seen in Fig. 2c.

For comparison purposes, samples were also deposited with the as prepared pH for the glycine and gluconate electrolytes. In the case of glycine, at a pH value of 3.7, the deposit quality and substrate adhesion was extremely poor. For this reason, results from this bath were not considered. Contrarily, from the gluconate electrolyte fast deposition of high quality Fe-rich deposits was possible (bath D). Elemental composition was also easier to control at the 4.1 pH value across the entire range of applied current densities while oxygen incorporation was kept low. It is assumed that the gluconate ions in the solution act as an inhibitor to the deposition of Cu due to their complexation of Cu $^{2+}$  via a ligand carboxyl group [34]. At lower pH the stability of the copper-gluconate complex is compromised, which increases the number of free Cu $^{2+}$  ions and allows deposition of Cu-rich films at low current densities [34].

Next, the effect of temperature was studied by comparing the deposit composition at 25 °C, 35 °C and 45 °C for the different electrolytes when plating at a current density of  $-50$  mA cm $^{-2}$ , as shown in Fig. 3. The increase of temperature improves mobility and, thus, favors the deposition of Cu, which is mass transfer

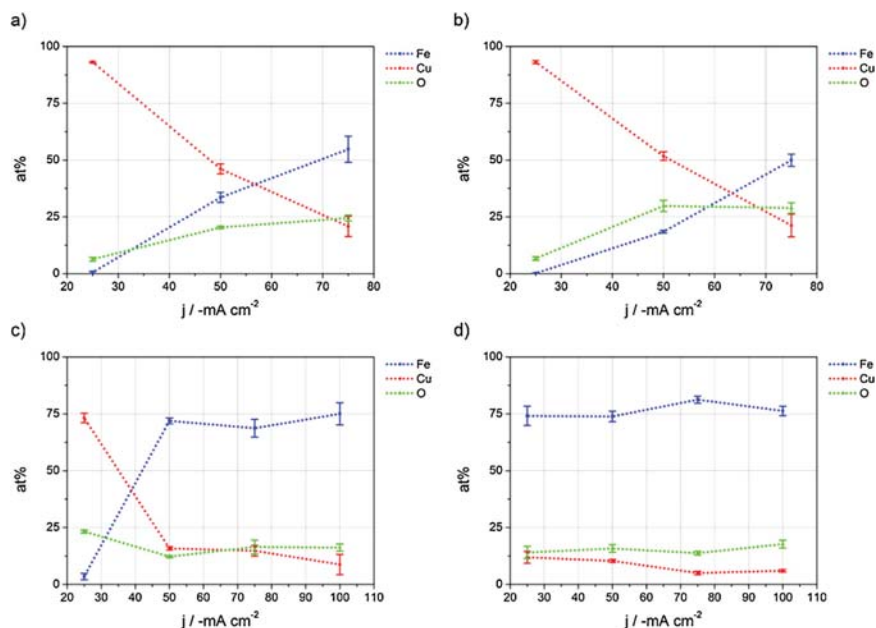


Fig. 2. Deposit composition dependence on current density at 25 °C for different electrolytes: (a) bath A (b) bath B (c) bath C (d) bath D.

controlled in the citric acid [35] and glycine solutions [36] (baths A and B). This is also accompanied by a decrease in the oxygen content, which is closely linked to the amount of Fe in the deposit (Fig. 3a and b). In the case of gluconate, the reverse trend is observed (Fig. 3c and 3d). The increase of temperature at the higher pH value (bath D) stabilizes the copper-gluconate complex and Fe deposition is favored while oxygen incorporation is limited (Fig. 3d). The adjustment of the pH weakens the stability of the copper-gluconate complexes and the rise of temperature

accelerates copper deposition (bath C). Therefore, at 35 °C and 45 °C copper is preferentially plated. However, this phenomenon is also marked by a significant elevation of the oxygen amount (Fig. 3c).

Pertaining to bath efficiency, this was found to vary substantially depending on current density and temperature across different electrolytes. Nevertheless, some assessments could be made based on the results from ICP-OES analysis of selected samples for the determination of the Fe and Cu mass deposited

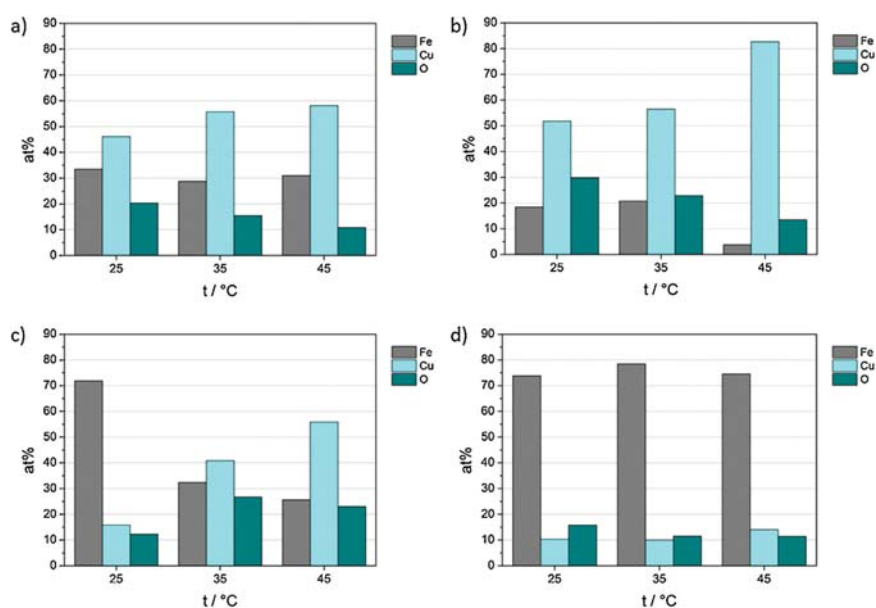


Fig. 3. Deposit composition dependence on temperature for different electrolytes: (a) bath A (b) bath B (c) bath C (d) bath D for deposits plated at a current density of  $-50 \text{ mA cm}^{-2}$ .

experimentally. These were compared to the theoretical mass of Fe and Cu deposited which was calculated assuming 100% cathodic efficiency using Faraday's law of electrolysis. In bath D, for example, at a current density of  $-50 \text{ mA cm}^{-2}$  and at a temperature of  $35^\circ\text{C}$ , an overall efficiency of approximately 41% was achieved. In bath C (pH adjusted to 2.2), however, at a current density of  $-50 \text{ mA cm}^{-2}$  and at a temperature of  $25^\circ\text{C}$ , total efficiency dropped to about 11%. Additionally, in bath C, at a current density of  $-75 \text{ mA cm}^{-2}$  and at a temperature of  $35^\circ\text{C}$ , the efficiency was calculated at about 20%. Finally, in bath A, at a current density of  $-25 \text{ mA cm}^{-2}$  and at a temperature of  $25^\circ\text{C}$ , the efficiency was around 18%. Furthermore, based on our observations during electrodeposition, bath D has the highest efficiency for Fe deposition whereas bath B is the most efficient for deposition of Cu. There are optimal current density and temperature combinations in each electrolyte which lead to the highest total efficiency, but these do not follow a linear relationship.

### 3.3. Surface characterization

From the images obtained using FE-SEM, the dependence of morphology on the plating parameters and electrolyte becomes apparent. Highly copper-rich deposits of approximately 99 at% Cu are granular and smooth with round, closely packed clusters of different size as seen in Fig. 4a. As the copper content decreases, nodular clusters are typically observed, which as is evident in

Fig. 4b, are formed much further apart. In the case of Fe-rich deposits from the gluconate electrolyte (bath D), which can be seen in Fig. 4c, the clusters are quite densely packed rendering a cauliflower-like morphology. Finally, Fe-rich deposits from the citric acid and glycine electrolytes tend to grow in the dendritic structure with significant oxygen incorporation (not shown). In any case, it was clear that the incorporation of Fe into Cu deposits brought remarkable changes in morphology.

Results from SEM imaging made it clear that for the Fe-rich samples roughness varied greatly depending on the applied current density and the temperature of the electrolyte. As shown previously, good quality samples with minimized oxygen content were obtained from the gluconate electrolyte at the 4.1 pH value (bath D). Therefore, a closer investigation of roughness variation for these deposits was deemed necessary. The 3D topographical images obtained using the CLSM technique are presented in Fig. 5. It was ascertained that increasing temperature led to gradually much smoother deposits while with respect to the applied current density there was an optimal value of  $-50 \text{ mA cm}^{-2}$ .

Finally, after establishing the optimal conditions required to produce high quality samples with low roughness and minimized oxygen content, it was deemed necessary to further research the oxidation phases present in the Fe-rich deposits and to determine whether oxygen is mostly present at the surface or throughout the entire sample volume. This was investigated by performing XPS

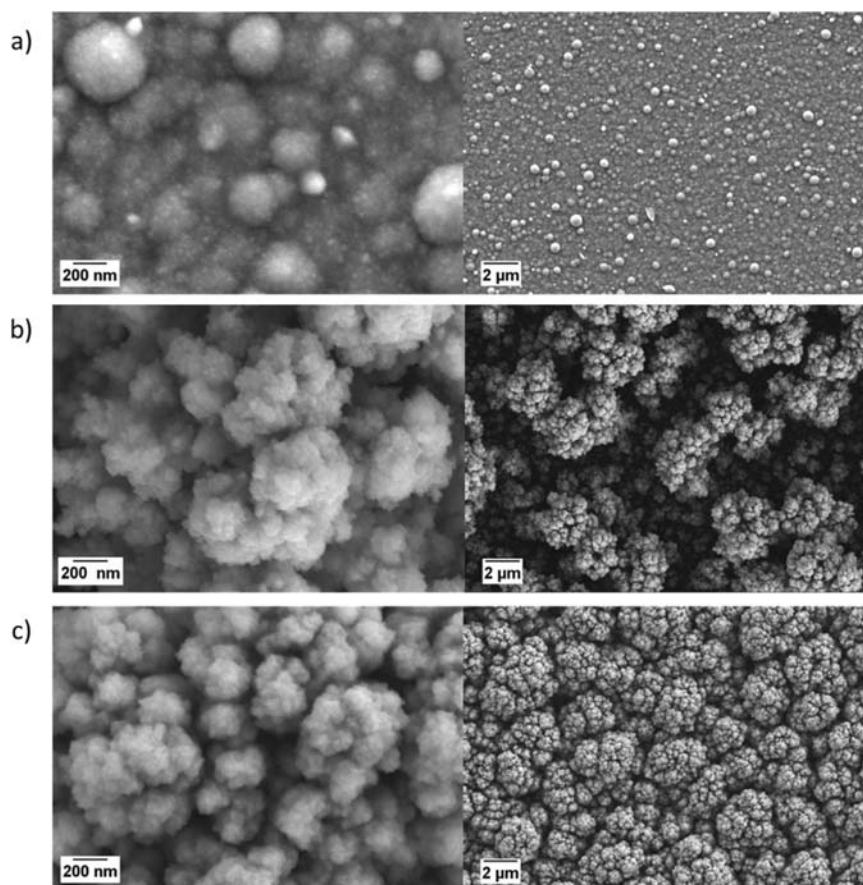


**Fig. 4.** Representative SEM images of films of distinct composition (a) almost pure Cu (99 at%) deposit obtained from bath B at  $25 \text{ mA cm}^{-2}$  current density at  $25^\circ\text{C}$  with a 36 min deposition time (b)  $\text{Fe}_{34}\text{Cu}_{66}$  from bath A at  $-50 \text{ mA cm}^{-2}$  at  $45^\circ\text{C}$  with an 18 min deposition time (c)  $\text{Fe}_{74}\text{Cu}_{14}$  from bath D at  $-50 \text{ mA cm}^{-2}$  at  $45^\circ\text{C}$  with an 18 min deposition time.

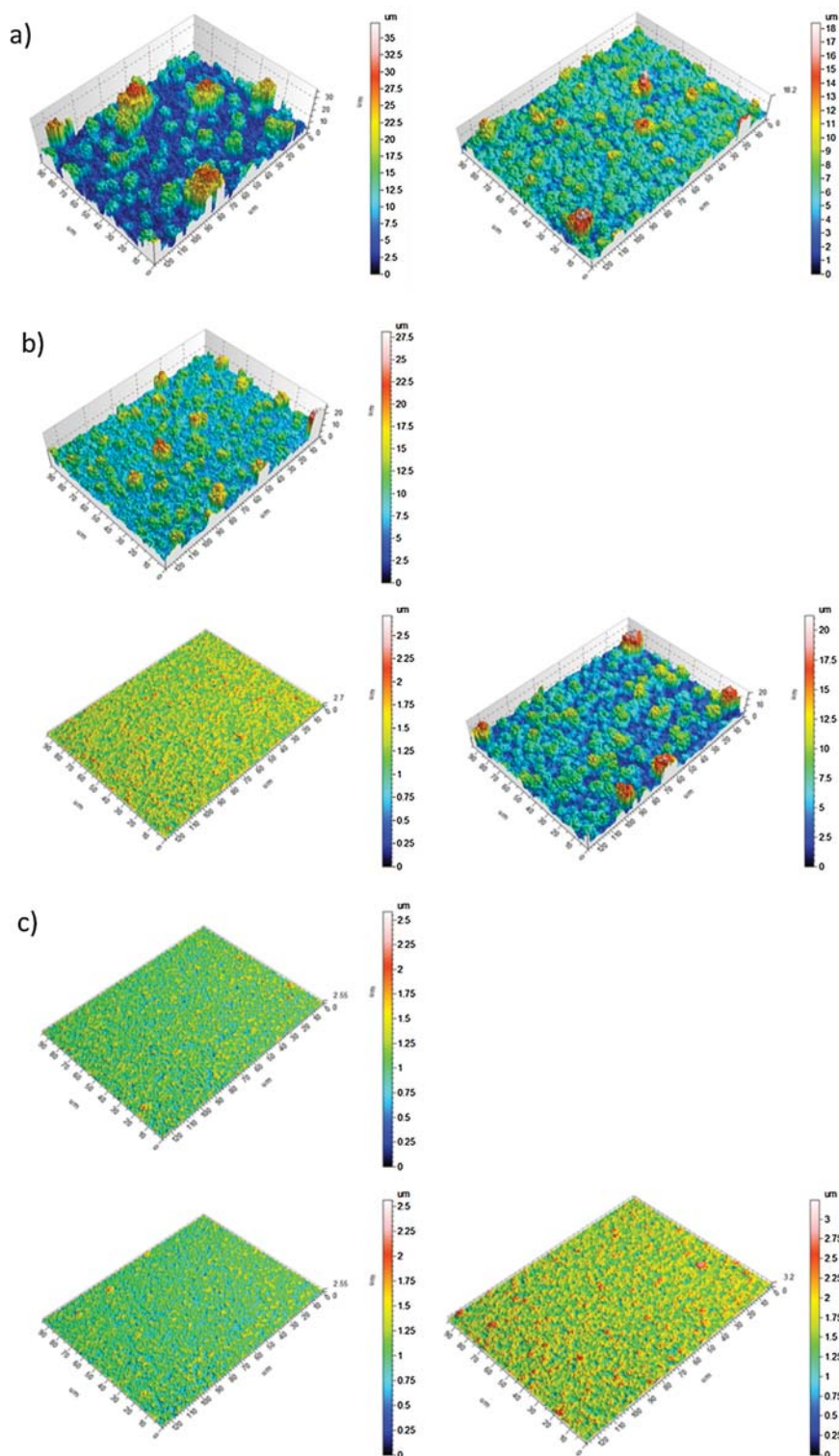


**Fig. 5.** CLSM 3D images illustrating roughness variation of Fe-rich films deposited from bath D at different current densities and temperatures: (a)  $\text{Fe}_{90}\text{Cu}_{10}$ ,  $-25 \text{ mA cm}^{-2}$  (left) and  $\text{Fe}_{88}\text{Cu}_{12}$ ,  $-50 \text{ mA cm}^{-2}$  (right) at  $25^\circ\text{C}$  (b)  $\text{Fe}_{78}\text{Cu}_{22}$ ,  $-25 \text{ mA cm}^{-2}$  (top left),  $\text{Fe}_{88}\text{Cu}_{12}$ ,  $-50 \text{ mA cm}^{-2}$  (bottom left) and  $\text{Fe}_{92}\text{Cu}_8$ ,  $-75 \text{ mA cm}^{-2}$  (bottom right) at  $35^\circ\text{C}$  (c)  $\text{Fe}_{71}\text{Cu}_{29}$ ,  $-25 \text{ mA cm}^{-2}$  (top left),  $\text{Fe}_{84}\text{Cu}_{16}$ ,  $-50 \text{ mA cm}^{-2}$  (bottom left) and  $\text{Fe}_{86}\text{Cu}_{14}$ ,  $-75 \text{ mA cm}^{-2}$  (bottom right) at  $45^\circ\text{C}$ .

analysis on six selected samples with high Fe amount since iron is considerably more prone to oxidation.

The general spectra of one sample chosen as a reference are exhibited in Fig. 6. It can be readily observed that the intensity of the O 1s peak significantly declines after Ar<sup>+</sup> sputtering. This trend was confirmed for all samples tested. After removal of the surface layer, the Fe and Cu amounts increase accordingly. For added clarity, the atomic percentages of Fe, Cu and O before and after sputtering for all samples are included in Table 1. From the detail spectra of Fe 2p presented in Fig. 7a, the doublets located between 707 eV and 719 eV (2p<sub>3/2</sub>) and between 720 eV and 732 eV (2p<sub>1/2</sub>) with shakeup satellites indicate that Fe is found mostly in an oxidized state (Fe<sup>2+</sup> and Fe<sup>3+</sup>). The small shoulder peak observed at around 706.5 eV (2p<sub>3/2</sub>), can be attributed to metallic iron (Fe<sup>0</sup>). However, after removing the surface by sputtering, the Fe<sup>0</sup> signal is much stronger, while the oxide peaks decrease. This points to the existence of iron oxide mainly on the surface while after sputtering with Ar<sup>+</sup> ions the main contributions in the XPS spectra correspond to Fe<sup>0</sup>. These results are also consistent with EDX quantification due to the large interaction volume in the order of μm in SEM, whereas XPS is very surface sensitive. In the detail spectra of Cu 2p seen in Fig. 7b, the peaks correspond to the Cu<sup>0</sup>/Cu<sup>+</sup>, Cu<sup>2+</sup> species and shakeup satellites. The very weak intensity of surface spectra means there is slight amount of Cu, whereas by removing the surface after sputtering, the increased intensity of the peaks associated with Cu<sup>0</sup>/Cu<sup>+</sup> suggests that the existent state of Cu is mainly metallic with small amount of oxides. Analysis of O 1s spectra, as presented in Fig. 7c, was performed by comparing with the spectra of Fe and Cu. After sputtering, the oxygen signal sharply decreases and the two main

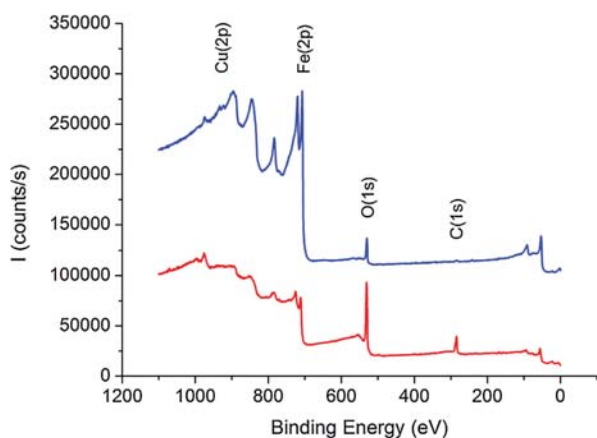


Fig. 6. XPS general surface profile of Fe-rich reference sample before (red curve) and after 2 min Ar<sup>+</sup> sputtering (blue curve).

Table 1

Atomic percentage of elements determined via XPS before and after surface sputtering.

At% Before Sputtering			At% After Sputtering		
Fe	Cu	O	Fe	Cu	O
26.80	0.27	72.93	81.93	1.28	16.79
28.69	0.66	70.65	76.70	2.36	20.95
21.16	15.51	63.33	72.45	8.93	18.62
27.07	4.47	68.45	63.47	6.96	29.57
29.74	2.72	67.55	76.74	3.70	19.56
30.72	13.14	56.14	76.52	11.98	11.49

O<sup>2-</sup> peaks correspond to the Cu oxides while the Fe oxide peak greatly diminishes. Additionally, the contribution from H<sub>2</sub>O (533.0 eV) can be found before and after sputtering indicating the absorption of water in the films. Therefore, it can be concluded that the surface was covered mainly by iron and copper oxides and after removal of the surface layer the amount of oxides drastically reduced, thus revealing the metallic states of Fe and Cu.

### 3.4. Crystallographic structure

The X-ray diffractograms obtained from samples with varying Fe/Cu ratio are illustrated in Fig. 8. The Miller indices of the peaks are also indicated. These results confirm phase separation with clear bcc and fcc peaks for Fe and Cu, respectively.

The XRD patterns were fitted using the Rietveld combined analysis tool provided by the MAUD software. As can be seen from the diffractograms, the films appear textured in the fcc (111) and bcc (110) planes evidenced by the higher relative intensity of these peaks compared to the theoretical intensities of isotropic bcc-Fe and fcc-Cu powders. The theoretical lattice constant for Cu fcc is 3.615 Å [37] and that of Fe bcc is 2.867 Å [38]. As is evident in Table 2, an increase in the amount of Fe is accompanied by a larger bcc volume fraction and a higher Cu amount signifies an elevated fcc volume fraction, respectively. The fcc lattice parameter of copper is also increased, which strongly suggests the inclusion of Fe atoms in the Cu matrix. This makes sense considering the atomic radii of Cu (1.45 Å) and Fe (1.56 Å) atoms. Moreover, it can be seen that the bcc crystallite size is progressively larger at higher bcc volume amounts. There is no clear trend, however, for fcc crystallite size. In any case, the values are within the nanosize domain, likely indicating that saccharine is an effective grain-refining agent in Fe-Cu codeposition. Finally, the microstrains, which is a microstructural parameter expressing the root-mean-square average deviation of the crystal d-spacings often caused by dislocations and other lattice defects, were found to be negligible and, indeed, the films were almost free of cracks. Low microstrains are typically reported in metallic films produced via electrodeposition [39–41], whereas for those produced using mechanical methods (e.g. ball milling) values of the order of 0.01 (or 1%) can be attained [42–44] due to the high dislocation densities resulting from the deformation processes.

### 3.5. Magnetic properties

Hysteresis loops of deposits with diverse at% Fe were recorded by VSM. The results of these measurements, for fields applied parallel to the film plane, are presented in Fig. 9. The y axis of magnetization has been normalized in emu g<sup>-1</sup>. As is evident in the graph, the saturation magnetization, M<sub>s</sub>, decreases monotonically as the Fe amount is gradually diminished. Note that M<sub>s</sub> for pure Fe at room temperature is 217.2 emu g<sup>-1</sup>. The obtained results are in good agreement with other experimental works on the magnetic properties of FeCu in the literature [8]. Importantly, films with a 6 at% Fe exhibit ferromagnetic behavior albeit with a very low saturation magnetization (~4 emu g<sup>-1</sup>). This is probably due to the occurrence of phase separation since fully alloyed fcc films with 6 at% Fe are typically paramagnetic at room temperature [13], although an enhanced magnetization is expected at low temperature for fcc-CuFe clusters with very small sizes [45]. Note that a 2–3% bcc-Fe (not detectable by XRD) would be enough to give this small value of M<sub>s</sub>. In addition, it is not possible to completely rule out that a small contribution to M<sub>s</sub> could come from the presence of ferrimagnetic surface iron oxides, as detected by XPS. Additionally, the films were found to be magnetically isotropic since similar hysteresis loops were recorded when applying the

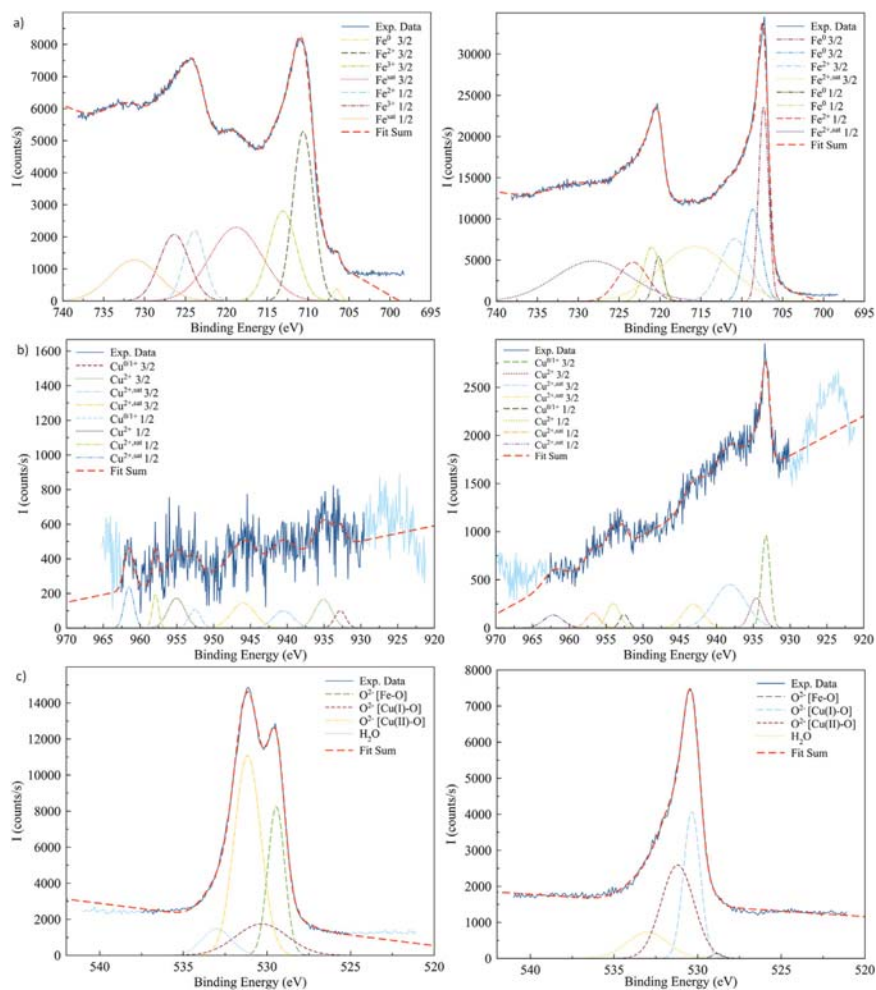


Fig. 7. Experimental and deconvoluted detail spectra at surface (left) and at  $\sim 10$ –15 nm below surface layer (right) of (a) Fe 2p, (b) Cu 2p and (c) O 1s bands of reference sample.

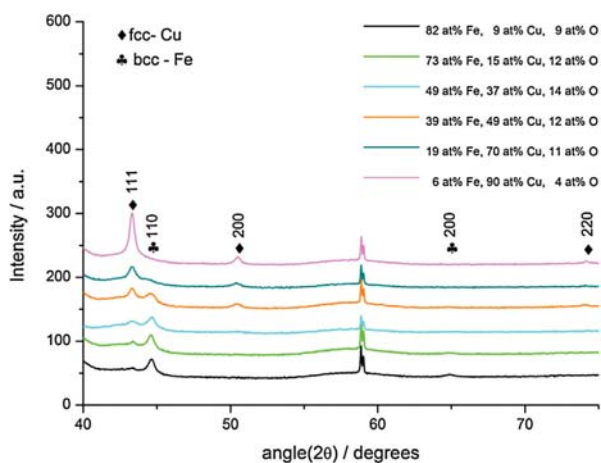


Fig. 8. X-ray Diffraction patterns for films of varying composition.

field along the in-plane and out-of-plane directions. The overall low coercivity values recorded ( $\sim 42$ – $154$  Oe) classify this material as soft magnetic and could find applications as structural components in magnetic micro- and nano-electromechanical systems (MEMS/NEMS).

#### 4. Conclusions

In this work,  $\text{Fe}_x\text{Cu}_{1-x}$  films were deposited within a wide composition range and the effect of three different complexing agents as well as of various plating conditions were systematically investigated. Subsequently, detailed morphological, structural and magnetic characterization was carried out. The choice of complexing agent was crucial in determining the derivable stoichiometry and the span of current densities leading to good adhesion and high film quality. Gluconate as a complexing agent leads to Fe-rich films because of suppression of Cu deposition, while in the case of citric acid and glycine higher current density favors Fe deposition. The increase of temperature typically favors Cu inclusion, although in the case of the gluconate electrolyte at the 4.1 pH value the effect is negligible. Film morphology is nodular with cauliflower-like cluster formation. In terms of roughness, higher temperature leads

**Table 2**  
Lattice parameters, crystallite size and microstrains of films of diverse compositions.

Composition according to EDX	Volume Fraction	Lattice Constant a		Crystallite Size		Microstrains	
		Fe-bcc (Å)	Cu-fcc (Å)	Fe-bcc (nm)	Cu-fcc (nm)	Fe-bcc	Cu-fcc
90 at% Fe 10 at% Cu	bcc:0.86 fcc:0.14	2.87702	3.63471	30.8	69.0	$1.30 \times 10^{-5}$	$5.08 \times 10^{-7}$
83 at% Fe 17 at% Cu	bcc:0.71 fcc:0.29	2.88396	3.63591	29.4	75.0	$1.18 \times 10^{-7}$	$7.70 \times 10^{-5}$
57 at% Fe 43 at% Cu	bcc:0.67 fcc:0.33	2.87110	3.62152	22.4	8.5	$1.81 \times 10^{-6}$	$5.56 \times 10^{-6}$
44 at% Fe 56 at% Cu	bcc:0.50 fcc:0.50	2.87632	3.62001	15.3	16.9	$1.78 \times 10^{-6}$	$6.25 \times 10^{-7}$
21 at% Fe 79 at% Cu	bcc:0.36 fcc:0.64	2.89166	3.62725	9.4	20.5	$4.74 \times 10^{-6}$	$7.45 \times 10^{-6}$
6 at% Fe 94 at% Cu	bcc:0.17 fcc:0.83	2.88664	3.61038	7.3	48.5	$4.17 \times 10^{-7}$	$2.03 \times 10^{-6}$

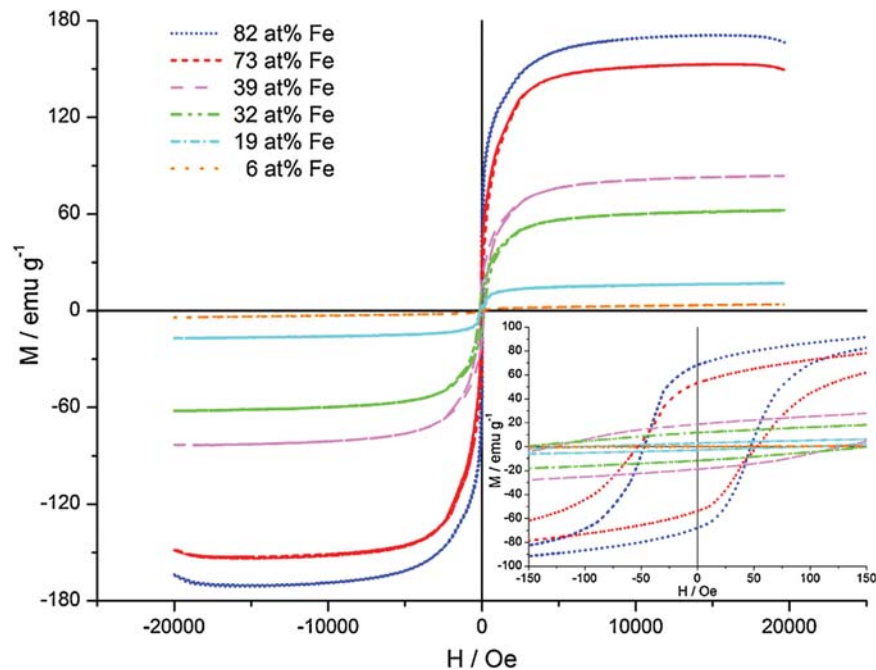


**Fig. 9.** Magnetic hysteresis loops obtained from films of varying Fe content. The inset shows a magnified detail at low fields.

to smoother deposits with more densely packed clusters. Current density is also a critical factor and an optimal value of  $-50 \text{ mA cm}^{-2}$  can be reported for the gluconate electrolyte. Oxygen is mostly found at the uppermost layer of the deposits where it most likely forms a passivation layer. Magnetite  $\text{Fe}_3\text{O}_4$  and hematite  $\text{Fe}_2\text{O}_3$  are the oxide phases present in the films. From the results of structural analysis, phase separation was confirmed with clear bcc and fcc diffraction peaks. However, the findings from Rietveld refinement strongly indicate partial alloying. Magnetic hysteresis measurements of the films revealed that saturation magnetization can be tuned by configuration of the at% Fe and, in contrast to previous studies, a low magnetic moment was observed even in the case of diminished Fe content.

#### Acknowledgements

This work was supported by the SELECTA (No. 642642) H2020-MSCA-ITN-2014 project. Partial financial support by the Spanish Government [Project MAT2014-57960-C3-1-R and associated FEDER], the Generalitat de Catalunya (2014-SGR- 1015) and the European Research Council (SPIN-PORICS 2014-Consolidator Grant, Agreement n° 648454) is acknowledged. E.P. is grateful to MINECO for the “Ramon y Cajal” contract (RYC-2012-10839).

#### References

- [1] Y. Tsunoda, N. Kunitomi, R.M. Nicklow, Magnetic structure of  $\gamma$ -Fe precipitates in a Cu matrix, *Journal of Physics F: Metal Physics* 17 (12) (1987) 2447.
- [2] Y. Tsunoda, Spin-density wave in cubic  $\gamma$ -Fe and  $\gamma$ - $\text{Fe}_{100-x}\text{Co}_x$  precipitates in Cu, *Journal of Physics: Condensed Matter* 1 (51) (1989) 10427.
- [3] P. Gorria, D. Martínez-Blanco, J.A. Blanco, M.J. Pérez, A. Hernando, L.F. Barquín, R.I. Smith, High-temperature induced ferromagnetism on  $\gamma$ -Fe precipitates in FeCu solid solutions, *Physical Review B* 72 (1) (2005) 014401.
- [4] W.A.A. Macedo, W. Keune, Magnetism of epitaxial fcc-Fe (100) films on Cu (100) investigated in situ by conversion-electron Mössbauer spectroscopy in ultrahigh vacuum, *Physical Review Letters* 61 (4) (1988) 475.
- [5] D. Li, M. Freitag, J. Pearson, Z.Q. Qiu, S.D. Bader, Magnetic phases of ultrathin Fe grown on Cu (100) as epitaxial wedges, *Physical Review Letters* 72 (19) (1994) 3112.
- [6] L. Kaufman, Coupled phase diagrams and thermochemical data for transition metal binary systems-III, *Calphad* 2 (2) (1978) 117–146.
- [7] M. Hansen, K. Anderko, H.W. Salzberg, Constitution of binary alloys, *Journal of the Electrochemical Society* 105 (12) (1958) 260C–261C.
- [8] A.R. Yavari, P.J. Desre, T. Benameur, Mechanically driven alloying of immiscible elements, *Physical Review Letters* 68 (14) (1992) 2235.
- [9] J. Eckert, J.C. Holzer, W.L. Johnson, Thermal stability and grain growth behavior of mechanically alloyed nanocrystalline Fe–Cu alloys, *Journal of Applied Physics* 73 (1) (1993) 131–141.
- [10] V.G. Harris, K.M. Kemner, B.N. Das, N.C. Koon, A.E. Ehrlich, J.P. Kirkland, J.C. Woicik, P. Crespo, A. Hernando, A.G. Escorial, Near-neighbor mixing and bond dilation in mechanically alloyed Cu-Fe, *Physical Review B* 54 (10) (1996) 6929.
- [11] P.J. Schilling, J.H. He, J. Cheng, E. Ma, Extended x-ray absorption fine structure of metastable bcc and fcc phases in mechanically alloyed Fe–Cu, *Applied Physics Letters* 68 (6) (1996) 767–769.



- [12] N. Wanderka, U. Czubyko, V. Naundorf, V.A. Ivchenko, A.Y. Yermakov, M.A. Uimin, H. Wollenberger, Characterization of nanoscaled heterogeneities in mechanically alloyed and compacted CuFe, *Ultramicroscopy* 89 (1) (2001) 189–194.
- [13] P. Gorria, D. Martínez-Blanco, J.A. Blanco, A. Hernando, J.S. Garitaonandia, L.F. Barquín, J. Campo, R.I. Smith, Invar effect in fcc-FeCu solid solutions, *Physical Review B* 69 (21) (2004) 214421.
- [14] A. Bachmaier, M. Kerber, D. Setman, R. Pippin, The formation of supersaturated solid solutions in Fe–Cu alloys deformed by high-pressure torsion, *Acta Materialia* 60 (3) (2012) 860–871.
- [15] C.L. Chien, S. Liou, D. Kofalt, W. Yu, T. Egami, T.J. Watson, T.R. McGuire, Magnetic properties of  $\text{Fe}_x\text{Cu}_{100-x}$  solid solutions, *Physical Review B* 33 (5) (1986) 3247.
- [16] W. Kuch, M. Salviati, X. Gao, M.T. Lin, M. Klaua, J. Barthel, C.V. Mohan, J. Kirschner, Artificially ordered FeCu alloy superlattices on Cu (001) II. Spin-resolved electronic properties and magnetic dichroism, *Physical Review B* 58 (13) (1998) 8556.
- [17] R.D. Desautels, C. Shueh, K.W. Lin, J.W. Freeland, J. van Lierop, Dynamical freezing, magnetic ordering, and the magnetocaloric effect in nanostructured Fe/Cu thin films, *Applied Physics Letters* 108 (17) (2016) 172410.
- [18] Z. Tian, C.S. Tian, L.F. Yin, D. Wu, G.S. Dong, X. Jin, Z.Q. Qiu, Magnetic ordering and anisotropy of epitaxially grown  $\text{Fe}_x\text{Cu}_{1-x}$  alloy on GaAs (001), *Physical Review B* 70 (1) (2004) 012301.
- [19] Ö.F. Bakkaloglu, A magnetic study of sputtered Fe/Cu multilayer films, *Journal of Magnetism and Magnetic Materials* 182 (3) (1998) 324–328.
- [20] A. Roig, X.X. Zhang, R. Zuberek, J. Tejada, E. Molins, Magnetic properties of FeCu multilayers, *Journal of Magnetism and Magnetic Materials* 140 (1995) 559–560.
- [21] T. Sakai, G. Oomi, K. Okada, K. Takanashi, K. Saito, H. Fujimori, Effect of pressure on the giant magnetoresistance of Fe/Cu magnetic multilayer, *Physica B: Condensed Matter* 237 (1997) 275–277.
- [22] W.H. Schreiner, D.H. Mosca, S.R. Teixeira, N. Mattoso, Epitaxial Fe/Cu superlattices on Si (111), *Journal of Applied Physics* 72 (12) (1992) 5682–5686.
- [23] Y. Ueda, N. Kikuchi, Structure and magnetic properties of electrodeposited Fe–Cu alloy films, *Japanese Journal of Applied Physics* 32 (4R) (1993) 1779.
- [24] J.M. Williams, H.J. Blythe, V.M. Fedosyuk, An investigation of electrodeposited granular CuFe alloyed films, *Journal of Magnetism and Magnetic Materials* 155 (1) (1996) 355–357.
- [25] V.G. Revenko, V.V. Pershutin, A.I. Shkorpelo, G.P. Chernova, N.L. Bogdashkina, Electroplating of Iron–Copper Coatings, *Protection of Metals* 38 (4) (2002) 377–381.
- [26] M.K. Roy, H.C. Verma, Mössbauer studies of Fe–Cu alloys prepared by electrodeposition, *Journal of Magnetism and Magnetic Materials* 270 (1) (2004) 186–193.
- [27] R.D. Noce, O.D.M. Gomes, S.D. de Magalhães, W. Wolf, R.B. Guimarães, A.C. De Castro, M.J.M. Pires, W.A.A. Macedo, D. Givord, V.M.T.S. Barthem, Magnetic properties of Fe–Cu alloys prepared by pulsed electrodeposition, *Journal of Applied Physics* 106 (9) (2009) 93907.
- [28] H.C. Verma, Mössbauer studies of CuFe–72% alloy, *Indian Journal of Pure and Applied Physics* 45 (10) (2007) 851–855.
- [29] G.A. Lange, S. Eugénio, R.G. Duarte, T.M. Silva, M.J. Carmezim, M.D.F. Montemor, Characterisation and electrochemical behaviour of electrodeposited Cu–Fe foams applied as pseudocapacitor electrodes, *Journal of Electroanalytical Chemistry* 737 (2015) 85–92.
- [30] M. Merikhi, G. Nabiyouni, B. Ghanbari, Effect of Magnetic Field on Surface Morphology and Magnetic Properties of FeCu/Cu Nano layers Prepared by Electrodeposition Technique: Investigation of Magneto-hydrodynamic Effect, *Journal of Nanostructures* 5 (4) (2015) 409–414.
- [31] L. Lutterotti, P. Scardi, Simultaneous structure and size–strain refinement by the Rietveld method, *Journal of Applied Crystallography* 23 (4) (1990) 246–252.
- [32] M. Repoux, Comparison of background removal methods for XPS, *Surface and Interface Analysis* 18 (7) (1992) 567–570.
- [33] I. Tabakovic, S. Riemer, N. Jayaraju, V. Venkatasamy, J. Gong, Relationship of  $\text{Fe}^{2+}$  concentration in solution and current efficiency in electrodeposition of CoFe films, *Electrochimica Acta* 58 (2011) 25–32.
- [34] S.A. El Rehim, S.M. Sayyah, M.M. El Deeb, Electroplating of copper films on steel substrates from acidic gluconate baths, *Applied Surface Science* 165 (4) (2000) 249–254.
- [35] S. Rode, C. Henninot, C. Vallières, M. Matlosz, Complexation chemistry in copper plating from citrate baths, *Journal of the Electrochemical Society* 151 (6) (2004) C405–C411.
- [36] J.C. Ballesteros, E. Chainet, P. Ozil, Y. Meas, G. Trejo, Electrocrystallization of copper from non-cyanide alkaline solution containing glycine, *International Journal of Electrochemical Science* 6 (2011) 1597–1616.
- [37] H.M. Otte, Lattice Parameter Determinations with an X-Ray Spectrogoniometer by the Debye-Scherrer Method and the Effect of Specimen Condition, *Journal of Applied Physics* 32 (8) (1961) 1536–1546.
- [38] P.M. Woodward, E. Suard, P. Karen, Structural tuning of charge, orbital, and spin ordering in double-cell perovskite series between  $\text{NdBaFe}_2\text{O}_5$  and  $\text{HoBaFe}_2\text{O}_5$ , *Journal of the American Chemical Society* 125 (29) (2003) 8889–8899.
- [39] L. Lu, N.R. Tao, L.B. Wang, B.Z. Ding, K. Lu, Grain growth and strain release in nanocrystalline copper, *Journal of Applied Physics* 89 (11) (2001) 6408–6414.
- [40] T. Mahalingam, J.S.P. Chitra, J.P. Chu, P.J. Sebastian, Preparation and microstructural studies of electrodeposited  $\text{Cu}_2\text{O}$  thin films, *Materials Letters* 58 (11) (2004) 1802–1807.
- [41] T. Mahalingam, V.S. John, L.S. Hsu, Microstructural analysis of electrodeposited zinc oxide thin films, *Journal of New Materials for Electrochemical Systems* 10 (1) (2007) 9.
- [42] F.M. Lucas, B. Trindade, B.F. Costa, G. Le Caër, Mechanical alloying of Fe–Cu alloys from as-received and premilled elemental powder mixtures, *Key Engineering Materials* 230 (2002) 631–634.
- [43] P. Gorria, D. Martínez-Blanco, J.A. Blanco, M.J. Pérez, M.A. González, J. Campo, Magnetism and structure of Fe–Cu binary solid solutions obtained by high-energy ball milling, *Physica B: Condensed Matter* 384 (1) (2006) 336–340.
- [44] M. Krifa, M. Mhadhbi, L. Escoda, J. Saurina, J.J. Suñol, N. Llorca-Isern, C. Artieda-Guzmán, M. Khitouni, Phase transformations during mechanical alloying of Fe–30% Al–20% Cu, *Powder technology* 246 (2013) 117–124.
- [45] C. Cutrano, C. Lekka, Structural, magnetic and electronic properties of Cu–Fe nanoclusters by density functional theory calculations, *Journal of Alloys and Compounds* (2016), doi:<http://dx.doi.org/10.1016/j.jallcom.2016.11.425>.

### **3.2. Fabrication of sustainable hydrophobic and oleophilic pseudo-ordered macroporous Fe–Cu films with tunable composition and pore size via electrodeposition through colloidal templates**

Superhydrophobic/superoleophilic materials with excellent absorption capacity are highly desirable for water/oil separation devices which can be utilized in environmental cleaning after an oil spill reversing the devastating effects of oil pollution without negative ramifications connected with other currently employed methods. Therefore, porous materials are promising candidates due to their high surface-to-volume ratio which maximizes absorption while by tuning the pore size one can effectively separate oil not only from mixtures but, importantly, also from emulsions. Several methods are employed to render these materials superhydrophobic/oleophilic which are hampered by several disadvantages related to complex and expensive fabrication process, sophisticated lab equipment, problems with upscalability and use of toxic substances.

In this paper, the fabrication of superhydrophobic and oleophilic Fe–Cu films of a highly porous nature was targeted. The synthetic protocols previously established for the growth of continuous coatings were extrapolated for the preparation of Fe-rich and Cu-rich porous films by coupling electrodeposition with a versatile hard templating technique. Polystyrene colloidal spheres of three submicron sizes (200 nm, 350 nm and 500 nm) were utilized to create the porous network. The spheres were deposited through electrophoretic deposition which allows for a close-packed assembly with good uniformity. Dual roughness created by the pores and by nanosized features along the pore walls was instrumental in achieving the high water contact angles measured in all films without the need for post-treatment. This was confirmed by the significantly lower water contact angles reached for their continuous (unpatterned) counterparts. Conversely, oil contact angles were systematically low for all porous samples, namely between 13.0° and 18.9° upon contact and gradually decreasing.

Remarkably, for the 500 nm macro-pore size Fe<sub>85</sub>Cu<sub>15</sub> film, water contact angles were consistently above 150° and a low contact angle hysteresis were achieved. As a proof

of concept, the superhydrophobic films were used to remove motor oil droplets from water and the efficiency was assessed by gas chromatography-mass spectroscopy. This revealed a 60% initial absorption capacity which held at 40% after multiple removal/rinsing cycles. Notably, certain losses were inevitable due to the tendency of the oil droplets to adhere to the sides of the glass container. Finally, the submicron pore size is ideal for oil removal in emulsions.



## **Fabrication of sustainable hydrophobic and oleophilic pseudo-ordered macroporous Fe–Cu films with tunable composition and pore size via electrodeposition through colloidal templates**

Evangelia Dislaki,<sup>1,\*</sup> Juho Pokki<sup>2</sup>, Salvador Pané<sup>2</sup>, Jordi Sort<sup>1,3</sup>, Eva Pellicer<sup>1,\*</sup>

<sup>1</sup>Departament de Física, Universitat Autònoma de Barcelona, 08193 Bellaterra, Spain

<sup>2</sup>Institute of Robotics and Intelligent Systems, ETH Zurich, CH-8092, Zurich, Switzerland

<sup>3</sup>Institució Catalana de Recerca i Estudis Avançats (ICREA), Passeig Lluís Companys 23, 08010 Barcelona, Spain

E-mails: [evangelia.dislaki@uab.cat](mailto:evangelia.dislaki@uab.cat)

[eva.pellicer@uab.cat](mailto:eva.pellicer@uab.cat)





Contents lists available at ScienceDirect

Applied Materials Today

journal homepage: [www.elsevier.com/locate/apmt](http://www.elsevier.com/locate/apmt)

# Fabrication of sustainable hydrophobic and oleophilic pseudo-ordered macroporous Fe–Cu films with tunable composition and pore size via electrodeposition through colloidal templates

Evangelia Dislaki<sup>a,\*</sup>, Juho Pokki<sup>b</sup>, Salvador Pané<sup>b</sup>, Jordi Sort<sup>a,c</sup>, Eva Pellicer<sup>a,\*</sup>

<sup>a</sup> Departament de Física, Universitat Autònoma de Barcelona, E-08193 Bellaterra, Spain

<sup>b</sup> Institute of Robotics and Intelligent Systems, ETH Zurich, CH-8092, Zurich, Switzerland

<sup>c</sup> Institució Catalana de Recerca i Estudis Avançats (ICREA), Passeig Luíís Companys 23, E-08010 Barcelona, Spain

## ARTICLE INFO

### Article history:

Received 22 February 2018

Received in revised form 20 March 2018

Accepted 20 March 2018

### Keywords:

Electrodeposition

Porous films

Colloidal lithography

Wettability

Sustainability

## ABSTRACT

In this work, sustainable hydrophobic and oleophilic macroporous Fe–Cu films are fabricated using a straightforward, inexpensive and environmentally friendly two-step procedure which combines electrodeposition with the colloidal lithography technique. Elemental, morphological and structural characterization of the resulting pseudo-ordered meshes is carried out and wettability is assessed using contact angle measurements with respect to two distinct film compositions (3 at.% Fe vs 75–85 at.% Fe) and three different pore diameters (namely, 200 nm, 350 nm and 500 nm). Water contact angles are measured to be in the range of approximately 109.0–155.1° (without any post-surface functionalization) and a low contact angle hysteresis is observed in the superhydrophobic samples. The increase in the hydrophobic character of the films correlates well with an increase in surface roughness, whereas differences in composition play a minor role. For the superhydrophobic Fe-rich macroporous film, water–oil separation capability and recyclability are also demonstrated while the pore size is favorable for effective water–oil mixture and emulsion separation. The results shown here demonstrate that sustainable and affordable materials processed in a simple and cheap manner can be an asset for the removal of water-immiscible organic compounds from aqueous environments.

© 2018 Elsevier Ltd. All rights reserved.

## 1. Introduction

Wetting phenomena observed in nature such as the water-repellent, non-adhesive surface of lotus leaves have attracted much attention due to the wide array of potential biomimetic technological applications in self-cleaning and anti-corrosion surfaces [1]. The anti-wetting behavior of lotus leaves is based on roughness promoted by micro- and nanoscale hierarchical surface characteristics along with the hydrophobic properties of the surface wax. In addition, their non-sticky surface allows for the contaminants to be easily carried away by water droplets and, thus, involves a self-cleaning effect [2]. Furthermore, materials with switchable or antithetical wetting affinities, i.e. hydrophobic/oleophilic or hydrophilic/oleophobic can be utilized in oil–water separation applications such as tackling the environmental pollution caused by

frequent oil spill accidents [3–5]. Methods that have been routinely employed in handling oil spill accidents such as booms and skimmers, dispersants, in situ burning and bioremediation are generally costly, inefficient and often result in secondary pollution which can be devastating to aquatic life as well as to other organisms [6–9]. Therefore, the development of inexpensive, sustainable and reusable materials that can separate the water and oil phases in an efficient way and even retrieve precious oil resources has garnered significant research attention in recent years. These materials function either through filtration (e.g. metallic meshes, textiles and membranes) or absorption (e.g. particles, sponges and aerogels) [3–5].

Fabrication of special wetting surfaces has been generally focused on tuning the surface morphology and composition in order to enhance the wetting properties and improve the separating efficiency. Functionalization of metallic meshes and textiles generally involves dip- or spray coating with polymers and optionally incorporating nanoparticles, hydrothermal reaction, in situ growth of micro- and nanocrystals or thermal oxidation to increase roughness followed by further modification by chemical

\* Corresponding authors.

E-mail addresses: [evangelia.dislaki@uab.cat](mailto:evangelia.dislaki@uab.cat) (E. Dislaki), [eva.pellicer@uab.cat](mailto:eva.pellicer@uab.cat) (E. Pellicer).

<https://doi.org/10.1016/j.apmt.2018.03.007>

2352-9407/© 2018 Elsevier Ltd. All rights reserved.

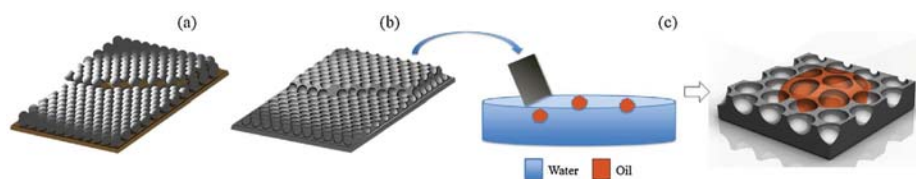


**Fig. 1.** Schematic representation of the work concept: (a) PS spheres assembled on the substrate, (b) electrodeposition of Fe–Cu followed by removal of the PS spheres, (c) removal of oil from water using the hydrophobic and oleophilic macroporous Fe–Cu film.

treatment [3–5]. These materials are generally used in the separation of layered oil/water mixtures. In the case of emulsions, polymeric membranes have been proposed where by configuring the pore size to be smaller or commensurate with that of the emulsified droplets (typically  $<20\ \mu\text{m}$ ), the water–oil emulsion can be separated since oil is allowed to pass through the pores and water is repelled [10].

However, the inherent difficulty of in situ removal of oil from water in the filtration scheme, in addition to the issue of potential fouling or blockage with decreasing pore size which leads to a decline of permeation, has signaled toward absorption as a more promising strategy. Highly porous materials are particularly targeted since the high surface-area-to-volume ratio leads to an increase of the capacity to absorb. Moreover, superhydrophobicity ensures water repellence, thereby enhancing oil absorption. Other desirable properties include eco-friendliness, reusability, recyclability, scalability and mechanical robustness. Nevertheless, many of the absorption materials currently described in literature can be difficult to handle, involve a complex preparation procedure, expensive precursors or specialized lab equipment (e.g. hydrothermal reaction, chemical vapor deposition, pyrolysis) and can also rely on subsequent treatment with toxic fluorinated compounds to reduce surface energy [3–5].

Several techniques exist for the preparation of porous metallic films such as dynamic template assisted electrodeposition [11], electron beam lithography [12] and colloidal templating [13]. Colloidal templating is a facile, cost-effective method of creating well-defined 3D porous structures by using 3D assembled colloids as a soft mask. Colloid size and assembly are critical factors that determine pore dimensions, wall and layer thickness and quality in terms of defect density. Various methods of packing techniques for monodisperse micro- and nanospheres such as vertical deposition [14], spin-coating [15], dip-coating [16], self-assembly [17], solvent evaporation [18], and electrophoretic deposition [19] have been reported in literature. Among these methods, electrophoretic deposition is an attractive option for achieving homogeneous coverage and assembly in a close-packed, oriented structure.

In this work, Fe–Cu porous coatings with hierarchical roughness and controllable pore dimensions were prepared using the colloidal templating technique coupled with electrodeposition from an environmentally-friendly electrolyte (Fig. 1a and b). Fe–Cu is a particularly beneficial system as it consists of elements that are very affordable, abundant and nonhazardous. Additionally, electrodeposition was chosen for the growth of the films due to several advantages compared to other methods. Specifically, electrodeposition involves a simple, low-cost setup, it can be operated in ambient conditions without the requirement of high vacuum and it enables the growth of relatively homogeneous coatings at fast rates. It also allows the creation of complex 3D geometries which are often unattainable by physical methods such as in the case of the patterned multi-layer porous architecture described in this work. The continuous Fe–Cu deposits were previously shown to exhibit a nodular, i.e. inherently rough morphology [20]. The added porous structure serves to further increase roughness and, therefore, the hydrophobic behavior of the coatings. Two distinct compositions

and three sub-micron pore diameters were chosen in order to study the effects on water and oil contact angle (CA). High water CAs were achieved overall with one configuration exhibiting superhydrophobicity with an average water CA of  $155.1^\circ$  and a contact angle hysteresis (CAH) of  $6.7^\circ$ . The oleophilic behavior was also investigated revealing very low oil CA. Water–oil separation ability and reusability of the samples over multiple trials was demonstrated as a proof of concept (Fig. 1c). Additionally, the small pore diameters are advantageous with respect to their potential toward separating both water–oil mixtures as well as emulsions while circumventing the fouling issues associated with membranes [21]. The entire fabrication process is upscalable and easy to implement in an industrial setting. Finally, the ferromagnetic properties of the Fe-rich Fe–Cu coatings [20] underscore the potential for magnetic manipulation and recyclability.

## 2. Materials and methods

### 2.1. Instrumentation

Electrophoretic deposition was implemented using a Keysight B2902A Precision Source/Measure Unit as a voltage source and a custom 3D-printed cell. The cell consisted of a  $1\ \text{cm} \times 1\ \text{cm} \times 0.6\ \text{cm}$  poly(methyl methacrylate) (PMMA) chamber glued to a platinumized titanium sheet which served as a counter electrode. The substrate was fixed in place at a 0.5 cm distance from the counter electrode via indented slots at the back of the chamber. Electrodeposition was carried out using a three-electrode cell connected to a Metrohm/Eco Chemie Autolab PGSTAT302N potentiostat/galvanostat. A Pt wire counter electrode and a double junction Ag/AgCl ( $E = +0.210\ \text{V/SHE}$ ) reference electrode (Metrohm AG) with a 3 M KCl inner solution and a 1 M  $\text{Na}_2\text{SO}_4$  outer solution were used. Silicon/silicon dioxide (Si/SiO<sub>2</sub>) substrates with a 10 nm Ti adhesion layer and a 90 nm Au seed layer and cut into  $1 \times 1.5\ \text{cm}$  dimensions were used. The working area was measured to be  $1 \pm 0.1\ \text{cm}^2$ .

### 2.2. Colloidal suspension, electrolyte composition and working temperature

Monodisperse polystyrene (PS) sub-micron spheres in an 2.5% w/v solids aqueous suspension were purchased in three chosen dimensions (0.2, 0.35 and  $0.5\ \mu\text{m}$ ) from Polysciences, Inc. to serve as templates. To prepare the solution for electrophoretic deposition, 0.05 mL of the PS sphere suspension was mixed in 0.45 mL of ethanol (0.25% w/v PS spheres in final solution). The electrolytes (100 mL) were prepared with Millipore Milli-Q water and ACS Reagent grade chemicals purchased from Sigma-Aldrich. The first solution contained  $58.8\ \text{g L}^{-1}$   $(\text{NH}_4)_2\text{Fe}(\text{SO}_4)_2 \cdot 6\text{H}_2\text{O}$ ,  $1.25\ \text{g L}^{-1}$   $\text{CuSO}_4 \cdot 5\text{H}_2\text{O}$ ,  $7.9\ \text{g L}^{-1}$  glycine as a complexing agent,  $0.2\ \text{g L}^{-1}$  sodium dodecyl sulfate as a wetting agent and  $0.46\ \text{g L}^{-1}$  saccharine as a grain refining agent. The pH was adjusted from 3.7 to 2.2 with addition of  $\text{H}_2\text{SO}_4$  and samples were deposited at a temperature of  $25^\circ\text{C}$  (bath A). For the second solution, glycine was substituted with  $22.9\ \text{g L}^{-1}$  of sodium gluconate as the complexing agent and

samples were deposited from the as prepared solution with a pH of 4.1 at a temperature of 35 °C (bath B). The optimal electrolyte compositions and plating conditions were established in previous work [20].

### 2.3. Substrate preparation and fabrication procedure

The substrates were initially cleaned with acetone, followed by isopropanol and, finally, rinsed with Milli-Q water to remove any debris and residues. As preparation for electrophoretic deposition they were treated with a 10 mM solution of 3-mercaptopropylsulfonic acid sodium salt (MPS, 90% purity from Sigma-Aldrich) in ethanol pre-heated to 50 °C for 1 h to increase the gold-coated substrate wettability [19]. Finally, they were alternatively rinsed in Milli-Q water and ethanol to remove excessive MPS layers. After placing the substrate in the cell, the PS sphere solution was added, covering a 1 cm<sup>2</sup> area [19]. A constant potential of 40 V cm<sup>-1</sup> in the case of the two smaller sphere sizes and of 60 V cm<sup>-1</sup> for the largest spheres was applied with deposition times of 1 min and 5 min, respectively [19]. Deposition time was tuned to allow for multi-layer assembly while preserving quality with regard to stability and number of defects. Following electrophoretic deposition, the samples were promptly placed on a hot plate and heated at 50 °C for 15 min [19]. Prior to performing electrodeposition, the Fe–Cu electrolyte was de-aerated with argon gas. Mild stirring during deposition was applied by means of a magnetic stirring bar ( $\omega=200$  rpm). The galvanostatic mode was chosen with applied current densities of  $-10$  mA cm<sup>-2</sup> (bath A) and  $-25$  mA cm<sup>-2</sup> (bath B) and deposition times between 3 and 5 min (bath A) and 15 and 50 s (bath B) depending on desired thickness, namely targeting single or multi-layer coverage of the previously deposited spheres. Finally, the PS spheres were removed by immersing the samples in chloroform for 3 h followed by a final rinsing in acetone, ethanol and MQ-water.

### 2.4. Characterization

Sample morphology and roughness were observed using a Zeiss MERLIN Field Emission Scanning Electron Microscope (FE-SEM) and a MultiMode MMAFM-2 Atomic Force Microscope from Digital Instruments, Inc. The elemental composition was determined by Energy Dispersive X-ray Spectroscopy (EDXS) at an acceleration voltage of 15 kV. A Perkin Elmer Optima 4300DV Inductively Coupled Plasma Optical Emission Spectrometer (ICP-OES) was used to measure the mass of deposited Fe and Cu of two samples as part of an investigation into determining the potential loss of material when the samples are immersed in an aqueous environment. In preparation, two samples were placed separately in beakers containing tap water for a duration of 120 h then mildly rinsed with solvents, dried and dissolved in test tubes each containing 2 mL of nitric acid solution. One tube was filled solely with 2 mL nitric acid solution to be used as a reference and another with tap water reference. Finally, two test tubes were filled with 2 mL each of the tap water from the beakers where the samples were previously placed. The crystallographic structure of the deposits was studied by Grazing Incidence X-ray Diffraction (GIXRD) using CuK $\alpha$  radiation and a Bragg-Brentano  $\theta$ - $2\theta$  configuration with a grazing incidence angle of 1°. For further elemental analysis of the surface with a particular focus on the at.% of oxygen incorporated, X-ray Photoelectron Spectroscopy (XPS) analysis of several samples was carried out on a PHI 5500 Multitechnique System spectrometer from Physical Electronics, equipped with a monochromatic X-ray source placed perpendicular to the analyzer axis and calibrated using the 3d5/2 line of Ag. A contact angle analyzer (SmartDrop, Femtofab) was used to determine the water and oil contact angles at room temperature. The liquids used for the measurements were 3  $\mu$ L droplets of

ultrapure water and of motor oil, respectively. The reported values correspond to the average of three independent measurements at different sample locations.

### 2.5. Oil/water separation capability

The oil absorption capacity was assessed using gas chromatography–mass spectrometry (GC–MS) using commercially available motor oil (diesel mixture) and the analysis was based on the signal corresponding to diesel. Several droplets of oil with a volume ranging between 21 and 27  $\mu$ L were placed with a micropipette in a beaker containing MQ water and a sample was manipulated using tweezers in order to approach the oil droplets where it could absorb and remove them from the water. The sample was then rinsed and placed in a vial containing 5 mL of an internal standard (IS) solution, namely palmitic acid in hexane, immediately after the final iteration and the process was repeated for a second replica. The experiment was then reiterated for 5 cycles of removal for 2 new replicas which were sonicated for 5 min in hexane and left to dry after each oil collection apart from the last round where they were placed in the vial with the IS solution. Finally, the same was done for 2 more replicas for a total of 10 cycles. All samples were then sonicated for 5 min to ensure complete oil separation from the samples and homogenization in the IS solution. To ensure that the samples were cleaned properly between iterations, 2 of the replicas were removed from the vials after sonication and placed in fresh vials with the IS solution and were once more sonicated for a 5 min duration.

## 3. Results and discussion

### 3.1. Fabrication and characterization of porous films

The fabrication of the Fe–Cu porous films was conducted in two main steps. Firstly, the polystyrene (PS) sub-micron spheres were assembled onto the Au coated substrate in a close-packed structure via electrophoretic deposition based on the procedure established by Pokki et al. [22]. A scanning electron microscopy (SEM) micrograph of the self-assembled PS sphere layers can be seen in Fig. 2. In the second step, based on our previous work [20] on the study and characterization of Fe–Cu continuous films, optimized electrolytes and plating conditions were chosen to deposit the Fe-rich and Cu-rich coatings in the interstices between the spheres. Upon removal of the spheres in the final step, the porous network was revealed with the pore sizes directly corresponding to the sphere diameters. This can be observed in the SEM micrographs in Fig. 3a and b of the Cu-rich and Fe-rich films obtained, where plating time was



Fig. 2. PS spheres of 200 nm diameter assembled onto Au substrate via electrophoretic deposition.



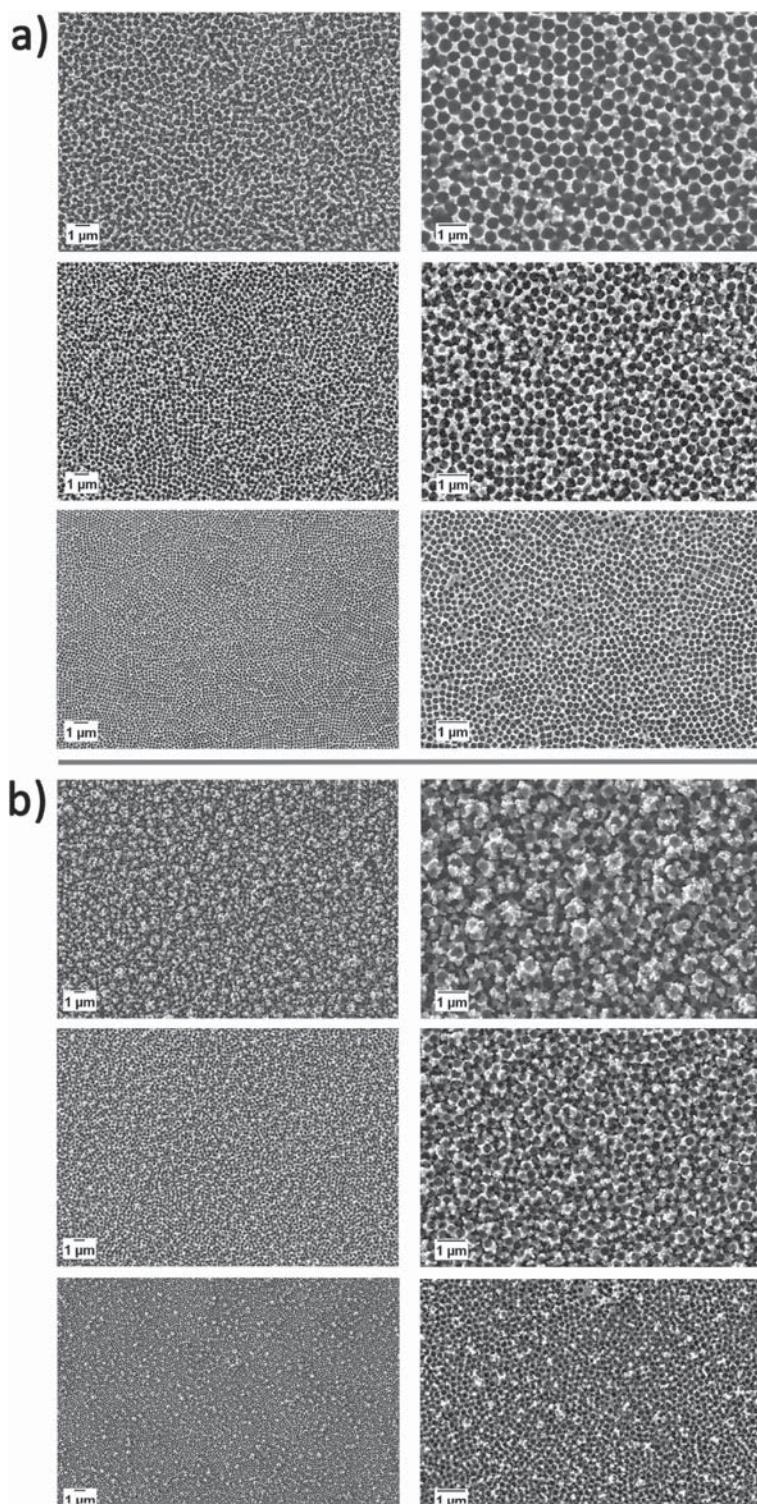


**Fig. 3.** Cu-rich porous films after removal of PS spheres of different diameters: (a)  $\text{Fe}_3\text{Cu}_{97}$  porous films of 500 nm (top), 350 nm (middle) and 200 nm (bottom) pore diameters and (b)  $\text{Fe}_{85}\text{Cu}_{15}$  porous films of 500 nm (top) and 350 nm (middle) pore diameters and  $\text{Fe}_{75}\text{Cu}_{25}$  film of 200 nm pore size (bottom).

**Table 1**

Atomic percentage of Fe, Cu and O at the uttermost film surface as determined via XPS. Notice that the correspondence between XPS (surface) and EDX (bulky) analyses is: 'Cu-rich' sample corresponds to 'Fe<sub>3</sub>Cu<sub>97</sub>' for the three pore sizes; 'Fe-rich' sample corresponds to 'Fe<sub>85</sub>Cu<sub>15</sub>' for the 500 nm and 350 nm pore size, and to the 'Fe<sub>75</sub>Cu<sub>25</sub>' for the 200 nm pore size.

	At.% at surface											
	Continuous			500 nm			350 nm			200 nm		
	Fe	Cu	O	Fe	Cu	O	Fe	Cu	O	Fe	Cu	O
Cu-rich	11.76	25.58	62.66	15.18	24.78	60.04	15.24	22.24	62.52	17.99	20.67	61.34
Fe-rich	25.64	10.89	63.46	16.12	16.98	66.91	14.57	12.17	73.26	15.89	14.94	69.17

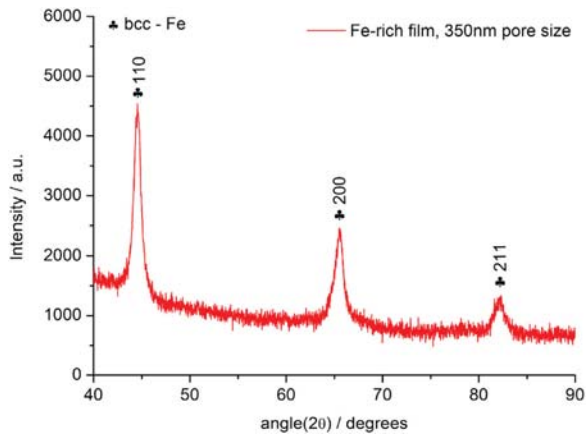


Fig. 4. XRD diffractogram obtained from a Fe<sub>85</sub>Cu<sub>15</sub> macroporous film.

calculated to cover multiple layers of spheres, thus resulting in a porous structure of two or more layers. Also, the pores are not randomly distributed but the occurrence of ordered or pseudo-ordered domains of  $\sim 1 \mu\text{m}^2$  in size is apparent for some of the films.

Since wettability is a surface phenomenon, it was deemed necessary to further investigate the surface elemental composition of the films obtained. In Table 1, the at.% of Fe, Cu and O for all deposits, determined by X-ray photoelectron spectroscopy (XPS), are listed. It can be easily seen that the at.% of oxygen is consistently higher than 60 at.% indicating the presence of mainly Fe and Cu oxides at the surface which comes into contact with the water and oil droplets. Beneath this nanometer-thick passivation layer, the films are entirely metallic.

Finally, for phase identification purposes, XRD analysis was performed on a number of Fe-rich samples. A representative diffractogram of a 350 nm pore size sample is shown in Fig. 4. The Miller indices have also been included. Remarkably, in contrast to the Fe-rich continuous films with similar composition and a thickness of several microns which were found to be phase separated

**Table 2**

Average water contact angles of Cu-rich and Fe-rich continuous and patterned films.

Composition	Water contact angle			
	Continuous	500 nm	350 nm	200 nm
Cu-rich	109.0°	136.2°	134.9°	146.0°
Fe-rich	135.8°	155.1°	145.2°	145.2°

[20], the macroporous Fe<sub>85</sub>Cu<sub>15</sub> films are shown to be single phase. This can be explained by the confined growth of the material at the sub-micron interstices between the PS spheres. It has been also observed for other systems like Cu–Ni that when the void size is sufficiently small, phase separation can be eventually suppressed [23]. Naturally, the oxide layer of a few nanometers found at the surface does not influence the XRD results as it is negligible compared to the overall interaction volume. The Cu-rich films were expectedly single phase as the amount of Fe (3 at.%) is well below the solubility limit of the face-centered cubic (fcc)-Cu phase.

### 3.2. Water wettability assessment

The wetting behavior of the samples was assessed using the sessile drop method to determine the static CA. In general, all samples were found to be hydrophobic with CAs exceeding 134° for the Cu-rich and 145° for the Fe-rich porous coatings. In comparison, the Cu-rich and Fe-rich continuous films of similar composition electrodeposited under the same conditions as their porous counterparts had significantly lower water CA. Their morphology can be observed in the SEM micrographs in Fig. 5.

In Table 2, the average value of the water CA for each sample can be viewed. Higher Fe content in the macroporous films was typically associated with an increase of roughness seen by the nano-size features along the pore walls and this is likely the reason for the enhanced hydrophobicity. Indeed, this is in agreement with previous studies showing that with an increase of roughness and even more so in the case of introducing hierarchical roughness, the hydrophobicity of the material is augmented [24–28]. Notably, the Fe-rich samples of 500 nm pore size were found to exhibit superhydrophobic behavior, as seen in Fig. 6a, with water CAs consistently

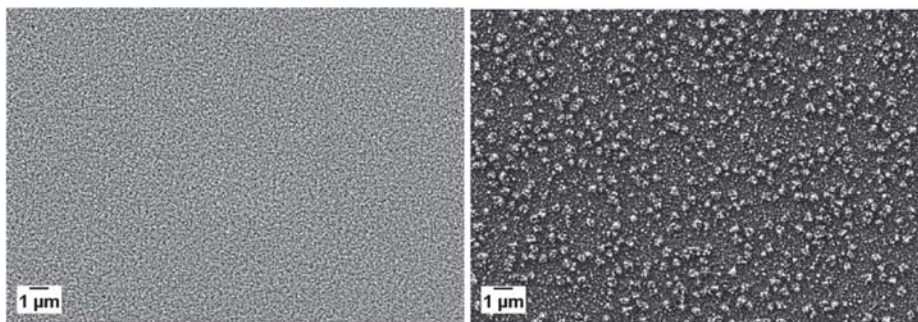
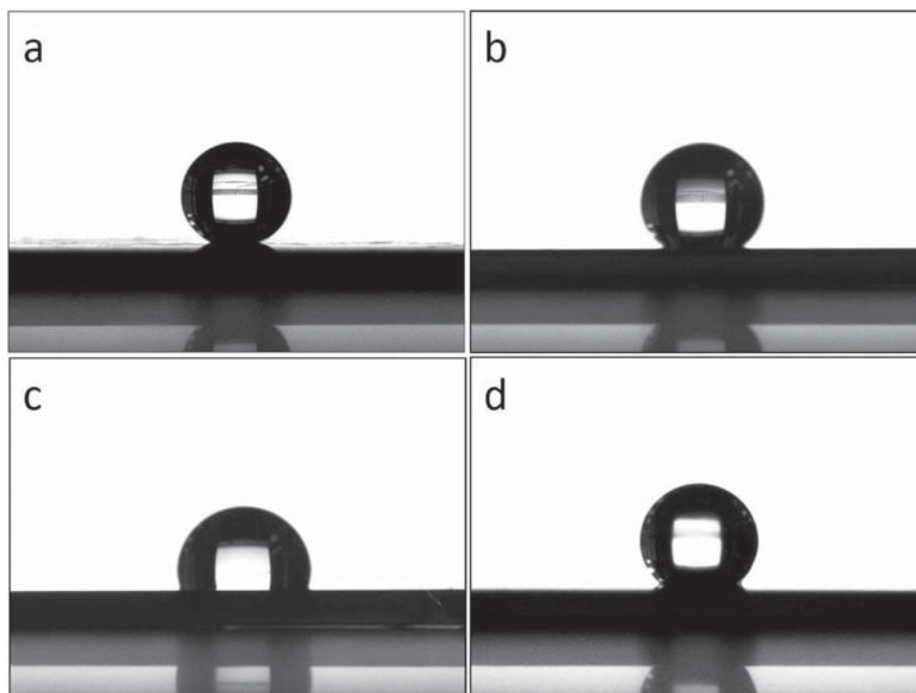


Fig. 5. SEM images of Fe<sub>3</sub>Cu<sub>97</sub> (left) and Fe<sub>85</sub>Cu<sub>15</sub> (right) continuous film morphology.



**Fig. 6.** Image taken during drop placement on the surface of: (a) an Fe-rich superhydrophobic sample with 500 nm pores, (b) an Fe-rich hydrophobic sample with 350 nm pores, (c) a Cu-rich continuous hydrophobic sample, and (d) a Cu-rich hydrophobic sample with 200 nm pores.

above  $150^\circ$  for all measurements. Importantly, the advancing and receding angles for the superhydrophobic sample were also measured and the calculated CAH of approximately  $6.7^\circ$  indicates a non-stick surface. Therefore, for the 500 nm sample, transition to the Cassie–Baxter state [29,30], with air pocket formation underneath the droplet, is quite evident. Curiously, the CAH value of the Fe-rich sample of 350 nm pore diameter, seen in Fig. 6b, was measured at a markedly higher value of  $19.5^\circ$ . For the latter case, it can be seen that there is at least partial wetting along the contact line. On the other hand, the hysteresis value for the continuous films was  $10.7^\circ$  for the Fe-rich and  $17.3^\circ$  for the Cu-rich, respectively (see Fig. S1a for the CA image of the continuous Fe-rich film). The Cu-rich continuous film is in a state closer to Wenzel as depicted in Fig. 6c [31,32]. It is also worth mentioning that, in comparison, the most hydrophobic Cu-rich sample was that of 200 nm pore size with a relatively high average CA of  $146^\circ$  and a CAH of  $16.6^\circ$ . Nevertheless, the droplet appears pinned on the surface, as depicted in Fig. 6d, indicating the presence of an intermediate state between the regimes of Wenzel and Cassie–Baxter with strong surface adhesion [33].

At this point, it was essential to further study the topography and estimate the roughness of the Fe-rich macroporous samples that displayed higher CAs overall and to compare them to the continuous case. With this consideration, atomic force microscopy (AFM) images were acquired for selected samples as seen in Fig. 7. It can be seen that the porous morphology is quite well defined in the images. Moreover, the corresponding root mean square (RMS) values of the height irregularities from an area of  $5\ \mu\text{m} \times 5\ \mu\text{m}$  were calculated at approximately 221.0 nm for the 500 nm pore sample, 140.5 nm for the 350 nm pore sample and 49.2 nm for the continuous film. This finding further supports the connection between increased roughness and higher CA. Finally, it is worth mentioning that the hydrophobic/superhydrophobic properties of the coatings are achieved without any post-surface functionalization of the

electrodeposited layers, in contrast with other works dealing with porous Fe-based alloy [34] or Cu films [35]. Even functionalized electrodeposited magnetite ( $\text{Fe}_3\text{O}_4$ ) films exhibit much lower CA values [36].

### 3.3. Oleophilicity and oil droplet collection performance

Oil wettability was investigated for all samples using commercial car diesel oil as a model. A very oleophilic behavior with initial CAs between  $13.0^\circ$  and  $18.9^\circ$  and gradually decreasing was observed (see video V1 in the Supporting Information corresponding to a Cu-rich film of 200 nm pore diameter). A notable exception was the initial oil CA for Cu continuous films which was recorded at approximately  $24.6^\circ$ . The Fe continuous films also demonstrated the third highest oil CA of  $18.8^\circ$  which was very similar to that of the Cu-rich patterned films of 200 nm pore size measured at  $18.9^\circ$  (representative images of different samples during oil droplet placement are shown in Fig. S1b–d of the Supporting Information).

Next, the water/oil separation ability was assessed as a proof of concept using Fe-rich superhydrophobic samples due to their superior water repellent properties which would also allow for higher oil absorption. The samples were shown to have removed approximately 62% of the total oil added on average, as determined by gas chromatography–mass spectrometry analyses (see Section 2). Some losses were inevitably caused by the apparent tendency of the oil to adhere on the glass beaker which was used to hold the water/oil mixture and specifically along the contact line with the surface of the water. After 5 cycles of oil removal, a 45% of oil absorption was attained. Lastly, post 10 cycles the absorption seemed to hold at about 42%. Still images of a video recorded during a collection process can be seen in Fig. 8 (see video V2 in the Supporting Information). In this case, the oil was mixed with graphite powder for improved contrast in the recording. Finally, the chemical stability of the films was tested by immersing them in tap water for 120 h

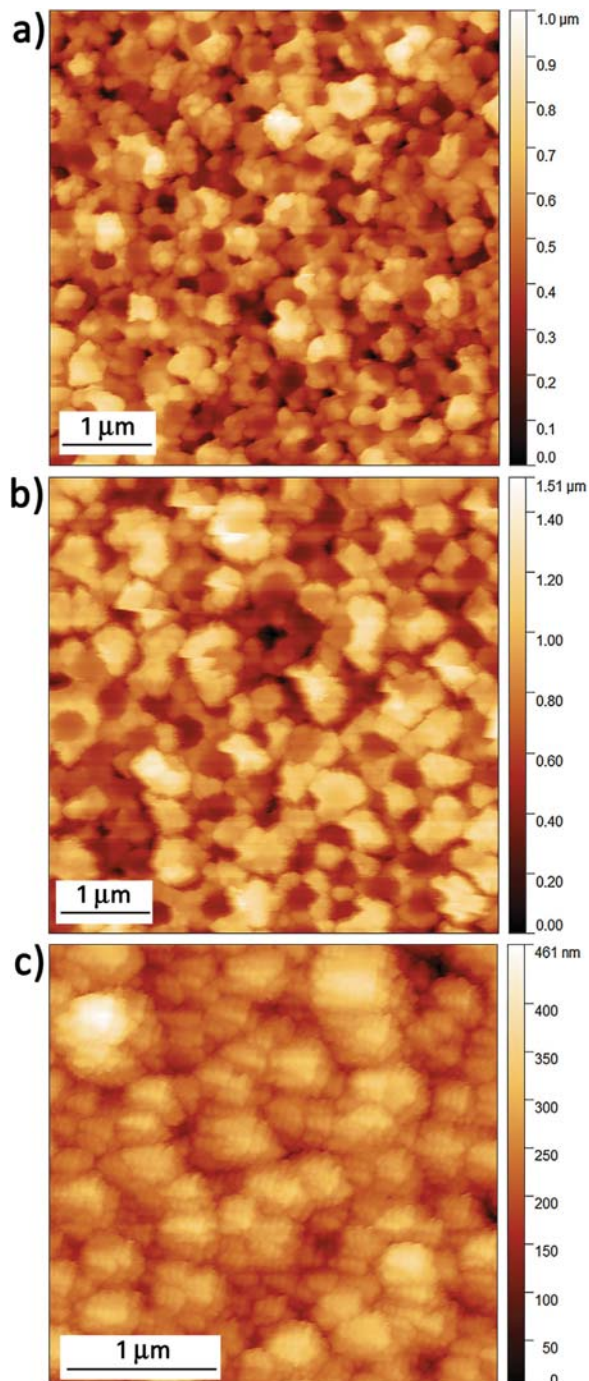


**Fig. 7.** AFM images of a  $\text{Fe}_{85}\text{Cu}_{15}$  macroporous film of (a) 350 nm and (b) 500 nm pore size, and of (c) a continuous film of the same composition.

and using inductively coupled plasma optical emission spectrometry (ICP-OES) measurements to detect any material losses due to eventual corrosion. The result of these tests indicated that there was no Fe or Cu amount dissolved in the water after the 120-h period when compared to the reference sample as can be verified in [Table T1 of the Supporting Information](#).

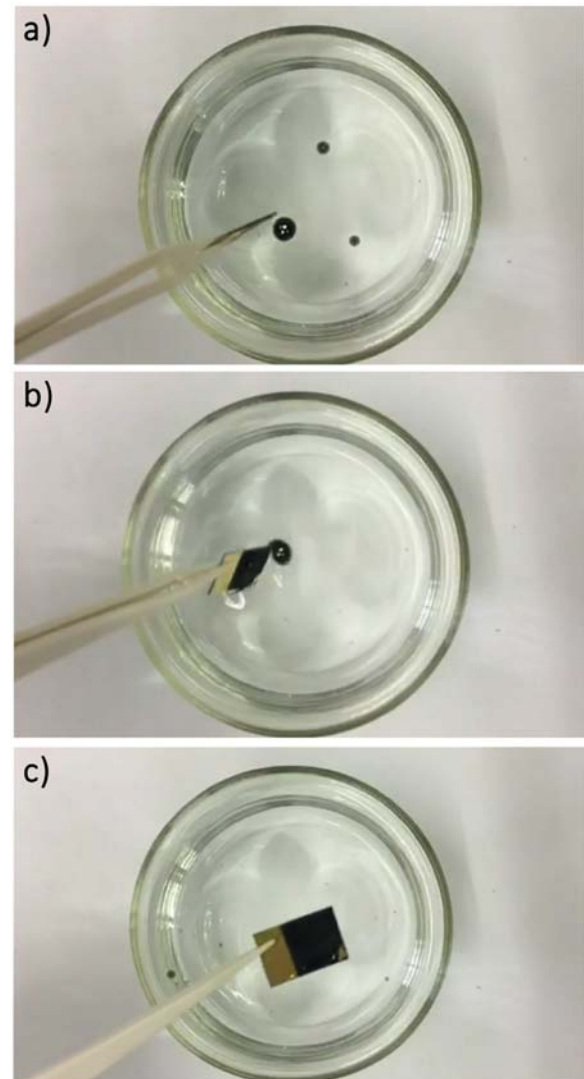


**Fig. 8.** From (a) to (c) still images taken from a recording of the oil droplet removal process.

#### 4. Conclusion

Porous Fe–Cu coatings of Fe-rich (75–85 at.% Fe) and Cu-rich (3 at.% Fe) compositions and tunable pore size were prepared through a simple technique of combining electrodeposition and colloidal lithography.

Water/oil wettability measurements demonstrated the strongly hydrophobic/oleophilic nature of the deposits which was enhanced by the hierarchical roughness resulting from the patterned microstructure. Superhydrophobicity with a CA hysteresis of  $6.7^\circ$  was achieved for one configuration. Fe-rich deposits typically exhibited higher CAs than their Cu-rich counterparts, with one prominent exception, though this was also accompanied by a higher roughness observed in the pore walls of the former. This indicates that surface morphology may play a more significant role in the wetting characteristics of the coatings than elemental composition. Finally, an oil absorption capacity exceeding 60% on the

first trial which is maintained at more than 40% after multiple removal cycles was documented.

#### Data availability statement

The raw/processed data required to reproduce these findings cannot be shared at this time due to technical or time limitations.

#### Conflict of interest

All authors confirm that there is no conflict of interest.

#### Acknowledgements

This work was supported by the SELECTA (No. 642642) H2020-MSCA-ITN-2014 project. Partial financial support by the Spanish Government [Project MAT2017-86357-C3-1-R and associated FEDER], the Generalitat de Catalunya (2017-SGR-292) and the European Research Council (SPIN-PORICS 2014-Consolidator Grant, Agreement n° 648454) is acknowledged. E.P. is grateful to MINECO for the “Ramon y Cajal” contract (RYC-2012-10839). J.P. acknowledges the contributions of Y. Çelik in the preparation of the 3D-printed setup for electrophoretic deposition, and P. Petit in 3D rendering of illustrations on porous films’ fabrication. Authors acknowledge A. Eustaquio and O. Palacios from the Servei d’Anàlisi Química de Universitat Autònoma de Barcelona for the fruitful discussions on GC measurements and networking support by the Cost Action MP1407.

#### Appendix A. Supplementary data

Supplementary data associated with this article can be found, in the online version, at [doi:10.1016/j.apmt.2018.03.007](https://doi.org/10.1016/j.apmt.2018.03.007).

#### References

- [1] B. Bhushan, Y.C. Jung, *Prog. Mater. Sci.* 56 (2011) 1.
- [2] W. Barthlott, C. Neinhuis, *Planta* 202 (1997) 1.
- [3] M. Qinglang, H. Cheng, A.G. Fane, R. Wang, H. Zhang, *Small* 12 (2016) 2186.
- [4] B. Wang, W. Liang, Z. Guo, W. Liu, *Chem. Soc. Rev.* 44 (2015) 336.
- [5] M. Ge, C. Cao, J. Huang, X. Zhang, Y. Tang, X. Zhou, K. Zhang, Z. Chen, Y. Lai, *Nanoscale Horiz.* (2018), <http://dx.doi.org/10.1039/C7NH00185A>, Advance online publication.
- [6] D.A.E.G. Dave, A.E. Ghaly, *Am. J. Environ. Sci.* 7 (2011) 423.
- [7] M. Fingas, *The Basics of Oil Spill Cleanup*, CRC Press, Boca Raton, FL, USA, 2012.
- [8] S. Kleindienst, J.H. Paul, S.B. Joye, *Nat. Rev. Microbiol.* 13 (2015) 388.
- [9] J. Fritt-Rasmussen, S. Wegeberg, K. Gustavson, *Water Air Soil Pollut.* 226 (2015) 329.
- [10] W. Zhang, Z. Shi, F. Zhang, X. Liu, J. Jin, L. Jiang, *Adv. Mater.* 25 (2013) 2071.
- [11] J. Zhang, M.D. Baró, E. Pellicer, *J. Sort, Nanoscale* 6 (2014) 12490.
- [12] T.W. Ebbesen, H.J. Lezec, H.F. Ghaemi, T. Thio, P.A. Wolff, *Nature* 391 (1998) 667.
- [13] O.D. Velev, E.W. Kaler, *Adv. Mater.* 12 (2000) 531.
- [14] P. Jiang, J.F. Bertone, K.S. Hwang, V.L. Colvin, *Chem. Mater.* 11 (1999) 2132.
- [15] P. Jiang, T. Prasad, M.J. McFarland, V.L. Colvin, *Appl. Phys. Lett.* 89 (2006) 011908.
- [16] Z.Z. Gu, A. Fujishima, O. Sato, *Chem. Mater.* 14 (2002) 760.
- [17] Y. Yin, Y. Lu, B. Gates, Y. Xia, *J. Am. Chem. Soc.* 123 (2001) 8718.
- [18] J.P. Hoogenboom, C. Retif, E. De Bres, M. Van De Boer, A.K. van Langen-Suurling, J. Romijn, A. Van Blaaderen, *Nano Lett.* 4 (2004) 205.
- [19] A.L. Rogach, N.A. Kotov, D.S. Koktysh, J.W. Ostrander, G.A. Ragoisha, *Chem. Mater.* 12 (2000) 2721.
- [20] E. Dislaki, J. Sort, E. Pellicer, *Electrochim. Acta* 231 (2017) 739.
- [21] Y. Peng, Z. Guo, *J. Mater. Chem. A* 4 (2016) 15749.
- [22] J. Pokki, O. Ergeneman, K.M. Sivaraman, B. Özkale, M.A. Zeeshan, T. Lühmann, B.J. Nelson, S. Pane, *Nanoscale* 4 (2012) 3083.
- [23] Z. Liu, G. Xia, F. Zhu, S. Kim, N. Markovic, C.L. Chien, P.C. Searson, *J. Appl. Phys.* 103 (2008) 064313.
- [24] M. Miwa, A. Nakajima, A. Fujishima, K. Hashimoto, T. Watanabe, *Langmuir* 16 (2000) 5754.
- [25] L. Feng, S. Li, Y. Li, H. Li, L. Zhang, J. Zhai, Y. Song, B. Liu, L. Jiang, D. Zhu, *Adv. Mater.* 14 (2002) 1857.
- [26] Z. Yoshimitsu, A. Nakajima, T. Watanabe, K. Hashimoto, *Langmuir* 18 (2002) 5818.
- [27] D. Quéré, *Physica A Stat. Mech. Appl.* 313 (2002) 32.
- [28] N.A. Patankar, *Langmuir* 20 (2004) 8209.
- [29] A.B.D. Cassie, *J. Chem. Soc. Faraday Trans.* 40 (1944) 546.
- [30] S. Wang, L. Jiang, *Adv. Mater.* 19 (2007) 3423.
- [31] R.N. Wenzel, *Ind. Eng. Chem.* 28 (1936) 988.
- [32] D. Murakami, H. Jinnai, A. Takahara, *Langmuir* 30 (2014) 2061.
- [33] C.R. Szczepanski, F. Guittard, T. Darmanin, *Adv. Colloid Interface Sci.* 241 (2017) 37.
- [34] S. Wang, Y.H. Ling, J. Zhang, J.J. Wang, G.Y. Xu, *Int. J. Min. Metal. Mater.* 21 (2014) 395.
- [35] Y. Li, W.Z. Jia, Y.Y. Song, Y.H. Xia, *Chem. Mater.* 19 (2007) 5858.
- [36] M. Cortés, E. Gómez, J. Sadler, E. Vallés, *Electrochim. Acta* 56 (2011) 4087.

# **Supporting Information**

**Fabrication of sustainable hydrophobic and oleophilic pseudo-ordered macroporous Fe–Cu films with tunable composition and pore size via electrodeposition through colloidal templates**

*Evangelia Dislaki,<sup>1,\*</sup> Juho Pokki<sup>2</sup>, Salvador Pané<sup>2</sup>, Jordi Sort<sup>1,3</sup>, Eva Pellicer<sup>1,\*</sup>*

<sup>1</sup>Departament de Física, Universitat Autònoma de Barcelona, 08193 Bellaterra, Spain

<sup>2</sup>Institute of Robotics and Intelligent Systems, ETH Zurich, CH-8092, Zurich, Switzerland

<sup>3</sup>Institució Catalana de Recerca i Estudis Avançats (ICREA), Passeig Lluís Companys 23, 08010 Barcelona, Spain

E-mails: [evangelia.dislaki@uab.cat](mailto:evangelia.dislaki@uab.cat)

[eva.pellicer@uab.cat](mailto:eva.pellicer@uab.cat)

Keywords: electrodeposition; porous films; colloidal lithography; wettability; sustainability

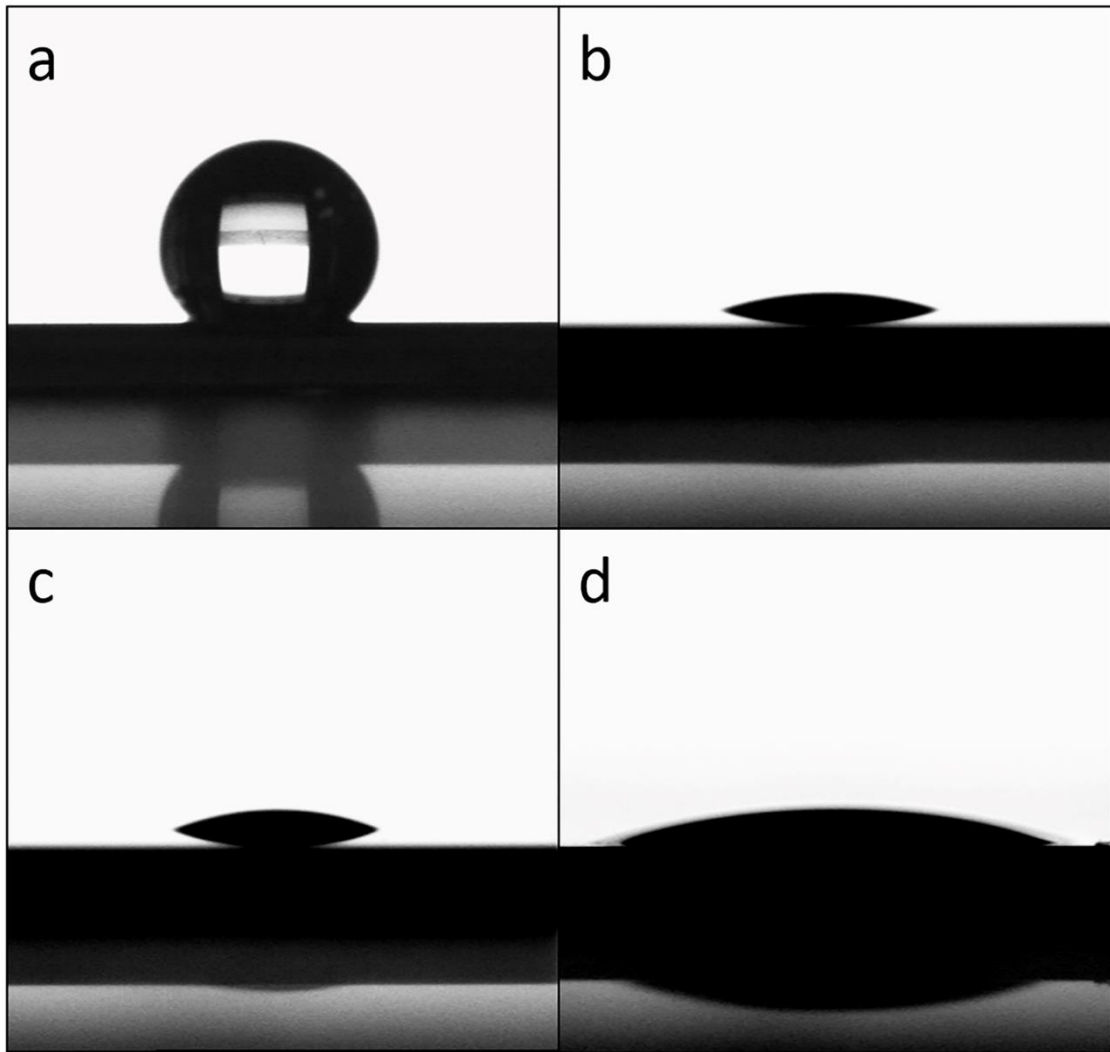


**Figure S1.** Image taken during water drop placement on the surface of: a) an Fe-rich continuous hydrophobic sample and during oil drop placement on the surface of: b) an Fe-rich continuous oleophilic sample, c) a Cu-rich continuous oleophilic sample, and d) an Fe-rich oleophilic sample with 500 nm pores.

**Table T1.** Mass Concentration of Fe and Cu in the specified liquid media as measured by ICP-OES.

Sample Measured	Mass Concentration	
	Fe (mg/L)	Cu (mg/L)
Water blank	<0.1	0.62
Nitric acid solution blank	<0.1	<0.1
Water where sample A was placed	<0.1	0.31
Nitric acid solution containing dissolved sample A	2.0	23
Water where sample B was placed	<0.1	0.34
Nitric acid solution containing dissolved sample B	2.4	23





### **3.3. Coercivity modulation in Fe–Cu pseudo-ordered porous thin films controlled by an applied voltage: a sustainable, energy-efficient approach to magneto-electrically driven materials**

The control of magnetism through voltage application has garnered much research interest due to the vast array of prospective applications such as in magnetic storage devices and spintronics. More specifically, the modulation of coercivity ( $H_c$ ) using electric fields is an appealing way towards minimizing power dissipation during magnetic actuation. In order to switch magnetization, a magnetic field larger than the  $H_c$  needs to be applied. Such magnetic fields are generated using electric currents which cause power dissipation through Joule heating. The utilization of DC voltages (with no associated flowing currents as, for example, in a condenser) in order to reduce the  $H_c$  can dramatically augment the energy efficiency of magnetically driven devices. Unfortunately, in metallic alloys, electric fields are dampened due to the confinement of charges at the very outer surface of the alloy, a phenomenon known as the electric-field screening effect. For this reason, voltage-driven modulation of coercivity was initially only observed in ultra-thin magnetic alloys and the maximum reduction of coercivity was only 4.5%. Observation of this effect in thicker films was recently achieved in our laboratory in nanoporous CuNi alloys produced by micelle-assisted electrodeposition, a complex and sensitive method. In this case, the nanoporosity of the material allowed to overcome the ultra-thin film requirement.

In this direction, hierarchically porous Fe–Cu films were fabricated by a two-step approach combining electroplating with colloidal lithography. Patterned pores in the range of 200 nm to 500 nm were created by simply varying the diameter of the colloidal templates. Ionic liquid gating was used to substantially boost the electric field through the formation of the electrical double layer. The dual porosity of up to 65% achieved by the patterned, pseudo-ordered macro-pores coupled with the inherent nanoporosity of the material along the ultrathin pore walls, resulted in a high surface-to-volume ratio and enabled a 25% voltage-driven coercivity reduction and good cyclability despite a film thickness of hundreds of nanometers.

X-ray photoemission spectroscopy and grazing incidence diffraction revealed no changes to the iron species while there was partial oxidation/reduction of the Cu species upon application of positive/negative bias, respectively. Careful analysis revealed that the observed magnetoelectric effects cannot be ascribed to redox reactions but are rather mainly attributed to carrier accumulation and dissipation.



**Coercivity modulation in Fe–Cu pseudo-ordered porous thin films controlled by an applied voltage: a sustainable, energy-efficient approach to magneto-electrically driven materials**

Evangelia Dislaki,\* Shauna Robbennolt, Mariano Campoy-Quiles, Josep Nogués, Eva Pellicer, and Jordi Sort\*

Evangelia Dislaki, Dr. Shauna Robbennolt, Dr. Eva Pellicer

Departament de Física, Universitat Autònoma de Barcelona (UAB), E-08193 Bellaterra, Spain.

E-mail: [evangelia.dislaki@uab.cat](mailto:evangelia.dislaki@uab.cat)

Dr. Mariano Campoy-Quiles

Institut de Ciència de Materials de Barcelona (ICMAB-CSIC), Campus UAB, E-08193 Bellaterra, Spain.

Prof. Dr. Josep Nogués

Catalan Institute of Nanoscience and Nanotechnology (ICN2), CSIC and The Barcelona Institute of Science and Technology, Campus UAB, E-08193 Bellaterra, Spain.

Institució Catalana de Recerca i Estudis Avançats (ICREA), Passeig Lluís Companys 23, E-08010 Barcelona, Spain.

Prof. Dr. Jordi Sort

Departament de Física, Universitat Autònoma de Barcelona (UAB), E-08193 Bellaterra, Spain.

Institució Catalana de Recerca i Estudis Avançats (ICREA), Passeig Lluís Companys 23, E-08010 Barcelona, Spain.

E-mail: [jordi.sort@uab.cat](mailto:jordi.sort@uab.cat)



# Coercivity Modulation in Fe–Cu Pseudo-Ordered Porous Thin Films Controlled by an Applied Voltage: A Sustainable, Energy-Efficient Approach to Magnetolectrically Driven Materials

*Evangelia Dislaki,\* Shauna Robbenolt, Mariano Campoy-Quiles, Josep Nogués, Eva Pellicer, and Jordi Sort\**

Fe–Cu films with pseudo-ordered, hierarchical porosity are prepared by a simple, two-step procedure that combines colloidal templating (using sub-micrometer-sized polystyrene spheres) with electrodeposition. The porosity degree of these films, estimated by ellipsometry measurements, is as high as 65%. The resulting magnetic properties can be controlled at room temperature using an applied electric field generated through an electric double layer in an anhydrous electrolyte. This material shows a remarkable 25% voltage-driven coercivity reduction upon application of negative voltages, with excellent reversibility when a positive voltage is applied, and a short recovery time. The pronounced reduction of coercivity is mainly ascribed to electrostatic charge accumulation at the surface of the porous alloy, which occurs over a large fraction of the electrodeposited material due to its high surface-area-to-volume ratio. The emergence of a hierarchical porosity is found to be crucial because it promotes the infiltration of the electrolyte into the structure of the film. The observed effects make this material a promising candidate to boost energy efficiency in magnetolectrically actuated devices.

screening length of metals, which was previously thought to be a limiting factor for the electric field effect,<sup>[2]</sup> the magnetic properties of ferromagnetic films, such as saturation magnetization, coercivity, magnetoresistance, and magnetic anisotropy have been successfully manipulated using electrical methods including voltage control.<sup>[3–12]</sup> In particular, the reduction of coercivity using electric fields is an appealing approach for minimizing power dissipation during magnetic actuation. More specifically, in order to switch the magnetization, a magnetic field larger than the coercivity needs to be externally applied. Electric currents are needed to generate such magnetic fields (or to switch magnetization by spin-torque effect). Since flowing electric currents are associated with Joule heating power dissipation, a reduction of the coercivity with DC voltages can drastically boost the energy


## 1. Introduction

The potential toward voltage manipulation of magnetism is currently a research topic of tremendous interest due to its numerous prospective applications in areas such as magnetic data storage or spin-based electronics.<sup>[1]</sup> Despite the short

efficiency in magnetically actuated devices. Voltage control of magnetism can be achieved through several mechanisms. These can be divided in five categories: (i) carrier accumulation, (ii) strain, (iii) exchange coupling, (iv) orbital reconstruction, and (v) electrochemical effect.<sup>[1]</sup> The possible coupling between different magnetolectric effects when the film thickness is in the

E. Dislaki, Dr. S. Robbenolt, Dr. E. Pellicer  
Departament de Física  
Universitat Autònoma de Barcelona (UAB)  
E-08193 Bellaterra, Spain  
E-mail: evangelia.dislaki@uab.cat

Dr. M. Campoy-Quiles  
Institut de Ciència de Materials de Barcelona (ICMAB-CSIC)  
Campus UAB, E-08193 Bellaterra, Spain

 The ORCID identification number(s) for the author(s) of this article can be found under <https://doi.org/10.1002/advs.201800499>.

© 2018 The Authors. Published by WILEY-VCH Verlag GmbH & Co. KGaA, Weinheim. This is an open access article under the terms of the Creative Commons Attribution License, which permits use, distribution and reproduction in any medium, provided the original work is properly cited.

DOI: 10.1002/advs.201800499

Prof. J. Nogués  
Catalan Institute of Nanoscience and Nanotechnology (ICN2)  
CSIC and the BIST  
Campus UAB, E-08193 Bellaterra, Spain

Prof. J. Nogués  
Institució Catalana de Recerca i Estudis Avançats (ICREA)  
Passeig Lluís Companys 23, E-08010 Barcelona, Spain

Prof. J. Sort  
Departament de Física  
Universitat Autònoma de Barcelona (UAB)  
E-08193 Bellaterra, Spain  
E-mail: jordi.sort@uab.cat

Prof. J. Sort  
Institució Catalana de Recerca i Estudis Avançats (ICREA)  
Passeig Lluís Companys 23, E-08010 Barcelona, Spain

range of several nanometers and the determination of the dominant factor are crucial issues requiring further investigation.<sup>[1]</sup>

In the case of ferromagnetic metals, carrier accumulation and relaxation is often driving the change in magnetism.<sup>[13,14]</sup> In bulk metals, the strong screening effect prevents penetration of the electric field throughout the entire metal. However, in the case of ultrathin metallic films with a high surface-to-volume ratio, a large electric field can be used to control carrier density, and thus magnetism. The use of liquid electrolytes has been shown to promote a large electric field owing to the very small thickness of the electric double layer (EDL) (typically <1 nm), which enables adjustment of the magnetic properties to a considerable extent.<sup>[2]</sup> However, the need to use ultrathin magnetic layers is hampering the development of practical devices based on these effects. Previously, with respect to thicker films, this phenomenon had only been achieved when mediated by ion migration (magnetoionics)<sup>[11]</sup> or by producing nanoporous alloys through highly sensitive and complex means such as micelle-assisted electrodeposition in order to bypass the requirement of an ultrathin film.<sup>[3]</sup> For this reason, a high surface area obtained by porosity was deemed a critical factor in attaining the desired magnetoelectric effect in films with a thickness of hundreds of nanometers. Porous metallic materials have been prepared in literature through the use of hydrogen bubble dynamic template,<sup>[15,16]</sup> block copolymers,<sup>[17–19]</sup> surfactant micelles,<sup>[20]</sup> and hard templates.<sup>[21,22]</sup> Among these, colloidal templating is a particularly advantageous method since it entails a swift and straightforward approach which, in conjunction with the electrodeposition technique, allows for the creation of a multilayered 3D architecture with controllable pore size. Moreover, the close packing of the colloidal spheres is conducive to the development of exceptionally thin pore walls.

In this work, hierarchically porous thin Fe–Cu films have been prepared by electrodeposition through colloidal templates

onto metallized substrates. Three macropore sizes (in the 200–500 nm range) were achieved through the selection of distinct colloidal sphere diameters. The close packing of the spheres, which was achieved by electrophoretic deposition, enabled the formation of ultrathin pore walls, which were found to exhibit an additional inherent nanoporosity according to ellipsometry measurements, thereby rendering a truly hierarchically porous alloy structure. The macropores are dispersed forming ordered or pseudo-ordered areas of  $\approx 1 \mu\text{m}^2$ . Importantly, the dual porosity leads to a high surface-to-volume ratio, which combined with the ultrathin pore walls, yields an excellent material for carrier density modulation<sup>[2]</sup> despite an overall film thickness of hundreds of nanometers. In fact, reversible coercivity ( $H_c$ ) reduction in the range of 21.6–25.3% was observed in all cases. Morphological, chemical, and structural analyses were carried out to correlate the structure–morphology with the underlying mechanisms of the voltage control of magnetism.

## 2. Results and Discussion

### 2.1. Sample Morphology and Porosity Assessment

Schematic drawings of the colloidal templating process are given in **Figure 1a,b**. Representative field emission scanning electron microscope (FESEM) images of the porous Fe–Cu films obtained after removal of the polystyrene (PS) spheres are shown in **Figure 1c,d**. In this case, a monolayer assembly of PS spheres was targeted. It can be clearly observed that the pore walls are extremely narrow and, in some locations, they are even below 10 nm. In addition, transmission electron microscopy (TEM) imaging performed on a multilayer sample reveals that the pore walls are, in turn, porous (as shown in **Figure 2**). We can, therefore, consider that the pore walls are equivalent to ultrathin

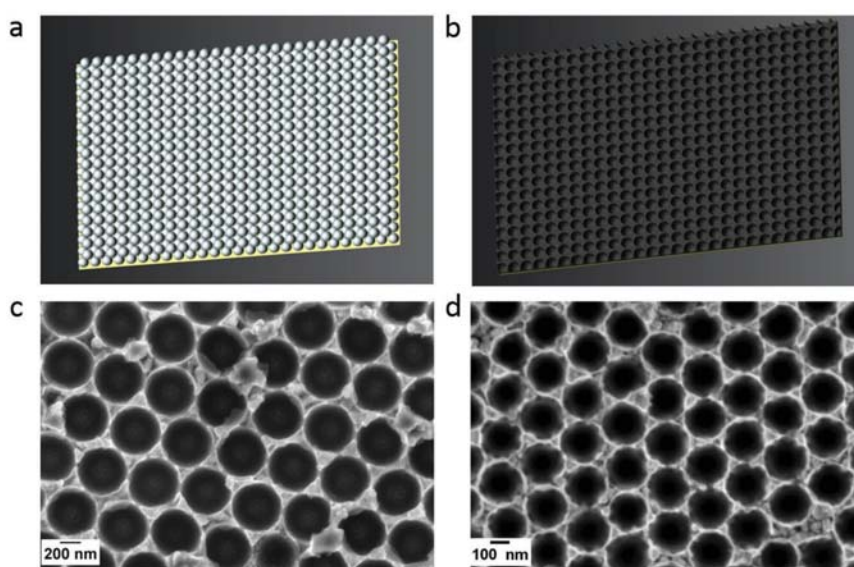


**Figure 1.** Schematic drawings of a) the assembly of PS spheres onto the metallized Si substrate and b) the electrodeposited Fe–Cu film after removal of the nanospheres. FESEM images of resulting Fe–Cu films of c) 500 and d) 200 nm pore size.

films for the purpose of assessing eventual voltage-driven magnetoelectric effects. Also, it should be noted that, while the films were electroplated under the same conditions, the composition for the 500 and 350 nm pore dimensions was  $\approx 85$  at% Fe while for the smallest sphere size of 200 nm the atomic percentage of Fe fell to 75 at%. This is on account of the formation of expectedly narrower interstices during packing of the smallest 200 nm diameter PS spheres. Since deposition of Cu is mass transport controlled,<sup>[23]</sup> Cu cations can probably infiltrate the spaces between the spheres in a more facile manner, thus resulting in compositions slightly more depleted in Fe. Another reason could be that the potential inside the spaces was positively shifting from the overpotential for Fe reduction as the cavity size decreased.

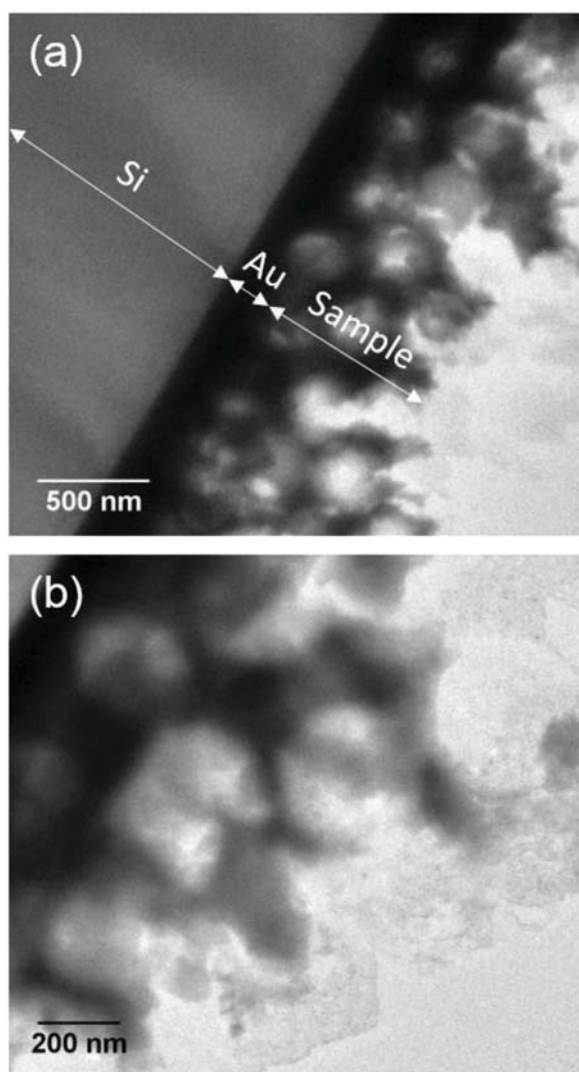


**Figure 2.** Transmission electron microscopy (TEM) images of a cross section of a porous Fe–Cu electrodeposited film (obtained using colloidal templating with spheres of 350 nm), revealing that the walls of the pores are not fully dense.

To evaluate the average degree of porosity inherent in the material, we first carried out spectroscopic ellipsometry on the reference electroplated (continuous, i.e., unpatterned and multilayer samples of three macropore sizes) and sputtered samples of similar composition. The optical properties for the sputtered sample are shown in **Figure 3a**. The refractive index

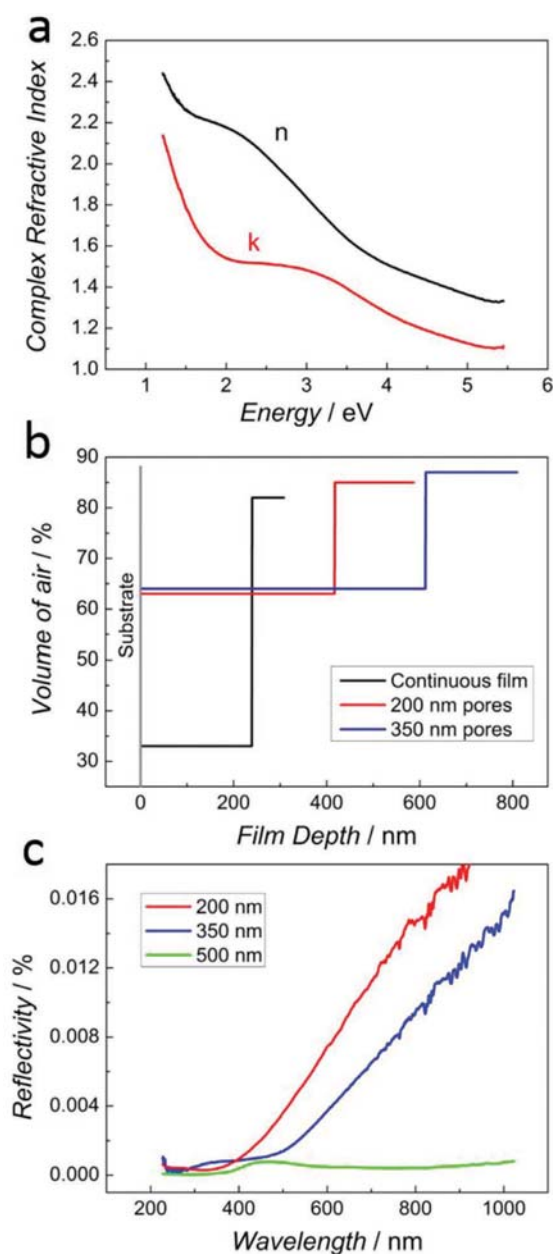


**Figure 3.** Results from ellipsometry measurements related to a) optical properties derived from sputtered sample (compact reference), b) volume of air contained in electroplated continuous film compared to porous samples when modeling the films as two sublayers with different void content, and c) reflectivity of porous deposits at an incident angle of  $30^\circ$ .



of this sample was then used as a reference to model the data for the electroplated samples and infer the average air content by taking the effective medium approximation of the optical properties via the Bruggeman model.<sup>[24]</sup> For the electroplated samples, two clear observations could be made. First, all electroplated samples, including the continuous case, exhibit a lower density compared to the sputtered sample, as the models contain large amounts of air (i.e., voids). Since the crystalline structure is the same, the lower density is here ascribed mainly to some degree of nanoscale porosity. The electroplated continuous film contained about a 33% volume fraction of air compared to the sputtered reference sample. This result from ellipsometry can be further supported by high magnification FESEM images (not shown) which reveal the existence of dispersed nanopores. In comparison, the use of colloidal templating increased the porosity value to around 65%. This is compatible with a hierarchical distribution of pores.

The second observation is that the air distribution is not homogeneous throughout the depth of the films, as the outer surface appears to be much more porous than the inner layers. Approximated depth profiles of air within the films are shown in Figure 3b for a simple description of the layer as two sub-layers with different void fractions (see the Experimental Section for details). In this graph, the zero in the X-axis corresponds to the substrate, and the curves extend through the depth of the film until the total thickness is reached (where each horizontal line finishes abruptly), thus marking the surface with air. This dual porosity results in a gradual variation of the index of refraction, akin to an antireflective coating, which results in a very low reflectivity in these materials (Figure 3c). The reflectivity becomes lower with increasing pore size, as the refractive index decreases (reducing index contrast with air) and scattering increases due to pore dimensions which become comparable to the wavelength of light.

## 2.2. Magnetoelectric Measurements and Coercivity Reduction

The magnetoelectric measurements were performed with samples obtained using each distinct colloidal sphere size (with a monolayer thickness, i.e., resulting from plating between the interstices of a single layer of PS spheres, to reduce the lack of reflectivity issues), as well as with the sputtered and electroplated continuous Fe<sub>85</sub>Cu<sub>15</sub> samples. The formation of an electrical double layer at the pore walls/electrolyte interface (as depicted in Figure 4a) caused the existence of large electric fields upon application of external voltages.

The protocol followed was to initially record a hysteresis loop at 0 V, then gradually increase the applied voltage in a stepwise manner up to +13 V and record the loops at each value of applied voltage. It was first observed that application of positive values of voltage does not lead to a substantial change in coercivity (Figure 4c). The coercivity remained the same even when applying voltages as high as +25 V. Subsequently, a waiting time of 20 min was introduced after which the sample was again measured at 0 V (with no appreciable changes with respect to the pristine as-deposited sample). Next, the voltage was decreased in steps until reaching -25 V. A clear coercivity reduction was observed for the three porous samples, with

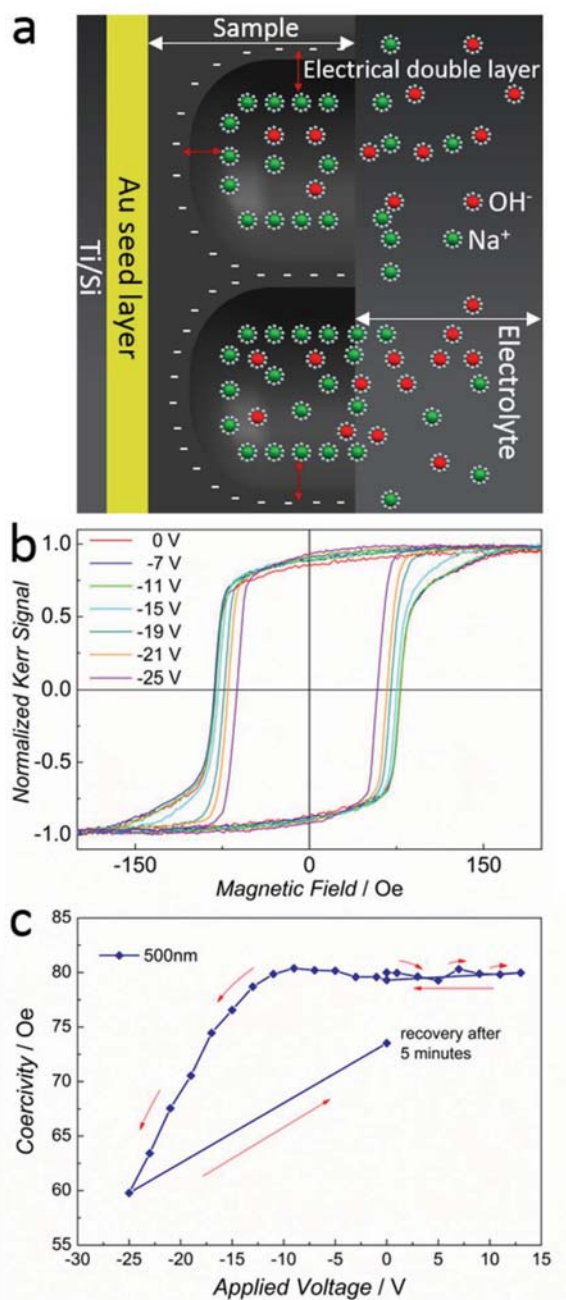


**Figure 4.** a) Schematic drawing to illustrate the formation of the electrical double layer at pore walls/electrolyte interface. b) Hysteresis loops captured for different values of applied voltage and c) voltage dependence of coercivity in the range of +13 to -25 V for the 500 nm pore sample.

≈21.6, ≈23.3, and ≈25.3% decrease for the 200, 350, and 500 nm samples, respectively. These changes are considerably more pronounced than those observed in the seminal work by Weisheit et al. in ultrathin (nonporous) FePt and FePd films (where the

maximum decrease in  $H_c$  was only 4.5%).<sup>[2]</sup> The most pronounced  $H_c$  modulation from 0 to  $-25$  V found for the 500 nm pore sample is illustrated in Figure 4b,c. Figure 5 shows the dependence of  $H_c$  on applied voltage for the 350 and 200 nm sphere diameters. Importantly, the Kerr amplitude (which is proportional to the saturation magnetization in a first approximation) does not show variations for different voltage values. As expected, for the sputtered, virtually pore-free film, no  $H_c$  changes were observed with variation of the applied voltage. Finally, the electrodeposited continuous film showed only small fluctuations with an average coercivity value of  $\approx 117$  which indicates that the electrolyte is interacting mainly with the surface but could not easily get infiltrated into the film. Moreover, it is apparent that the inherent nanoporosity of the material is not sufficient to induce any sizable magnetoelectric effects in the absence of the well-defined, ultrathin pore walls. Therefore, the results confirm that the porous structure created by colloidal templating is indeed essential for the magnetoelectric effect as it allows for the diffusion of the electrolyte throughout the entire porous network and leads to extremely thin pore walls which are, in a sense, equivalent to ultrathin films.

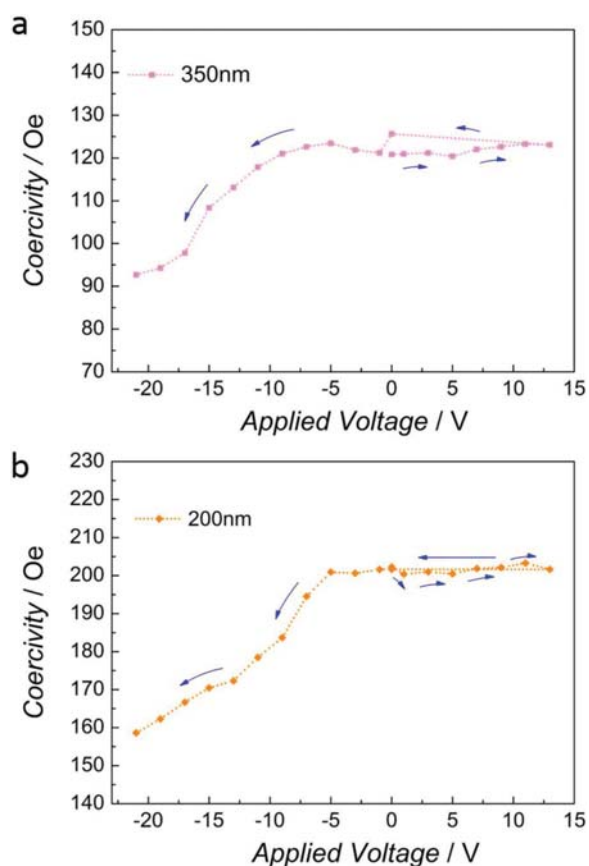


**Figure 5.** Dependence of the coercivity on the applied voltage for the electrodeposited Fe–Cu films grown using colloidal templated substrates, with spheres of a) 350 and b) 200 nm.

### 2.3. Investigation of Crystalline Structure and Surface Elemental Composition during Voltage Actuation

Upon verification of the feasibility of the voltage control of magnetism for the hierarchically porous Fe–Cu deposits, further examination of their structural characteristics and surface composition was carried out with a special emphasis on identifying and tracking any eventual changes resulting from the application of voltage, which could contribute to the observed magnetoelectric effects, besides the inherent electric charge accumulation. The grazing incidence X-ray diffraction (GIXRD) patterns of a representative multilayer sample of 350 nm macropore size in the as-prepared state (i.e., before any voltage manipulation) as well as after subjecting it to DC voltages of  $+13$  V for 20 min and  $-15$  V for 20 min, are shown in Figure 6. As can be readily discerned, there are no detectable shifts in the diffraction peaks for the large negative and positive voltage values (i.e., no changes in the cell parameter). In addition, no other peaks (e.g., stemming from oxidation or a phase transition) were visible either. It should be noted that all the porous films present the same peaks corresponding to body-centered cubic (bcc) Fe and are, therefore, single phase. Typically, phase separation into bcc and face-centered cubic (fcc) phases can occur in this range of compositions for electrodeposited Fe–Cu films with a thickness of several micrometers.<sup>[25]</sup> However, it was confirmed that this was not the case for continuous films of 250–300 nm thickness as in our case (only peaks from bcc Fe were observed, not shown). Additionally, in the multilayer porous films, the formation of a single phase is promoted by the forced growth in the narrow interstices between the PS spheres. It has been previously shown that confining electrodeposition in narrow cavities close to or comparable to crystallite size can suppress phase separation.<sup>[23]</sup> Thus, the GIXRD results clearly indicate that the films remain unaltered during the voltage application.

Subsequently, the chemical composition of the uppermost surface layer was examined using X-ray photoelectron spectroscopy (XPS). This revealed the presence of mainly Fe and Cu oxides at the surface (i.e., a thin oxide passivation layer), which were not detectable by XRD as they are below the threshold

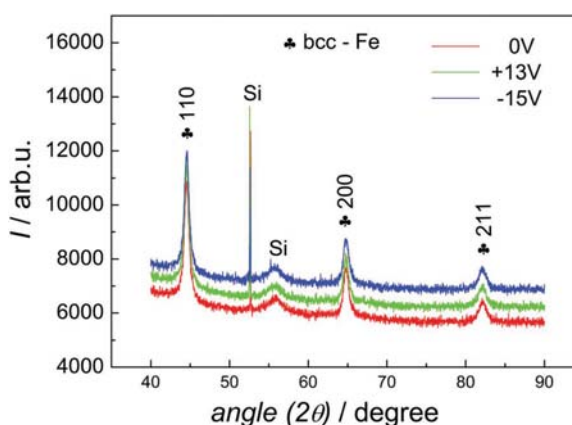


**Figure 6.** X-ray diffractograms of a representative sample taken in as-prepared condition and following negative and positive values of voltage applied.

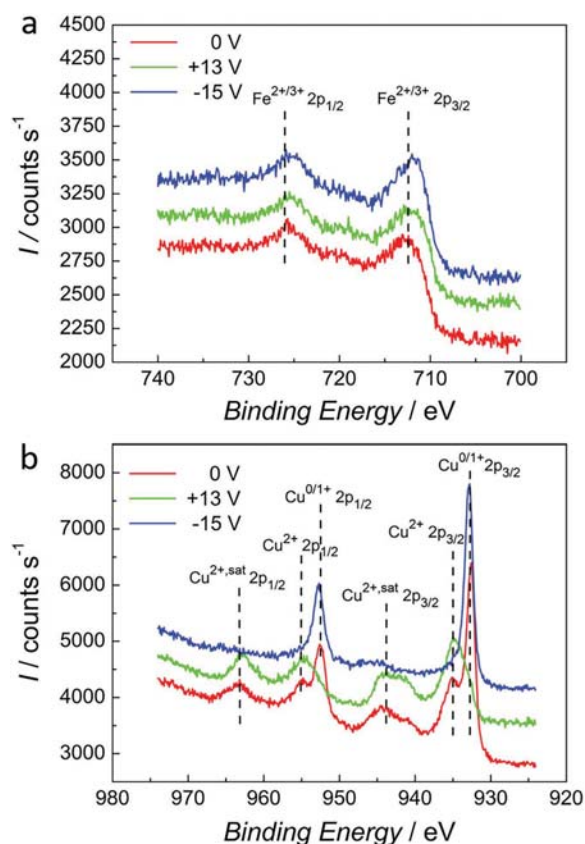


**Figure 7.** XPS detail spectra of a) Fe 2p and b) Cu 2p peaks of a chosen sample taken at as-prepared conditions and after voltage modulation.

detection limit. As seen in **Figure 7a** for the sample of 350 nm pore size, there is no appreciable change in the oxidation state of Fe which presents mainly as a mixture of Fe<sup>2+</sup> and Fe<sup>3+</sup> oxidation states. Contrarily, as shown in **Figure 7b** there is a clear shift in the Cu oxidation states, where for +13 V there is an enhancement of the Cu<sup>2+</sup> peak. When the negative voltage of -15 V is applied, the Cu<sup>2+</sup> peak and corresponding satellites are diminished and the Cu<sup>0/1+</sup> peak emerges strongly due to reduction. These structural changes seem to be mainly limited to the uppermost surface and, remarkably, the Fe peaks remain virtually unaltered. Additionally, it should be emphasized that a Cu enrichment of the Fe–Cu solid solution would have resulted in a reduction in saturation magnetization, and in eventual shifts in the XRD peaks, which is shown not to be the case. Finally, it was previously established that a higher Cu content in the electrodeposited Fe–Cu films actually causes an increase in  $H_c$  rather than the reduction observed here for negative voltages.<sup>[25]</sup> Therefore, the structural changes induced by the electric field observed in this system mainly influence the Cu species at the surface, whereas the Fe species controlling the magnetic behavior remain unaltered. Consequently, redox effects cannot be advocated to explain the voltage-induced coercivity changes, which should then be mainly attributed to the carrier accumulation magnetoelectric effect. Indeed, iron has four unpaired 3d electrons with a high density of states near the

**Table 1.** Summary of results from cyclability measurements using the 500 nm pore sample.

Wait time [min]	$H_c$ at an applied voltage of +21 V	$H_c$ at an applied voltage of -21 V
0	–	68
2	74	72
4	74	65
6	72	69

Fermi level due to the narrow 3d band. These electrons function as the free charge carriers of the surface which govern the magnetic properties. The application of a high voltage alters the surface charge and can thereby modify the magnetic behavior, as has been demonstrated by ab initio calculations.<sup>[26]</sup> The fluctuation in the number of 3d electrons has a direct influence on the magnetocrystalline anisotropy,<sup>[10,27]</sup> and thus on coercivity.

Finally, 5 min after removal of the voltage, a final hysteresis loop was recorded showing good recovery of the system (**Figure 4c**). The samples also showed good cyclability with alternating positive and negative voltage application. The corresponding  $H_c$  values during successive alternation between +21 and -21 V of applied voltage are summarized in **Table 1**. The wait time refers to both the time between positive and negative applied voltages as well as before starting the next pair of measurements.

### 3. Conclusions

Porous, pseudo-ordered thin metallic films consisting of non-toxic, abundant elements and prepared using a simple, easily reproducible and environmentally friendly process have been fabricated. The magnetic properties can be controlled by voltage application in a facile manner at ambient conditions leading to a reversible coercivity reduction of around 25%. According to the analysis of the film properties in the as-fabricated state as well as after voltage application the phenomenon can be mainly ascribed to carrier accumulation/dissipation. In view of these properties, the films are good candidates for voltage control magnetic applications aimed at minimization of power consumption.

### 4. Experimental Section

**Sample Preparation, Hard-Templating Procedure, and Electrodeposition of Porous Fe–Cu Films:** Silicon/silicon dioxide (Si/SiO<sub>2</sub>) substrates with a 10 nm Ti adhesion layer and a 90 nm Au seed layer and cut into 1 × 1.5 cm<sup>2</sup> dimensions were used with a working area of 1 ± 0.1 cm<sup>2</sup>. Prior to use, the substrates were cleaned consecutively with acetone, isopropanol, and Milli-Q water. As a preparation for electrophoretic deposition, they were treated with a 10 × 10<sup>-3</sup> M solution of 3-mercaptopropanesulfonic acid sodium salt (MPS) in ethanol at 50 °C for 1 h to increase the wettability of the surface.<sup>[28]</sup> Finally, they were alternately rinsed in Milli-Q water and ethanol to remove excessive MPS layers.

Electrophoretic deposition was implemented using a Keysight B2902A Precision Source/Measure Unit as a voltage source and a custom 3D-printed cell consisting of a 1 cm × 1 cm × 0.6 cm poly(methyl methacrylate) (PMMA) chamber attached to a platinized titanium sheet serving as a counter electrode. Monodisperse polystyrene (PS) sub-micrometer spheres with three different diameters (200, 350, and 500 nm) in a 2.5% w/v solid-liquid suspension were purchased from Polysciences, Inc.

The final solution was prepared by mixing of the PS sphere suspension (0.05 mL) in ethanol (0.45 mL) and was added to the custom cell covering a 1 cm<sup>2</sup> area of the substrate which was secured by slots at the back of the chamber at a 0.5 cm distance from the counter electrode. A constant potential of 40 V cm<sup>-1</sup> in the case of the two smaller sphere sizes and of 60 V cm<sup>-1</sup> for the largest spheres was applied with deposition times of 1 and 5 min, respectively.<sup>[28]</sup> The deposition time was tuned to allow for either monolayer or multilayer assemblies while preserving quality regarding stability and number of defects. Following the electrophoretic deposition, the samples were promptly placed on a hot plate and heated at 50 °C for 15 min to evaporate the ethanol and stabilize the assembled PS sphere layers.<sup>[28]</sup>

Electrodeposition was carried out using a three-electrode cell connected to a Metrohm/Eco Chemie Autolab PGSTAT302N potentiostat/galvanostat. A Pt wire served as the counter electrode and a double junction Ag|AgCl ( $E = +0.210$  V/SHE) as the reference electrode. The electrolyte (100 mL) was prepared with Millipore Milli-Q water and ACS Reagent grade chemicals purchased from Sigma-Aldrich and contained (NH<sub>4</sub>)<sub>2</sub>Fe(SO<sub>4</sub>)<sub>2</sub>·6H<sub>2</sub>O (58.8 g L<sup>-1</sup>), CuSO<sub>4</sub>·5H<sub>2</sub>O (1.25 g L<sup>-1</sup>), C<sub>6</sub>H<sub>11</sub>NaO<sub>7</sub> (22.9 g L<sup>-1</sup>), NaC<sub>12</sub>H<sub>25</sub>SO<sub>4</sub> (0.2 g L<sup>-1</sup>), and C<sub>7</sub>H<sub>5</sub>NO<sub>2</sub>S (0.46 g L<sup>-1</sup>). The samples were deposited from the as-prepared solution with a pH of 4.1 at a temperature of 35 °C. The optimized electrolyte composition and plating conditions were established previously with unpatterned substrates.<sup>[25]</sup> Current densities of -25 mA cm<sup>-2</sup> and deposition times between 15 and 50 s depending on the diameter of the previously deposited spheres and the desired thickness were applied. Finally, the PS spheres were removed by immersing the samples in chloroform for 3 h followed by a final rinsing in acetone, ethanol, and MQ-water. Unpatterned, continuous Fe-Cu films of 250–300 nm in thickness were prepared whenever needed and used as control samples.

**Characterization Techniques:** The sample morphology was imaged by scanning electron microscopy using a Zeiss MERLIN FESEM. The elemental composition was determined by energy dispersive X-ray spectroscopy (EDXS) at an acceleration voltage of 15 kV. The crystallographic structure of the deposits was studied by GIXRD using a Bruker-AXS, model A25 D8 Discover equipped with a LinxEye XE-T detector using CuK $\alpha$  radiation and a grazing incidence angle of 1°. For the surface elemental composition and oxidation state detection, XPS analyses were carried out on a PHI 5500 Multitechnique System spectrometer from Physical Electronics with a monochromatic X-ray source placed perpendicular to the analyzer axis and calibrated using the 3d<sup>3/2</sup> line of Ag. TEM analyses were performed with a Jeol-JEM 2011 system with a field emission gun operating at 200 kV.

**Ellipsometry Measurements and Data Analysis:** In order to quantitatively account for the porosity degree of the electrodeposited Fe-Cu films, these were characterized by ellipsometry. A virtually fully dense, sputter-deposited, Fe-Cu film of  $\approx 100$  nm thickness was prepared by co-sputtering using an AJA International, Inc. magnetron sputtering system and was taken as a reference. Fe was sputtered at 200 W (direct current, DC) and the Cu at 20 W (radio frequency, RF) for 20 min. Variable angle spectroscopic ellipsometry and reflectivity were measured using a Sopralab GES5E rotating polarizer ellipsometer with a focused spot size of  $\approx 250$   $\mu$ m and CCD detection. At least three angles of incidence were measured for each sample. The angles were adjusted to be around the Brewster angle for each sample, which decreased with pore size as one would expect for a lower refractive index. The data were analyzed using the WinElli II software. For the sputtered sample, a two semi-infinite media approximation was applied for the direct inversion of the ellipsometric angles. The data for the electroplated samples were analyzed within the effective medium approximation, mixing the reference optical properties (those deduced for the sputtered sample) and void. Note that as the pore diameter increases, this approximation loses its validity. This was indeed observed in a worsening of the fit quality with increasing pore diameter, particularly for the data of the 500 nm pore sample. It was found that fits that assumed a homogeneous volume fraction throughout the film did not result in acceptable fits of the experimental data. The standard deviation of the fit was improved by a factor of about 5 by modeling the sample as containing two sublayers

with different void content, thus strongly indicating the existence of a gradient of composition through the depth of the film, in agreement with SEM cross sections. More elaborate models, including concentration profiles or a larger number of sublayers, were also employed to analyze the data but reliable fit improvements could not be obtained due to the relatively large experimental uncertainty related to the large pore size.

**Magnetolectric Measurements:** In-plane hysteresis loops were recorded using a magneto-optical Kerr effect (MOKE) setup from Durham Magneto-Optics while applying different values of DC voltage at ambient conditions using the Keysight B2902A unit as a source. The sample was mounted vertically on a custom 3D-printed PMMA base and placed in a quartz SUPRASIL cell filled with anhydrous propylene carbonate containing Na<sup>+</sup> ions.<sup>[3]</sup> The sodium cations served a dual function of reacting with any water entering the system to form NaOH as well as to enhance the electrical double layer owing to the presence of the dissolved Na<sup>+</sup> and OH<sup>-</sup> ions.<sup>[3]</sup> The anhydrous nature of the electrolyte minimized oxidation of the Fe-Cu during the measurements. After each change of the value of applied voltage, a waiting period of 300 s was introduced before recording the hysteresis loop to allow the electrolyte to enter the pore network and the electrical double layer to form.<sup>[3]</sup>

## Acknowledgements

This work was supported by the SELECTA (No. 642642) H2020-MSCA-ITN-2014 project. Partial financial support by the Spanish Ministry of Economy, Industry and Competitiveness (MINECO) (Project Nos. MAT2017-86357-C3-1-R, MAT2015-70850-P and associated FEDER), the Generalitat de Catalunya (2017-SGR-292), and the European Research Council (SPIN-PORICS and FOREMAT, with Agreement Nos. 648454 and 648901, respectively) is acknowledged. E.P. is grateful to MINECO for the “Ramon y Cajal” contract (RYC-2012-10839). The ICN2 is funded by the CERCA programme/Generalitat de Catalunya. The ICN2 is supported by the Severo Ochoa programme of MINECO, grant no. SEV-2013-0295. The authors thank Alberto Quintana and Eloy Isarain-Chávez for providing the custom cell for magnetolectric measurements, as well as Dr. Agustín Mihi (ICMAB-CSIC) for additional FTIR measurements and useful discussion regarding the photonic properties of these systems.

## Conflict of Interest

The authors declare no conflict of interest.

## Keywords

coercivity, colloidal templating, electrodeposition, hierarchical porosity, magnetolectric effects, voltage-driven effects

Received: April 2, 2018

Revised: May 17, 2018

Published online: June 20, 2018

[1] C. Song, B. Cui, F. Li, X. Zhou, F. Pan, *Prog. Mater. Sci.* **2017**, *87*, 33.

[2] M. Weisheit, S. Fähler, A. Marty, Y. Souche, C. Poinsignon, D. Givord, *Science* **2007**, *315*, 349.

[3] A. Quintana, J. Zhang, E. Isarain-Chávez, E. Menéndez, R. Cuadrado, R. Robles, M. D. Baró, M. Guerrero, S. Pané, B. J. Nelson, C. M. Müller, P. Ordejón, J. Nogués, E. Pellicer, J. Sort, *Adv. Funct. Mater.* **2017**, *27*, 1701904.

[4] C. A. Vaz, *J. Phys. Condens. Matter.* **2012**, *24*, 333201.

[5] C. Bi, Y. Liu, T. Newhouse-Illige, M. Xu, M. Rosales, J. W. Freeland, O. Mryasov, S. Zhang, S. G. E. Te Velthuis, W. G. Wang, *Phys. Rev. Lett.* **2014**, *113*, 267202.

- [6] F. Matsukura, Y. Tokura, H. Ohno, *Nat. Nanotechnol.* **2015**, *10*, 209.
- [7] M. Ghidini, F. Maccherozzi, X. Moya, L. C. Phillips, W. Yan, J. Soussi, N. Métallier, M. E. Vickers, N. J. Steinke, R. Mansell, C. H. Barnes, *Adv. Mater.* **2015**, *27*, 1460.
- [8] M. Liu, N. X. Sun, *Philos. Trans. R. Soc. A* **2014**, *372*, 20120439.
- [9] T. Maruyama, Y. Shiota, T. Nozaki, K. Ohta, N. Toda, M. Mizuguchi, A. A. Tulapurkar, T. Shinjo, M. Shiraishi, S. Mizukami, Y. Ando, *Nat. Nanotechnol.* **2009**, *4*, 158.
- [10] U. Bauer, M. Przybylski, G. S. Beach, *Phys. Rev. B* **2014**, *89*, 174402.
- [11] U. Bauer, L. Yao, A. J. Tan, P. Agrawal, S. Emori, H. L. Tuller, S. Van Dijken, G. S. Beach, *Nat. Mater.* **2015**, *14*, 174.
- [12] Y. Lee, Z. Q. Liu, J. T. Heron, J. D. Clarkson, J. Hong, C. Ko, M. D. Biegalski, U. Aschauer, S. L. Hsu, M. E. Nowakowski, J. Wu, *Nat. Commun.* **2015**, *6*, 5959.
- [13] D. Chiba, S. Fukami, K. Shimamura, N. Ishiwata, K. Kobayashi, T. Ono, *Nat. Mater.* **2011**, *10*, 853.
- [14] D. Chiba, T. Ono, *J. Phys. D* **2013**, *46*, 213001.
- [15] Y. Li, W. Z. Jia, Y. Y. Song, X. H. Xia, *Chem. Mater.* **2007**, *19*, 5758.
- [16] J. Zhang, M. D. Baró, E. Pellicer, J. Sort, *Nanoscale* **2014**, *6*, 12490.
- [17] H. Atae-Esfahani, L. Wang, Y. Nemoto, Y. Yamauchi, *Chem. Mater.* **2010**, *22*, 6310.
- [18] L. Wang, Y. Yamauchi, *Chem. Mater.* **2011**, *23*, 2457.
- [19] B. Jiang, C. Li, V. Malgras, M. Imura, S. Tominaka, Y. Yamauchi, *Chem. Sci.* **2016**, *7*, 1575.
- [20] C. Li, T. Sato, Y. Yamauchi, *Angew. Chem., Int. Ed.* **2013**, *52*, 8050.
- [21] H. Wang, H. Y. Jeong, M. Imura, L. Wang, L. Radhakrishnan, N. Fujita, T. Castle, O. Terasaki, Y. Yamauchi, *J. Am. Chem. Soc.* **2011**, *133*, 14526.
- [22] P. M. Tessier, O. D. Velev, A. T. Kalambur, A. M. Lenhoff, J. F. Rabolt, E. W. Kaler, *Adv. Mater.* **2001**, *13*, 396.
- [23] Z. Liu, G. Xia, F. Zhu, S. Kim, N. Markovic, C. L. Chien, P. C. Searson, *J. Appl. Phys.* **2008**, *103*, 064313.
- [24] H. Tompkins, E. A. Irene, *Handbook of Ellipsometry*, William Andrew, Norwich, NY **2005**.
- [25] E. Dislaki, J. Sort, E. Pellicer, *Electrochim. Acta* **2017**, *231*, 739.
- [26] K. Nakamura, R. Shimabukuro, Y. Fujiwara, T. Akiyama, T. Ito, A. J. Freeman, *Phys. Rev. Lett.* **2009**, *102*, 187201.
- [27] G. H. O. Daalderop, P. J. Kelly, M. F. H. Schuurmans, *Phys. Rev. B* **1991**, *44*, 12054.
- [28] J. Pokki, O. Ergeneman, K. M. Sivaraman, B. Özkale, M. A. Zeeshan, T. Lühmann, B. J. Nelson, S. Pane, *Nanoscale* **2012**, *4*, 3083.

---

## **Electrodeposited compositionally graded micron- and submicron-scale magnetic structures, tubes and rods patterned via hard templating and lithographic techniques**

In the interest of maintaining consistency throughout the thesis, this chapter is structured as a research article.

### **Abstract**

In this work, micron- and submicron-scale Fe–Cu structures were electrodeposited onto pre-patterned gold-coated substrates forming nine 100  $\mu\text{m}$  x 100  $\mu\text{m}$  arrays of three selected geometries (cylindrical, rectangular and cruciform), each featuring three different sizes. These Cu-rich structures were found to exhibit a gradient in composition by along their thickness with copper enrichment at the uppermost surface. Confined growth in the restricted cavities resulted in a nanoscale grain size leading to well-defined sharp edges. Magnetic force microscopy revealed virtually no contrast at zero field, suggesting magnetic curling effects (instead of coherent rotation) during magnetization reversal. Subsequently, Fe-rich rods and tubes of various diameters, ranging from 200 nm to 2  $\mu\text{m}$ , were electrodeposited into track-etched polycarbonate membranes using baths with and without a nonionic surfactant. A compositional gradient, which occurred as an intrinsic characteristic of the

preparation technique as well as through deliberate alteration of the overpotential of deposition for the creation of distinct Cu-rich and Fe-rich segments, was observed through energy-dispersive X-ray spectroscopy (EDX) mapping. The 2  $\mu\text{m}$  microtubes show photocatalytically driven propulsion while the ferromagnetic properties of the rods and tubes can be exploited in magnetically-driven devices.

#### 4.1. Introduction

Since the discovery of giant magnetoresistance (GMR) and its implementation in magnetic field sensors,<sup>1</sup> the field of nanomagnetism has experienced rapid developments in the last decades given the novel properties that have been discovered in the field of spintronics with major implications for data processing and storage<sup>2,3</sup> as well as the highly promising and fascinating functionalities of flexible electronics.<sup>4</sup> The growing trend towards miniaturization faces challenges related to spin wave guidance<sup>5</sup> and the superparamagnetic limit which need to be addressed in a holistic approach that combines several traditional disciplines under the umbrella of nanomagnetism.<sup>6</sup> The vast majority of existing studies have focused on two-dimensional nanomagnetism where single- or multi-layer films and structures are confined to a thickness that leads to monodomain magnetic states in the vertical direction and interesting functionalities are achieved by capitalizing on interfacial effects. Nevertheless, new fabrication and characterization techniques enable the expansion of nanomagnetism into three dimensions where unconventional spin textures bring about remarkable new phenomena involving geometry, topology and chirality. Indeed, patterned 3D nanostructures can revolutionize sensing technology, ultrahigh density magnetic recording and the Internet-of-Things (IoT) while 3D nano- and micro-scale magnetically actuated motors are essential for mechano-biology applications.<sup>7</sup>

From a synthesis point of view, electrodeposition is widely used due to its conformal coverage, control of grain size and crystallinity and fast growth rates. When combined with ultra-high-resolution electron-beam lithography, well-defined nano-motifs can be created. The height of the submicron motifs produced by physical vapor deposition (PVD) approaches is typically below 50 nm<sup>8,9</sup> and in order to reach an approximate

thickness of 200 nm several successive time-consuming steps including sputter etching can be involved.<sup>10</sup> Contrarily, it is easily possible to achieve a high aspect ratio with electroplating. Nevertheless, existing literature on electrodeposited 3D structures has thus far been focused on arrays of nanowires.<sup>11-13</sup> Nanowires can be realized by thin film patterning using nanolithographic techniques such as ion- and electron-beam lithography or nanoimprint. A limitation of these methods is that the nanowires are oriented parallel to the substrate (horizontal) whereas by electrodeposition one can easily prepare vertical nanowires. Another downside is that the composition is uniform along the nanowire axis. Compositionally graded nanowires have been prepared by spatial gradient of source materials and control of local substrate temperature in chemical vapor deposition.<sup>14,15</sup> A more elegant, straightforward and fast approach involves growth of dense nanowire arrays in templates, such as anodic aluminum oxide (AAO), polycarbonate (PC) track etched membranes or diblock copolymers by electrochemical methods at ambient temperature and pressure (unlike vacuum deposition methods).<sup>16,17</sup>

Herein compositionally graded micron and submicron Fe–Cu structures organized in nine 100  $\mu\text{m}$  x 100  $\mu\text{m}$  arrays of three select shapes (disks, stripes and crosses) and of three sizes each have been prepared by electrodeposition onto e-beam lithographed substrates from an aqueous sulfate-based electrolyte with saccharin added as a grain refiner.<sup>18</sup> Morphological and structural information was obtained by scanning electron microscopy (SEM), atomic force microscopy (AFM) and transmission electron microscopy (TEM). The structures were very well-resolved and relatively smooth with a thickness ranging between 200-300 nm while plating time was as low as 3.5 s, i.e. much faster than reported by PVD techniques. The lithography process was also optimized in order to reduce writing time to less than 1 h. Overall composition was initially assessed by EDX/TEM while local elemental maps were obtained by EDX/TEM and electron energy loss spectroscopy (EELS). Magnetic properties were investigated using magnetic force microscopy (MFM) as well as using a vibrating sample magnetometer (VSM) for large single-feature arrays of three selected geometries and dimensions (small- and large-sized disks and medium crosses). Measurement by magneto-optical Kerr effect (MOKE) was attempted but made infeasible by Cu-



enrichment at the surface coupled by roughness which limits reflectivity since MOKE is a surface sensitive technique.

Subsequently, upright nanorods of 200 nm and tubes of 400 nm diameter were produced from an iron-copper electrolyte by electrodeposition into PC membranes both with and without the use of a nonionic surfactant. The rods and tubes were attached to a self-supporting Cu layer, which was sputtered onto a 200 nm-thick gold/palladium layer sputter coated on the back of the membrane. Additionally, compositionally graded free-standing microtubes were electrodeposited into PC membranes of 1  $\mu\text{m}$  and 2  $\mu\text{m}$  diameter. Imaging was performed by SEM and elemental maps of selected samples were also obtained by SEM/EDX. Magnetic manipulation of the fabricated tubes and wires was readily confirmed while the 2  $\mu\text{m}$  tubes show directional motion under visible light irradiation.

## 4.2. Experimental

### 4.2.1. Fabrication details

The lithography patterns were created with a FEI Quanta 3D dual beam FEG which combines a Focused Ion Beam (FIB) with a high-resolution Field Emission Gun Scanning Electron Microscope (FEG-SEM). Silicon/silicon dioxide (Si/SiO<sub>2</sub>) substrates were used with a 15 nm Ti adhesion layer and an 80 nm Au seed layer, both deposited by e-beam evaporation. The process was controlled by the Nanometer Patterning Generation System (NPGS) software. The information on the dimensions and positions of the different structures, the sizes of the arrays and their reciprocal position on the sample surface were contained in a computer-aided design (CAD) file managed by the NPGS. The features were designed with sufficient spatial separation so as to avoid the proximity effect. The electron dose was 400  $\mu\text{C cm}^{-2}$  for the smallest-sized feature arrays and 375  $\mu\text{C cm}^{-2}$  for the rest. The operating voltage was 30 KeV. Electrodeposition was carried out in a three-electrode cell connected to a Metrohm / Eco Chemie Autolab PGSTAT302N potentiostat / galvanostat. A Pt wire served as the counter electrode and a double junction Ag|AgCl ( $E = +0.210\text{V}/\text{SHE}$ ) electrode (Metrohm AG) with a 3M KCl inner solution and a 1M Na<sub>2</sub>SO<sub>4</sub> outer solution was used as a reference.

#### 4.2.2. Sample preparation and post-process treatments

Prior to lithography, the substrates were cleaned successively with acetone, isopropanol and de-ionized water. The substrates were subsequently spin-coated at 2000 rpm for 1 min with a layer of poly(methyl methacrylate) (PMMA) polymeric resist. This ensured that a homogenous layer of PMMA is formed on top of the conductive substrates. The thickness of the resist was around 300 nm, as measured by ellipsometry. After coating, the PMMA was heat treated for 5 min at 165 °C. Upon completion of the patterning procedure, the PMMA in the exposed regions was removed by placing the samples for 60 s in a 1:3 solution of 4-methyl-2-pentanone with isopropanol, followed by 20 s in isopropanol and, finally, 20 s in de-ionized water. Subsequent to electrodeposition, the samples were placed in acetone for 10 min to remove the remaining PMMA leaving behind the created structures of different geometries attached to the substrate. This was followed by a final rinsing in isopropanol and Milli-Q water.

The TEM lamella preparation was made on a dual beam Carl Zeiss Neon 40 station equipped with a Schottky FE-SEM and Ga<sup>+</sup> ion columns (CANION31, Orsay). The lamella originated from a section of the medium-sized cruciform structures. The region of interest was first covered with a thin Pt layer of approximately 200 nm using e-beam assisted Pt deposition. On top of the thin Pt layer, a thicker Pt layer (~500 nm) was added by ion-beam assisted Pt deposition. Both Pt layers are used in order to protect the underlying structures from ion beam damage during lamella preparation. After the Pt deposition, two 15 μm x 10 μm trenches on both sides of the lamella were made by successive coarse (30kV:10nA) and finer millings (30kV:2nA). In this way, a lamella with 15 μm length, 1 μm width and 8 μm depth was formed in the region of interest. This lamella was then lifted out using a Kleindiek micromanipulator with a tungsten microprobe. The tip of the probe was first attached to one side of the lamella by ion-beam assisted Pt deposition. The other side was cut using 30kV:500pA ion current. The lamella was then lifted out from the sample and then attached to a TEM grid also using ion-beam assisted Pt deposition. The microprobe tip was then cut by ion milling. The final step is polishing of the lamella up to electron transparency. Only a region of 5 μm width was polished in three different steps. Coarse polishing was

performed with 30kV:50pA ion current up to a thickness of about 120 nm. Next, fine polishing with a smaller ion dose (30kV:10pA) was used to achieve a thickness of about 60 nm. The final step was a quick polishing by just imaging the region of interest with low energetic beam (5kV:20pA) in order to reduce the Ga induced amorphization of the lamella walls. The electron transparency was monitored with the conventional Everhart-Thornley secondary electron detector. The metal-organic precursor used for the Pt deposition was trimethyl(methylcyclopentadienyl)platinum(IV) ( $C_9H_{16}Pt$ ).

Lastly, in preparation for the electrodeposition of the nano-/microrods and tubes, the PC membranes were sonicated in Milli-Q water for 5 min. The back of the membranes was sputter coated prior with a 200 nm thick gold-palladium layer to create a conductive substrate. For the fabrication of standing rods and tubes, a thick self-supporting layer of Cu of approximately 1  $\mu m$  was added using dc magnetron sputtering. After the conclusion of the plating process, the membranes were removed by immersing the samples in chloroform for 3 h. As a final step, the rods/tubes were sequentially cleaned with acetone, ethanol and Milli-Q water.

#### **4.2.3. Electrolytes and plating conditions**

The electrolytes were prepared with Millipore Milli-Q water and ACS Reagent grade chemicals purchased from Sigma-Aldrich. The solution for the patterned structures contained 58.8 g L<sup>-1</sup>  $(NH_4)_2Fe(SO_4)_2 \cdot 6H_2O$ , 0.625 g L<sup>-1</sup>  $CuSO_4 \cdot 5H_2O$ , 22.9 g L<sup>-1</sup> sodium gluconate, 0.2 g L<sup>-1</sup> sodium dodecyl sulfate and 0.46 g L<sup>-1</sup> saccharine (Solution A). The as prepared pH was 4.1 and the temperature was adjusted to 45 °C through use of an external thermostatisation jacket. Electrodeposition was carried out in potentiostatic mode at an applied potential of -1.1 V for 3.5 s with magnetic stirring at 300 rpm. For the nano-/microrods and tubes fabricated by the standard electrodeposition approach, the same bath was used but with an increase of the Cu salt concentration to 1.25 g L<sup>-1</sup> (Solution B). The operating temperature was set to 35 °C while plating times ranged between 2 min and 4 min and applied cathodic potentials of -1 V to -1.2 V were applied. Finally, for the nanorods prepared using electrodeposition with a nonionic surfactant, 0.45 mM Triton X-100 were added to Solution B which is well above the room temperature critical micelle concentration of 0.22 to 0.24 mM

according to the manufacturer (Solution C). Plating was performed at -1 V and -1.1 V with an electrolyte temperature of 45 °C.

#### **4.2.4. Characterization**

The morphology of the patterned structures was observed using a Zeiss MERLIN Field Emission Scanning Electron Microscope (FE-SEM) and the elemental composition was determined by energy dispersive X-ray spectroscopy at an acceleration voltage of 15 kV. Further chemical analysis at nanometer level and elemental mapping as well as study of crystal structure by selected area electron diffraction (SAED) was conducted with a FEI Tecnai G2 F20 200 kV field emission gun high resolution and analytical TEM/STEM. Atomic and magnetic force microscopy (AFM/MFM) were performed with a Bruker Multimode V Nanoscope 8 microscope operated in tapping mode and lift mode using a commercial cobalt alloy hard magnetic tip ( the coercive field is ~950 Oe for both in-plane and perpendicular orientation ). The magnetic domain evolution was studied by MFM under application of an in-plane magnetic field generated by an electromagnet with values up to 600 Oe. For further magnetic characterization, the samples were placed in a vibrating sample magnetometer (VSM) from LOT-Quantum Design and hysteresis loops were recorded at room temperature, along the in-plane direction with an applied field range of -20 kOe to 20 kOe. The micro- and nano-scale rods and tubes were imaged with a FEI Magellan 400L XHR SEM and a Zeiss Leo 1530 while EDX maps were obtained with the latter.

The photocatalytic performance of the Fe–Cu microtubes in H<sub>2</sub>O<sub>2</sub> aqueous solutions was investigated with an optical microscope (Olympus IX 81, Olympus Co., Japan) equipped with a mercury lamp (X-Cite 120, Excelitas Technologies, USA) and different light emissions were obtained through the use of filter cubes: 360–370 nm (UV), 420–440 nm (blue), 460–495 nm (cyan), 540–550 nm (green), 590–650 nm (red).

### **4.3. Results and discussion**

#### **4.3.1. Morphology of patterned structures**

While existing literature on lithographed patterns mainly focuses on the fabrication of cylindrical arrays,<sup>19-22</sup> this work targets more complex geometries. The dimensions of

the various motifs are given in **Table 4.1**. As can be viewed in **Figure 4.1**, the electrodeposited Fe–Cu arrays of different shapes and dimensions are quite smooth and have a well-defined geometry with sharp edges in the case of the medium- and large-sized crosses and stripes thanks to the small grain size achieved by electrodeposition. This is significant considering the submicron dimensions of the structures and, especially, the complex geometry of the cross-shaped motifs which are characterized by several edges separating them into segments along their axes of symmetry. The average height of the structures, as determined by AFM, was 180-200

**Table 4.1.** Detailed dimensions of the nine arrays of patterned structures.

Geometry	Dimensions		
	Small	Medium	Large
Stripes	150 nm x 450 nm	300 nm x 900 nm	450 nm x 1.35 $\mu\text{m}$
Disks	d: 200 nm	d: 500 nm	d: 1 $\mu\text{m}$
Crosses	300 nm x 500 nm	600 nm x 1 $\mu\text{m}$	900 nm x 1.5 $\mu\text{m}$

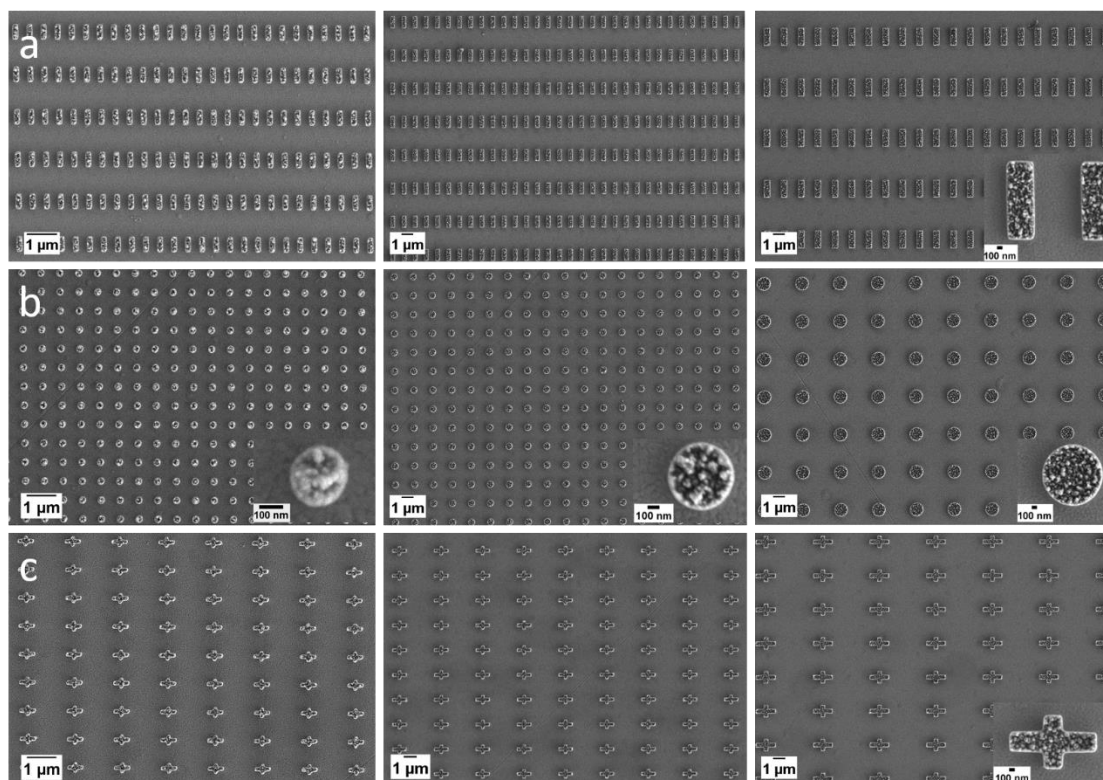


**Figure 4.1.** SEM micrographs of electrodeposited arrays of a) stripes, b) disks and c) crosses in three distinct sizes.

nm for the disks, 200-220 nm for the crosses and 190-210 nm for the stripes. These values are consistent considering that the deposition time was the same (3.5 s) for all structures. Interestingly, the medium-sized features were at the upper range limit for the height, followed closely by the small-sized motifs while the larger ones were the shortest and displayed more roughness due to increased deposition around the edges. The occurrence of donut-like structures due to an uneven distribution of the current density in the cavities can occur when electroplating dot arrays.<sup>23,24</sup> In the case of the Fe–Cu disks, it can be easily observed from the magnified insets in Figure 4.1 that the structures are fully plated in the center.

In **Figure 4.2**, AFM images of the large-sized structures are shown where the very small grain size is visible which resulted in the growth of well-resolved geometries despite the narrowness of the cavities especially at the corners. An inherent aberration connected to the interaction of the AFM tip with the structures leads to a blurring effect around the edges rendering an inaccurate representation of their lateral dimensions and spacing along the horizontal x-axis direction. This is especially true as feature size decreases and, consequently, the AFM image quality obtained for the smallest-sized structures was rather poor. Therefore, the SEM micrographs offer a direct representation of geometrical aspects while the AFM images act in a complementary manner to further investigate morphology and estimate height and roughness since very accurate measurements can be obtained in the z-axis direction. The color gradient in the images offers a representation of the roughness present at the surface of the structures while the color bar aids in assessing approximate height at different points.

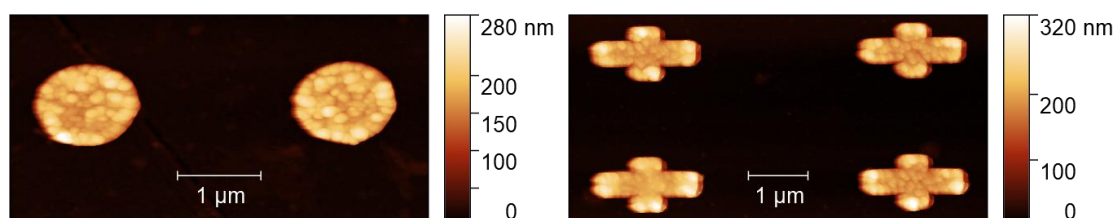


**Figure 4.2.** AFM images of large disks and crosses.

### 4.3.2. Chemical and structural analysis of structures

For the deposition of the submicron structures, the optimized electrolyte and plating conditions previously determined for the growth of Fe-rich continuous films were utilized.<sup>25</sup> The very short electrodeposition time of 3.5 s into submicron cavities and the use of potentiostatic mode for the structures as compared to galvanostatic for the films lead to a different composition than anticipated, namely 20 at% Fe and 80 at% Cu in average. In order to enhance Fe deposition, the Cu amount was then halved. Elemental analysis by SEM/EDX after this modification of the Cu salt concentration showed an average value of 45 at% Fe and 55 at% Cu which varied slightly for the different arrays. Notably, a compositional gradient can occur when depositing a system with low mutual solubility such as Fe–Cu into cavities of high aspect ratio, and thus the composition determined by SEM/EDX represents only an overall value with no further insights into deposit growth mechanisms. Therefore, a lamella was prepared from a section of the array of the intermediate-sized crosses for TEM characterization and the results of the STEM analysis are shown in **Figure 4.3**.

In Figure 4.3a, the indexed SAED pattern collected from a spot in the middle of the lamella displays small spots and rings confirming the nanocrystalline nature of the deposited structures. The measured interplanar distances indicate phase separation with partial alloying. From the high-resolution TEM image in Figure 4.3b, we can observe the sharply defined lattice planes. In Figure 4.3c, the quantitative TEM/EDX chemical maps, taken vertically starting from the substrate and extending beyond the surface, show a rather uniform distribution of Fe with a sudden decrease at the uppermost section while copper gradually increases as we approach the top. This indicates that, contrary to one would expect considering the nobility of Cu and Fe, iron plates preferentially during the first stages of electrodeposition. Oxygen is more concentrated close to the substrate within the Fe-rich area and then, as would be expected, above the surface of the lamella. Since Fe is prone to bond to oxygen leading to the formation of iron oxides and hydroxides, the co-presence of Fe and O in regions close to the substrate is thus anticipated. Likewise, passivation of the structures upon standing in air leads to the accumulation of oxygen at the surface of the lamella. These trends were further confirmed by line scans, which nevertheless revealed low oxygen

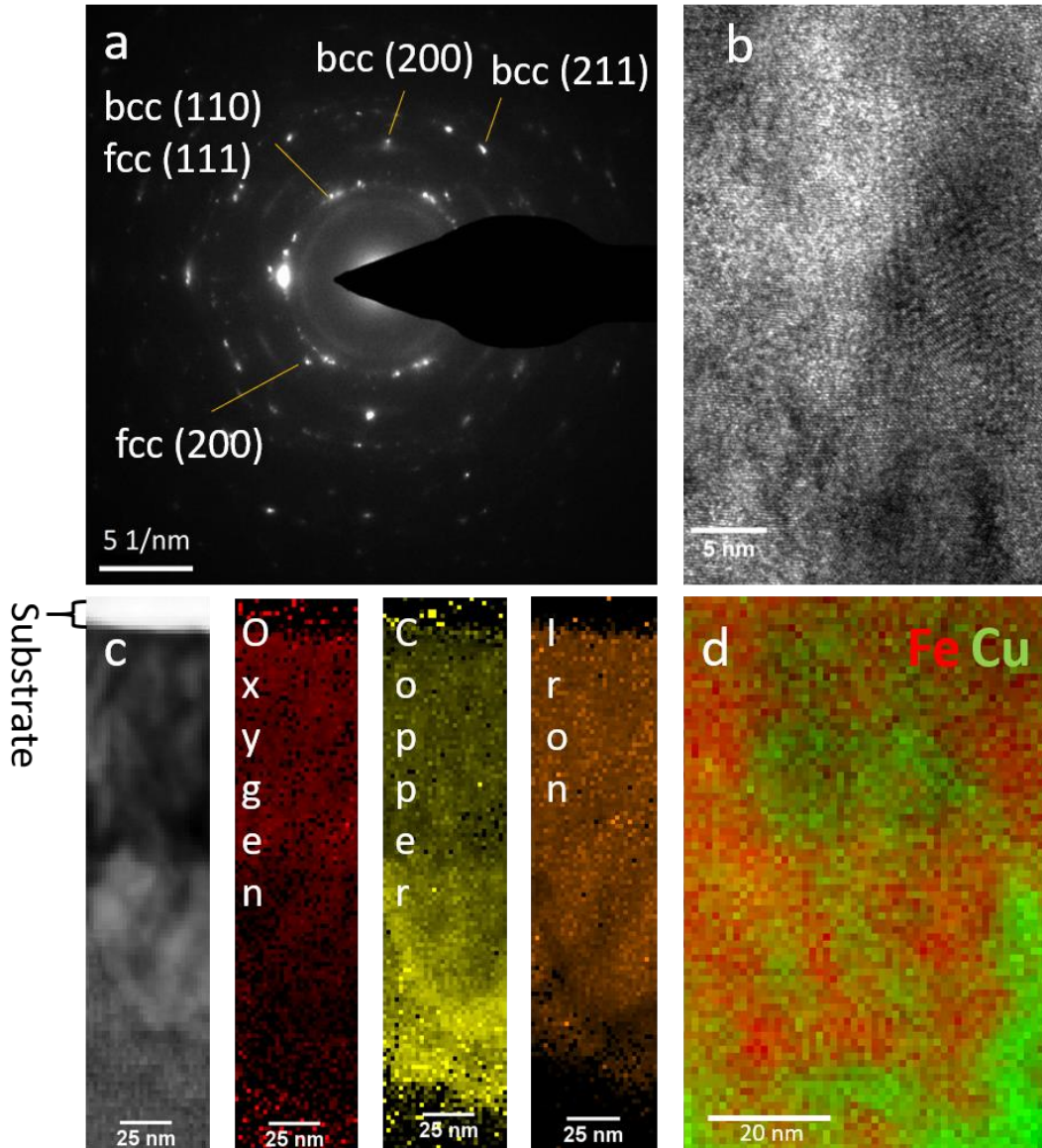


**Figure 4.3.** a) SAED pattern taken at an intermediate point in the sample where bcc and fcc correspond to Fe-rich and Cu-rich solid solutions, respectively b) HR-TEM image showing crystal lattice fringes, c) EDX/TEM compositional maps and d) EELS mixed elemental map. counts evincing that the deposits are mainly metallic. The EELS compositional map seen in Figure 4.3d displays Fe-rich and Cu-rich areas as well as areas with a mixed composition where partial alloying takes place. Quantification by EELS for this area showed an overall 83.5 at% Fe and 16.5 at% Cu content. It is likely that the copper enrichment at the top of the structures had influenced earlier quantification by EDX since the deposits are very Fe-rich as we move towards the substrate.

### 4.3.3. Magnetic characterization of the Fe–Cu motifs

In consideration of the stoichiometries of the structures as determined by SEM/EDX and EELS, it should be mentioned that the value of saturation magnetization for a



Fe<sub>39</sub>Cu<sub>61</sub> film was measured at approximately 83.7 emu g<sup>-1</sup> and for a Fe<sub>82</sub>Cu<sub>18</sub> film it was 171 emu g<sup>-1</sup>.<sup>25</sup> Consequently, despite the relatively high overall Cu content of these motifs, a clear magnetic response is expected. In order to study the magnetization reversal of the fabricated structures, each of the nine arrays was exposed to an in-plane static magnetic field of 600 Oe and images were recorded by magnetic force microscopy. Additional images were taken at remanence. The field was then applied in the opposite direction and the same process was repeated. By comparison, when the field is removed, the images become rather featureless thus suggesting magnetic curling instead of coherent rotation.<sup>26,27</sup> The MFM images taken at a static field show a single domain state with reverse polarity. This single domain behavior is in spite of the phase separation and graded composition observed by TEM. Representative images for the medium disks and crosses where dipolar contrast is evident and opposite upon field reversal are seen in **Figure 4.4**.

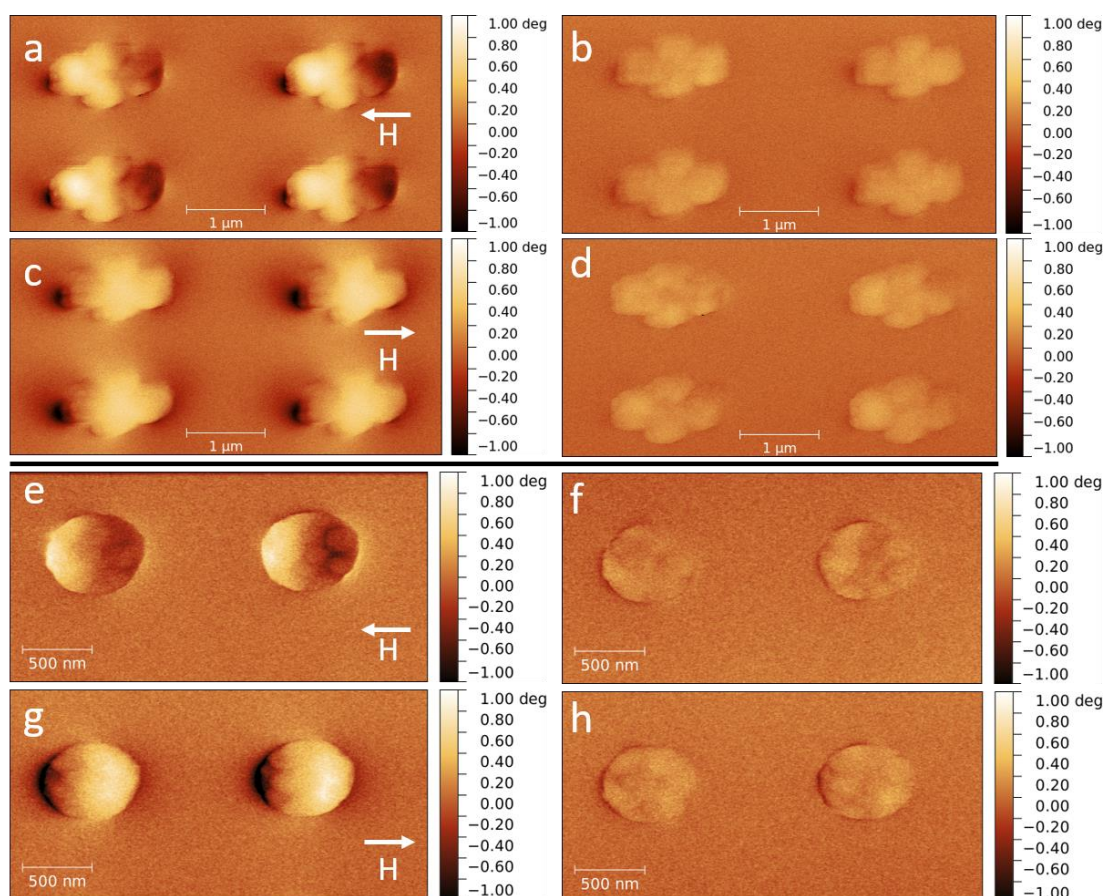


**Figure 4.4.** MFM images taken a,e) under a static field of 600 Oe, b,f) at remanence after removal of the field as well as c,g) and d,h) following the same steps upon reversal of the field direction.

Finally, since the positioning of different geometries on the same substrate did not allow acquisition of hysteresis loops of each individual array, three substrates with large single-feature arrays were also prepared. Specifically, a 6x6 and a 12x12 pattern were created by repetition of the small- and large-sized disk array, respectively, as well as a 16x16 duplication of the medium cross array. In this way, two geometries as well as three different feature sizes could be assessed. The number of duplications for each pattern was selected so as to ensure an adequate signal by VSM. The hysteresis loops corresponding to the single feature arrays, from which the diamagnetic background originating from the substrate has been subtracted, are shown in **Figure 4.5**. From this, it can be seen that saturation is reached at an applied field of more than 1000 Oe. At 600 Oe, which was the maximum achievable field by MFM, the structures cannot reach saturation. This holds especially true for the large-sized features. Meanwhile, the measured coercivities were approximately 81 Oe, 114 Oe and 174 Oe for the large disks, small disks and medium crosses, respectively.

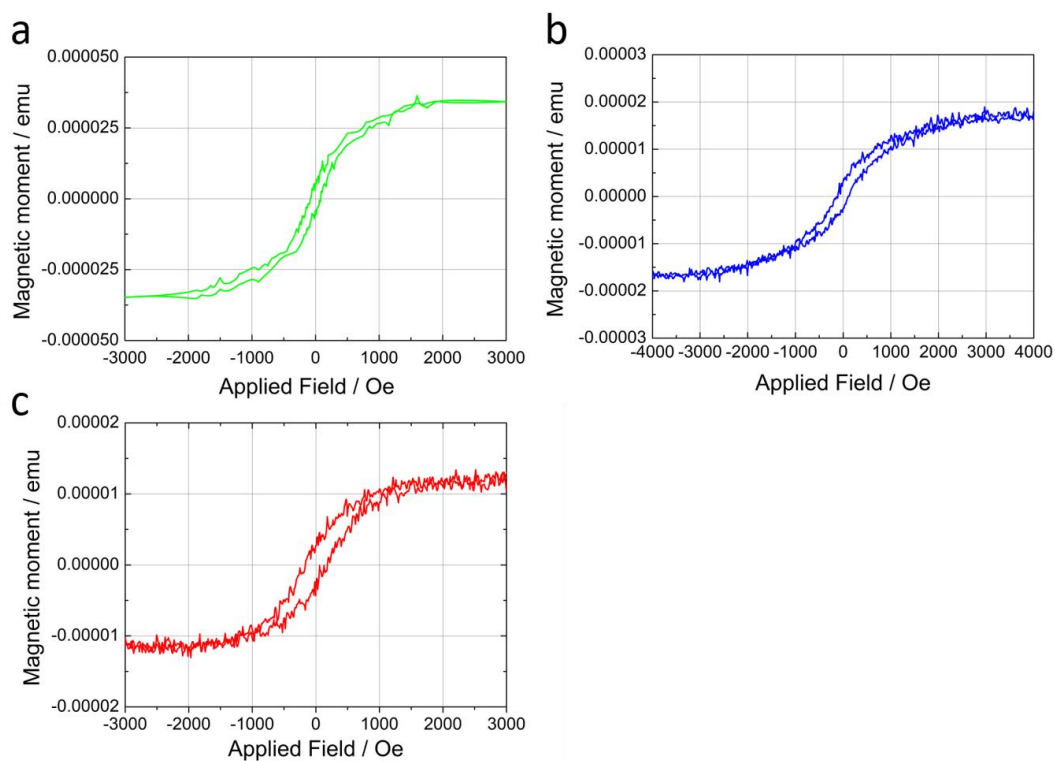


**Figure 4.5.** Hysteresis loops obtained by VSM for the large single-feature arrays of the a) large disks, b) small disks and c) medium-sized crosses.

#### 4.3.4. Chemical and morphological analysis of electroplated nano/microrods and tubes

Following preparation and investigation of the submicron motifs grown by electrodeposition into lithographed patterns of different geometries, attempts were made to fabricate dense arrays of nano- and micron-scale rods and tubes by electrodeposition into PC membranes either free-standing or attached to a self-sustaining Cu layer. In a first step, an array of standing nanorods 200 nm (Figure 4.6a) and 400 nm in diameter was produced from a Triton X-100 containing electrolyte with the aim to induce nanoporosity.<sup>28,29</sup> The electrolyte was initially tested by depositing Fe—Cu films potentiostatically at -1.1 V and -1.2 for 120 s onto Au coated Si/SiO<sub>2</sub> substrates from Solution C. The resulting nanoporous morphology of a Fe<sub>79</sub>Cu<sub>21</sub> film deposited at -1.1 V can be seen in Figure 4.6b. The established plating conditions were applied towards the growth of nanorods with reduction of the applied potential to -1

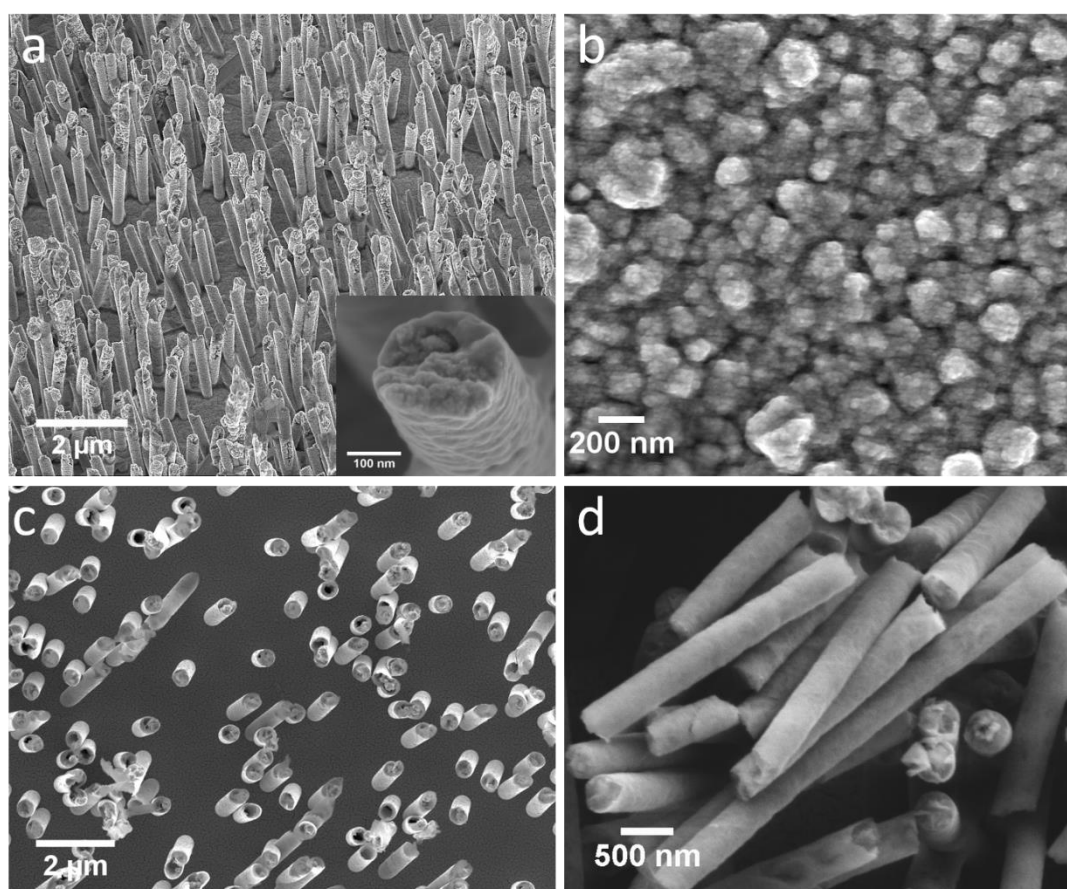


**Figure 4.6.** SEM micrographs of a) standing Fe<sub>69</sub>Cu<sub>31</sub> rods in tilted view with a magnified inset nanorod image and b) Fe<sub>79</sub>Cu<sub>21</sub> film produced from the Triton X-100 containing electrolyte as well as a c) top view of standing 400 nm Fe<sub>57</sub>Cu<sub>43</sub> rods and a d) magnified image of the Fe<sub>57</sub>Cu<sub>43</sub> rods at a site containing several detached from the substrate.

V to slightly enhance Cu content. Indeed, the overall composition of the rods as detected by EDX/SEM was  $\text{Fe}_{69}\text{Cu}_{31}$  and they are also revealed to be smooth and nanograined though the occurrence of nanoporosity was not as evident as for the continuous films.

When plating was performed without the use of nonionic surfactants, i.e. from Solution B, smooth rods with sporadic tubes were typically grown (Figures 4.6c and d). In this case, the rods were plated at -1.2 V resulting in a  $\text{Fe}_{57}\text{Cu}_{43}$  composition. Interestingly, despite the more negative overpotential, the Fe content was lower than in the Triton X-100 containing bath. This is also contrary to the fact that plating at lower temperature in this bath (i.e. at 35 °C as compared to 45 °C) tends to enhance Fe content.<sup>25</sup> This, in turn, suggests that the effect of Triton X-100 surfactant dominates over the change in the applied potential and temperature.

The diameter of the standing rods was kept small in consideration of potential applications in spintronics. An in-plane hysteresis loop recorded for the  $\text{Fe}_{69}\text{Cu}_{31}$  standing rods with a coercive field of about 223 Oe is shown in **Figure 4.7**.

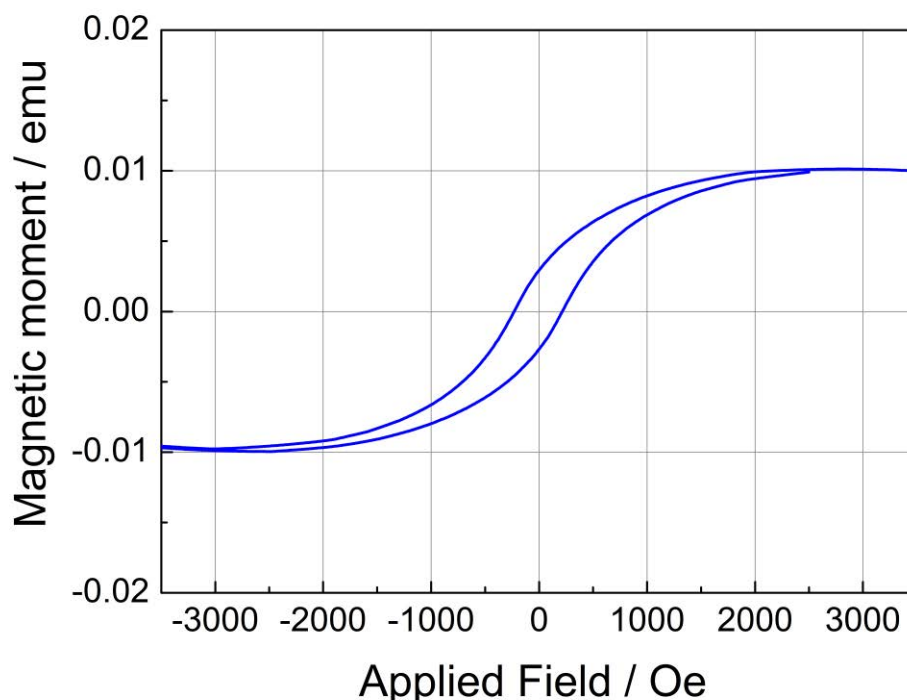


**Figure 4.7.** Hysteresis loop of  $\text{Fe}_{69}\text{Cu}_{31}$  standing rods produced by nonionic surfactant-assisted deposition.

Next, detached micron-scale tubes of 1  $\mu\text{m}$  and 2  $\mu\text{m}$  were also produced. An example of various microtubes of 2  $\mu\text{m}$  diameter is shown in **Figure 4.8**. The formation of tubes instead of rods can be attributed to the large diameter where the sputtered Au layer on the back of the membrane is non-uniform and enters the pores during sputtering attaching to their interior.<sup>30</sup> Electrodeposition will then begin at those sites rendering tubes instead of rods. It can be seen in Figure 4.8b that slightly overplating the tubes results in a mushroom-like cap formation. As verified by EDX/SEM line scans and maps, a graded composition existed along the tube axis with a consistently high Cu content at the end of the tubes. It is conjectured that this occurred due to closer proximity to the surface of the membrane during deposition.

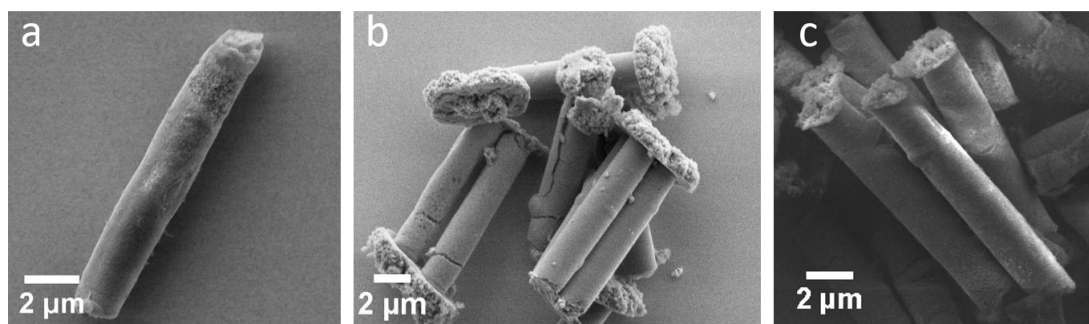


**Figure 4.8.** SEM images of electrodeposited Fe–Cu tubes of 2  $\mu\text{m}$  diameter.

Although the compositional gradient was inherent to the process, intentional modulation of the applied potential during deposition led to segments with even greater compositional difference. This is shown in **Figure 4.9**, where a potential of -1.2 V was applied for 60 s followed by 180 s at -1 V, thus constructing an Fe-rich and a shorter Cu-rich segment. Plating time can be configured to target different segment lengths. While the overall composition of the tubes was  $\text{Fe}_{73}\text{Cu}_{27}$ , a  $\text{Fe}_{21}\text{Cu}_{79}$  composition was measured close to the surface while a  $\text{Fe}_{88}\text{Cu}_{12}$  and a  $\text{Fe}_{80}\text{Cu}_{20}$  spot in the middle and at the bottom end of the tube, respectively, were also detected by line scans.

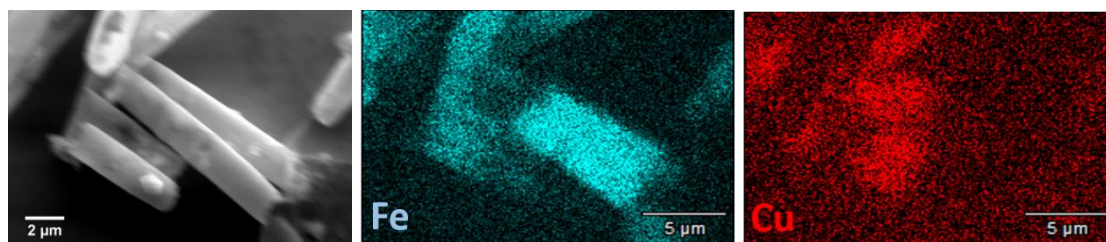


**Figure 4.9.** EDX elemental maps revealing Fe and Cu distribution along 2  $\mu\text{m}$  diameter microtubes.

### 4.3.5. Photocatalytic performance of microtubes

Efficient removal of toxic chemicals from water is one of the most pressing environmental issues of our times. In this direction, the development of photocatalytic motors for water remediation is highly promising.<sup>31,32</sup> Therefore, preliminary assessment of the photocatalytic properties of the microtubes in H<sub>2</sub>O<sub>2</sub> solutions was performed for the Fe-rich compositionally graded tubes of 2 μm diameter deposited at -1.2 V for 150 s. It is well known that Fe is prone to surface oxidation and visible-light controlled catalytic iron oxide/gold and Cu<sub>2</sub>O/Au motors have been reported<sup>33,34</sup> while the Fe-rich composition was aimed at enabling eventual magnetically-driven motion control. The hollow core of the microtubes and the large length of approximately 11 μm provided for a high surface area and was targeted at bubble-propelled motion.<sup>32</sup>

Illumination under different wavelengths of light showed that the microtubes were indeed photocatalytically active when irradiated by blue light and exhibited directional bubble-propelled locomotion in H<sub>2</sub>O<sub>2</sub> aqueous solutions. When the light source was removed, the microtubes would stop moving, thus enabling on/off switching. The trajectory traced under blue light can be observed in the still images of **Figure 4.10** which were taken from a video recording.

Nevertheless, the amount of H<sub>2</sub>O<sub>2</sub> required to trigger propulsion was about 12.5 wt % which is too high for environmental applications. Finally, repeatability was also suboptimal and time dependent.

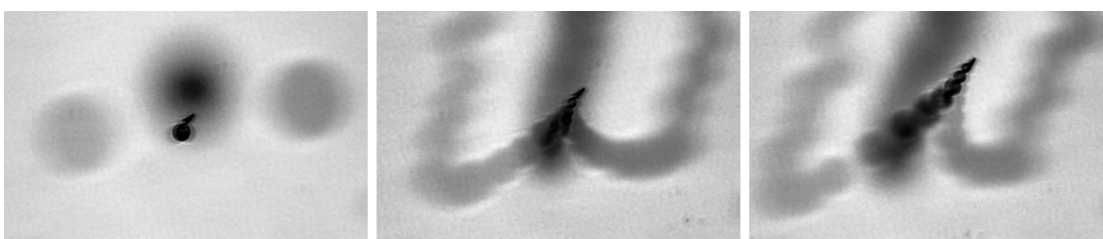


**Figure 4.10.** Still images taken at 2.5 s intervals

## 4.4. Conclusions

In this work, electrodeposition of complex Fe–Cu geometric structures onto pre-lithographed substrates as well as high aspect ratio tube and rod arrays in PC membranes was demonstrated. The fabricated features show phase separation and

graded composition which can be modulated by the applied deposition overpotential. Moreover, their straightforward preparation technique and ferromagnetic character makes them attractive candidates for a slew of potential applications in spintronics, microelectromechanical systems and in drug delivery applications in the case of the rods/tubes. Further combination with other patterning techniques such as colloidal templating would increase geometric complexity targeting novel magnetic behavior. Finally, the 2  $\mu\text{m}$  microtubes show photocatalytically-driven bubble-propulsion though the process requires additional optimization.

## References

- [1] Grünberg, P.A., 2008. Nobel Lecture: From spin waves to giant magnetoresistance and beyond. *Reviews of Modern Physics*, 80(4), p.1531.
- [2] Stamps, R.L., Breitzkreutz, S., Åkerman, J., Chumak, A.V., Otani, Y., Bauer, G.E., Thiele, J.U., Bowen, M., Majetich, S.A., Kläui, M. and Prejbeanu, I.L., 2014. The 2014 magnetism roadmap. *Journal of Physics D: Applied Physics*, 47(33), p.333001.
- [3] Hoffmann, A. and Bader, S.D., 2015. Opportunities at the Frontiers of Spintronics. *Physical Review Applied*, 4(4), p.047001.
- [4] Makarov, D., Melzer, M., Karnaushenko, D. and Schmidt, O.G., 2016. Shapeable magnetoelectronics. *Applied Physics Reviews*, 3(1), p.011101.
- [5] Lara, A., Moreno, J. R., Guslienko, K. Y. and Aliev, F. G., 2017. Information processing in patterned magnetic nanostructures with edge spin waves. *Scientific Reports*, 7(1), p.5597.
- [6] Braun, H.B., 2012. Topological effects in nanomagnetism: from superparamagnetism to chiral quantum solitons. *Advances in Physics*, 61(1), pp.1-116.
- [7] Fernández-Pacheco, A., Streubel, R., Fruchart, O., Hertel, R., Fischer, P. and Cowburn, R.P., 2017. Three-dimensional nanomagnetism. *Nature Communications*, 8, p.15756.
- [8] Pfau, B., Günther, C.M., Hauet, T., Eisebitt, S. and Hellwig, O., 2017. Thermally induced magnetic switching in bit-patterned media. *Journal of Applied Physics*, 122(4), p.043907.
- [9] Gilbert, D.A., Maranville, B.B., Balk, A.L., Kirby, B.J., Fischer, P., Pierce, D.T., Unguris, J., Borchers, J.A. and Liu, K., 2015. Realization of ground-state artificial skyrmion lattices at room temperature. *Nature Communications*, 6, p.8462.
- [10] Lau, J.W., McMichael, R.D., Chung, S.H., Rantschler, J.O., Parekh, V. and Litvinov, D., 2008. Microstructural origin of switching field distribution in patterned Co/Pd multilayer nanodots. *Applied Physics Letters*, 92(1), p.012506.



- [11] Ivanov, Y.P., Chuvilin, A., Vivas, L.G., Kosel, J., Chubykalo-Fesenko, O. and Vázquez, M., 2016. Single crystalline cylindrical nanowires—toward dense 3D arrays of magnetic vortices. *Scientific Reports*, 6, p.23844.
- [12] Ivanov, Y.P., Chuvilin, A., Lopatin, S. and Kosel, J., 2016. Modulated magnetic nanowires for controlling domain wall motion: toward 3D magnetic memories. *ACS Nano*, 10(5), pp.5326-5332.
- [13] Arshad, M.S., Šturm, S., Zavašnik, J., Espejo, A.P., Escrig, J., Komelj, M., McGuinness, P.J., Kobe, S. and Rožman, K.Ž., 2014. Effect of magnetocrystalline anisotropy on the magnetic properties of electrodeposited Co–Pt nanowires. *Journal of Nanoparticle Research*, 16(11), p.2688.
- [14] Pan, A., Zhou, W., Leong, E.S., Liu, R., Chin, A.H., Zou, B. and Ning, C.Z., 2009. Continuous alloy-composition spatial grading and superbroad wavelength-tunable nanowire lasers on a single chip. *Nano Letters*, 9(2), pp.784-788.
- [15] Pan, A., Liu, R., Sun, M. and Ning, C.Z., 2010. Spatial composition grading of quaternary ZnCdSSe alloy nanowires with tunable light emission between 350 and 710 nm on a single substrate. *ACS Nano*, 4(2), pp.671-680.
- [16] Zhang, J., Pané, S., Sort, J. and Pellicer, E., 2016. Toward robust segmented nanowires: understanding the impact of crystallographic texture on the quality of segment interfaces in magnetic metallic nanowires. *Advanced Materials Interfaces*, 3(18), p.1600336.
- [17] Thurn-Albrecht, T., Schotter, J., Kästle, G.A., Emley, N., Shibauchi, T., Krusin-Elbaum, L., Guarini, K., Black, C.T., Tuominen, M.T. and Russell, T.P., 2000. Ultrahigh-density nanowire arrays grown in self-assembled diblock copolymer templates. *Science*, 290(5499), pp.2126-2129.
- [18] Pané, S., Panagiotopoulou, V., Fusco, S., Pellicer, E., Sort, J., Mochnacki, D., Sivaraman, K.M., Kratochvil, B.E., Baró, M.D. and Nelson, B.J., 2011. The effect of saccharine on the localized electrochemical deposition of Cu-rich Cu–Ni microcolumns. *Electrochemistry Communications*, 13(9), pp.973-976.

- [19] Xie, Q., Hong, M. H., Tan, H. L., Chen, G. X., Shi, L. P. and Chong, T. C., 2008. Fabrication of nanostructures with laser interference lithography. *Journal of Alloys and Compounds*, 449(1-2), pp.261-264.
- [20] Varea, A., Pané, S., Gerstl, S., Zeeshan, M. A., Özkale, B., Nelson, B. J., Suriñach, S., Baró M. D., Nogués, J., Sort, J. and Pellicer, E., 2013. Ordered arrays of ferromagnetic, compositionally graded  $\text{Cu}_{1-x}\text{Ni}_x$  alloy nanopillars prepared by template-assisted electrodeposition. *Journal of Materials Chemistry C*, 1(43), pp.7215-7221.
- [21] Neykova, N., Hruska, K., Holovsky, J., Remes, Z. and Vanecek, M., 2013. Arrays of ZnO nanocolumns for 3-dimensional very thin amorphous and microcrystalline silicon solar cells. *Thin Solid Films*, 543, pp.110-113.
- [22] Quintana, A., Varea, A., Guerrero, M., Suriñach, S., Baró, M. D., Sort, J. and Pellicer, E., 2015. Structurally and mechanically tunable molybdenum oxide films and patterned submicrometer structures by electrodeposition. *Electrochimica Acta*, 173, pp.705-714.
- [23] Gómez, E., Pellicer, E. and Vallés, E., 2004. Microstructures of soft-magnetic cobalt–molybdenum alloy obtained by electrodeposition on seed layer/silicon substrates. *Electrochemistry Communications*, 6(8), pp.853-859.
- [24] Luo, J.K., Chu, D., Flewitt, A.J., Spearing, S.M., Fleck, N.A. and Milne, W.I., 2005. Uniformity control of Ni thin-film microstructures deposited by through-mask plating. *Journal of the Electrochemical Society*, 152(1), pp.C36-C41.
- [25] Dislaki, E., Sort, J. and Pellicer, E., 2017. Parametric aqueous electrodeposition study and characterization of Fe–Cu films. *Electrochimica Acta*, 231, pp.739-748.
- [26] Ross, C. A., Hwang, M., Shima, M., Cheng, J. Y., Farhoud, M., Savas, T. A., Smith, H. I., Schwarzacher, W., Ross, F. M., Redjda, M. and Humphrey, F. B., 2002. Micromagnetic behavior of electrodeposited cylinder arrays. *Physical Review B*, 65(14), p.144417.

- [27] Pribiag, V. S., Krivorotov, I. N., Fuchs, G. D., Braganca, P. M., Ozatay, O., Sankey, J. C., Ralph, D. C. and Buhrman, R. A., 2007. Magnetic vortex oscillator driven by dc spin-polarized current. *Nature Physics*, 3(7), p.498.
- [28] Park, S., Boo, H., Lee, S.Y., Kim, H.M., Kim, K.B., Kim, H.C. and Chung, T.D., 2008. Apparent electrocatalysis on 3D nanoporous platinum film electroplated from hexagonal lyotropic liquid crystalline phase of Triton X-100. *Electrochimica Acta*, 53(21), pp. 6143-6148.
- [29] Guerrero, M., Pané, S., Nelson, B.J., Baró, M.D., Roldán, M., Sort, J. and Pellicer, E., 2013. 3D hierarchically porous Cu–BiOCl nanocomposite films: one-step electrochemical synthesis, structural characterization and nanomechanical and photoluminescent properties. *Nanoscale*, 5(24), pp.12542-12550.
- [30] Fu, J., Cherevko, S. and Chung, C.H., 2008. Electroplating of metal nanotubes and nanowires in a high aspect-ratio nanotemplate. *Electrochemistry Communications*, 10(4), pp.514-518.
- [31] Mushtaq, F., Chen, X., Hoop, M., Torlakcik, H., Pellicer, E., Sort, J., Gattinoni, C., Nelson, B.J. and Pane, S., 2018. Piezoelectrically Enhanced Photocatalysis with BiFeO<sub>3</sub> Nanostructures for Efficient Water Remediation. *iScience*, 4, pp.236-246.
- [32] Wang, S., Jiang, Z., Ouyang, S., Dai, Z. and Wang, T., 2017. Internally/externally bubble-propelled photocatalytic tubular nanomotors for efficient water cleaning. *ACS Applied Materials & Interfaces*, 9(28), pp.23974-23982.
- [33] Zhou, D., Ren, L., Li, Y.C., Xu, P., Gao, Y., Zhang, G., Wang, W., Mallouk, T.E. and Li, L., 2017. Visible light-driven, magnetically steerable gold/iron oxide nanomotors. *Chemical Communications*, 53(83), pp.11465-11468.
- [34] Zhou, D., Li, Y.C., Xu, P., McCool, N.S., Li, L., Wang, W. and Mallouk, T.E., 2016. Visible-light controlled catalytic Cu<sub>2</sub>O–Au micromotors. *Nanoscale*, 9(1), pp.75-78.

## Discussion

The extensive consumption of critical raw materials and the devastating environmental implications of the widespread use of toxic compounds in high-tech industry has brought the urgent need for sustainable, environmentally-friendly alternatives to the forefront. Furthermore, the natural reserves of many precious noble metals and rare-earth elements is controlled by countries such as the US and China which employ protectionist policies limiting access and driving up prices. From this perspective, the Fe–Cu system presented an excellent option due to the wide availability and eco-friendliness of its constituent elements and the highly tunable magnetic properties involved. In previous literature, different methods were employed towards the preparation of mainly metallic Fe–Cu thin films and the general consensus is that the properties derived depend heavily on the fabrication method and experimental conditions. Of these, the incredible versatility, low cost, rapid growth rate, simplicity and ease of operation of the electrodeposition technique is unparalleled. Past efforts on electrodeposited Fe–Cu have been largely focused on the deposition of thin films, while the low solubility of Fe and Cu and the tendency of oxide/hydroxide formation during deposition has led to a paucity of literature on this approach.

In this thesis, thick  $\text{Fe}_x\text{Cu}_{1-x}$  films within a wide composition range ( $0 \leq x \leq 86$ ) were electrodeposited galvanostatically from three aqueous sulfate-based electrolytic solutions where the effects of different chelating agents (citric acid, glycine and sodium gluconate) and plating regimes were examined. Glycine as a complexing agent

enhanced copper inclusion while sodium gluconate had a copper suppressing effect and thus promoted the growth of Fe-rich deposits. Temperature was an important factor influencing bath efficiency, roughness and oxygen incorporation and allowing operation at higher current densities. The role of pH was also a substantial one in ensuring good deposit quality and strong adhesion to the substrate. Interestingly, the glycine and citric acid containing electrolytes showed improved performance at a low pH value while for gluconate optimal results were obtained at a higher pH. The thickness targeted was that of several micrometers and the combination of different plating parameters was connected to a substantial variation of the current efficiency. Imaging revealed a cluster-like morphology and the films were nanocrystalline and phase separated with partial alloying according to structural analysis. In the case of Fe-rich films with an iron content of 25 at% or higher obtained from the gluconate electrolyte, a thickness dependent phase separation was confirmed since films with a submicron thickness were confirmed to form a solid solution. With respect to the magnetic properties, the films were soft magnetic, and the saturation magnetization increased with Fe content. Even at very copper rich compositions the films gave a weak ferromagnetic response owing to phase separation.

The fabrication of hierarchically porous Fe–Cu thin films by coupling electrodeposition with the colloidal templating technique was also targeted. Promoting hierarchical roughness by combining nano- and micron-sized surface features has been shown both by nature and by bio-inspired synthesis approaches to lead to enhanced wetting behavior with a plethora of existing and future applications which take advantage of the properties of superhydrophobic/oleophilic and superhydrophilic/oleophobic materials. Different submicron diameters of polystyrene spheres as a hard template were chosen to investigate the influence of pore size and distribution. Two stoichiometries, Fe-rich and Cu-rich, were selected to study the effect of elemental composition. The resulting films had closely packed interconnected pores with narrow pores walls of variable roughness. Scanning electron microscopy images and subsequent ellipsometry measurements revealed the inherent nanoporosity of the material along the patterned macro-pore walls thereby confirming the hierarchical porosity present. Water and oil contact angles showed that all of the porous films

were very hydrophobic with water contact angles of up to 154° and low contact angle hysteresis also achieved. Contrarily, the oil contact angles were very low with initial values of as low as 13° and gradually decreasing. The high surface-to-volume-ratio and the superhydrophobic/oleophilic properties which engender enhanced absorption capacity and strong water repellence/-oil attraction, respectively. Therefore, the possibility of water/oil separation was investigated as a proof of concept. Results indicated that the films possessed good absorption capacity (up to 60%) which was maintained at a satisfactory level after multiple absorption/rinsing cycles. We postulate that the absorption capacity measured was underrepresented since the oil droplets had a tendency to stick to the glass beaker container and more specifically around the water surface/glass beaker contact line. Furthermore, the submicron pore size implies that these films are also suitable for water/oil separation in emulsified solutions.

Moore's law, formulated by Intel cofounder Gordon Moore in 1965, stipulated that the number of transistors per square inch of circuit would double every year. The pace was adjusted to a doubling every two years in 1975. This had been the golden rule for the semiconductor industry for more than 50 years but has begun to falter with the ever-increasing number of circuitries crammed in a single chip and the inevitable heat generated. Spin-based electronics offer a possible solution to the current conundrum. On this premise, further exploiting the hierarchically porous nature of the Fe–Cu films in tandem with their ultrathin pore walls and ferromagnetic character, magneto-electric measurements using ionic liquid gating were conducted. These revealed that the narrowness of the pore walls and intrinsic nanoporosity could bypass the ultrathin film requirement and enable magneto-electric effects despite the overall film thickness of hundreds of nanometers. Specifically, a coercivity reduction of up to 25% was observed. Elemental and structural analysis led to the conclusion that the effects were mainly ascribed to charge accumulation/dissipation. The implications of voltage-induced coercivity modulation for energy-efficient devices, owing to the reduction of Joule effect related heat dissipation, with applications in areas such as cloud computing, mobile devices, and robotics, cannot be overstated.

Finally, pursuing the current trend towards miniaturization in technologies such as data storage and processing, biomechanics and MEMS/NEMS, magnetic nano- and micron-scale structures, rods and tubes were fabricated. For the creation of structures with different geometric shapes (disks, crosses, stripes) and sizes in nine configurations, a combinatorial approach of electrodeposition with electron beam lithography, a powerful technique offering ultra-high resolution, was undertaken. A higher aspect ratio was attained than commonly reported for lithographed motifs which holds great promise due to the transition to three-dimensional nanomagnetism where novel phenomena can occur. A gradient of composition was observed with an increase of copper amount at the surface. Magnetic studies were not straightforward in the case of the structures, hindered by the inclusion of all patterns on one substrate and the exceptionally copper rich surface which excluded MOKE analysis. Nevertheless, the fabrication of large single feature arrays on a substrate enabled VSM measurements of two chosen geometries which showed a weak soft ferromagnetic signal. Magnetic force microscopy was more promising for studying magnetization reversal though the maximum applied field magnitude was limited to 600 Oe which did not achieve saturation. Magnetic curling effects were also observed. On the other hand, for the preparation of the arrays of rods and tubes, polycarbonate PC membranes were used as hard templates. Apart from the intrinsic to the process compositional gradient, the creation of Fe-rich and Cu-rich segments was accomplished. The free-standing tubes and rods responded strongly to an external magnet while the microtubes showed photocatalytic bubble-propelled directional locomotion. These nano/micromotors can function as mobile platform in diverse chemical applications.

As can be discerned from the above, electrodeposition and sustainability were the predominant driving forces and main focal points of this thesis while multifaceted functionalization with respect to geometry and compositional control was intensely endeavored. Environmental applications such as the removal of toxic chemicals from water as well as the effective and sustainable cleanup of oil spills were targeted by the photocatalytic microtubes and the patterned superhydrophobic/oleophilic films, respectively. Correspondingly, the voltage-controlled coercivity modulation achieved

in the patterned films can lead to enhanced energy efficiency in spintronics applications. The Fe—Cu system, with its low-cost and abundant constituent elements along with its intriguing magnetic properties, was at the center of all these ventures.





## Conclusions

The main conclusions that can be drawn are summarized in the bullet points below:

1. Fe–Cu continuous coatings with low oxygen content can be prepared over a wide composition range from a single electrolyte by tuning plating parameters such as temperature, pH and applied current densities.
2. The choice of complexing agent is vital in determining the compositions that can be achieved, the range of operating current densities and oxygen incorporation in the deposits.
3. The role of temperature on the morphology of the deposits is significant and roughness decreases substantially at higher temperatures.
4. The Fe–Cu deposits exhibit a cauliflower-like morphology with more closely packed clusters at high iron content. Meanwhile, almost pure Cu deposits are smooth with a nodular morphology.
5. Oxygen was mainly located at the uppermost surface forming a passivation layer.
6. The Fe–Cu thick continuous coatings are nanocrystalline and are characterized by phase separation with partial alloying when the thickness is that of several micrometers. Meanwhile, Fe<sub>75</sub>Cu<sub>25</sub> and Fe<sub>85</sub>Cu<sub>15</sub> thin films obtained from the gluconate containing electrolyte are shown to be fully alloyed.

7. The magnetization is easily tunable and increases with Fe content. Due to phase separation and the formation of Fe-rich clusters even films with 6 at% Fe have a weak ferromagnetic response.
8. The Fe-rich and Cu-rich deposits can be patterned by colloidal templating using PS spheres of various diameters ranging from 200 nm to 500 nm to create hierarchically porous structures with closely packed macropores of different diameters. The ultrathin pore walls are shown to be nanoporous.
9. The patterned macroporous films are also revealed to be single phase contrary to the thick continuous coatings.
10. The Fe-rich and Cu-rich patterned films are hydrophilic and oleophobic. Water contact angles of  $155^\circ$  with a contact angle hysteresis of  $6.7^\circ$  is achieved for the 500 nm  $\text{Fe}_{85}\text{Cu}_{15}$  film while initial oil contact angles in the range of  $13^\circ - 18^\circ$  are recorded. Compared to continuous films, the contact angle greatly increases with patterning.
11. As a proof of concept, the superhydrophobic  $\text{Fe}_{85}\text{Cu}_{15}$  patterned films are shown to be capable of separating oil from water.
12. The hierarchical porosity and ultrathin pore walls of the Fe-rich patterned films are shown to be an excellent way of bypassing the ultrathin film requirement for observing magneto-electric effects in metals. A voltage-driven coercivity reduction of up to 25% was reached.
13. The structural changes induced by the electric field during magneto-electric measurements mainly influence the Cu species at the surface, whereas the Fe species controlling the magnetic behavior remain unaltered.
14. High aspect ratio Fe–Cu compositionally graded submicron structures of different geometries with sharply defined features has been achieved by coupling electrodeposition with electron beam lithography. At static fields, the structures show dipolar contrast which vanishes at zero field suggesting magnetic curling.

15. Free-standing or detached Fe–Cu nano- and microrods and tubes deposited into PC membranes show a graded composition while intentional Fe-rich and Cu-rich segment creation is possible with modification of the applied potential during deposition.
16. The Fe-rich microtubes of 2  $\mu\text{m}$  diameter show photocatalytic directional bubble propulsion under blue light.



---

## Future perspectives

In view of the results described in this thesis, several potential avenues for future research can be outlined:

1. The effect of different levelers on the quality of the obtained deposits can be further studied. Pulsed plating can also be employed to investigate the effect on morphology and composition.
2. The properties of films obtained by electrodeposition with use of a nonionic surfactant can be thoroughly characterized. Eventually, the evolution of the mechanical properties of 2:1 aspect ratio microstructures produced with and without the surfactant addition and with different levelers can be determined.
3. Further magnetic and structural investigation of the patterned submicron features by X-ray magnetic circular dichroism (XMCD), photoemission electron microscopy (PEEM) and XRD at synchrotron radiation facilities will shed light into the magnetic behavior observed.
4. The performance and repeatability of the photocatalytic microtubes can be optimized so as to make them suitable for environmental applications. Gold segments produced from a cyanide free gold containing electrolyte could aid in this direction. Magnetic steering of the microtubes can also be applied.
5. The Triton X-100 concentration and plating conditions for the nanorods produced by nonionic surfactant-assisted electrodeposition should be improved upon in order to render a fully nanoporous morphology.

6. Additional patterning of large diameters rods using polystyrene colloidal spheres to produce a hierarchically porous structure could make them interesting for a variety of applications.
7. Cytotoxicity of the Fe–Cu deposits and nano/microrods and tubes can be assessed for possible biological applications.

